

A THESIS FOR THE DEGREE OF PH.D. IN ENGINEERING

Magnetic properties of single
crystalline Mn_5Ge_3 films grown on
Ge(111) substrates

SEPTEMBER 2015

GRADUATE SCHOOL OF SCIENCE AND TECHNOLOGY

KEIO UNIVERSITY

TRUONG NHU PHUOC ALAIN

À ma famille, qui m'a toujours soutenu.

Abstract

The field of spintronics has increasingly become an interest because of the possibility to manipulate magnetic properties with electric current and to produce spin currents. Spin currents are less energy-consuming than charge currents and they can be generated in a semiconductor material by a process called spin injection, using a ferromagnet as a spin polarizer. Due to the fact ferromagnets are usually metallic, the efficiency of spin injection is affected by the difference of conductivity between the ferromagnet and the semiconductor. In order to prevent such conductivity mismatch, the creation of ferromagnetic semiconductors was proposed. Semiconductors doped with magnetic atoms (diluted magnetic semiconductors) are excellent candidates as spin polarizers due to their conductivity matching. They are however difficult to fabricate and suffer from low Curie temperatures. The use of highly spin-polarized ferromagnetic metals, that can be grown epitaxially on doped semiconductors, represents a reasonable alternate choice as long as the properties at the ferromagnet/semiconductor interface can be controlled. Mn_5Ge_3 has the advantage to be grown coherently on Ge(111) with a relatively high Curie temperature and spin polarization.

The present thesis gives a characterization of the interface between epitaxial Mn_5Ge_3 thin films and their Ge substrate. The evidenced interfacial spin-glass state is a promising result towards elucidating the interactions between ferromagnets and spin-glasses, which could open new prospects for spintronics applications.

This thesis is composed of six chapters. Chapter 1 explains the motivations of this thesis. Chapter 2 gives a general background about epitaxial growth and deals with the structural characterization of the Mn_5Ge_3 thin films used in this work. Chapter 3 introduces the magnetic properties that are relevant to this work.

Chapter 4 provides a detailed characterization of the magnetocrystalline anisotropy

in Mn_5Ge_3 by using the ferromagnetic resonance technique. It is revealed that, despite being weak, a perpendicular anisotropy exists in such Mn_5Ge_3 thin films and its temperature dependence is successfully determined not to follow the Callen-Callen law. By comparing the perpendicular anisotropy with the shape anisotropy, this chapter concludes that the weak perpendicular anisotropy does not affect the magnetization hysteresis at low temperature.

Chapter 5 explains the presence of a thermal irreversibility in the in-plane magnetization of Mn_5Ge_3 thin films. A spin-glass-like state arising at the interface between Mn_5Ge_3 and Ge considerably changes the magnetic properties of the ferromagnetic Mn_5Ge_3 by introducing a slow magnetization dynamics below the Curie temperature. It is also observed that the spin-glass-like state clearly depends on the growth conditions.

Chapter 6 concludes the results of this work.

Acknowledgements

When I came to Itoh group in September 2012, it was my very first time in Japan. From the beginning of my stay, I was simultaneously confronted to the environment of research and Japanese culture. I have seen and learnt countless things, whether they are directly or indirectly related to research. I would like to thank all the people, without whom I could not have accomplished my doctorate.

The first person I would like to acknowledge is my Ph.D. advisor Professor Kohei M. Itoh, for giving me the opportunity to join his laboratory, for his guidance and time spent on fruitful discussions about my research. Not only did he advice me about physics, but he also played a very essential role in giving me an insight of the proper behavior to adopt as a Ph.D. student. Through his teachings, I became aware of the responsibility a Ph.D. student should have towards science. He told me that a Ph.D. course could sometimes be felt as a lonely trip, during which one has to find their own path and persistence is nearly the only way to produce favorable outcomes. His positive comments as well as his criticisms gave me the strength to pursue my goals under any conditions.

Secondly, I would like to thank Dr. Takeharu Sekiguchi. I was amazed by the expertise he has in so many fields in physics. By giving me his precious time, he helped me with the theoretical and experimental aspects of crystallography, which were of considerable importance for my research.

My deepest thanks to Professor Tomoyasu Taniyama for his warm welcome to Tokyo Institute of Technology, for the helpful discussions we had, and for letting me use his equipments. I am also really thankful to Professor Tetsuya Sato and Professor Kazuya Ando for their time spent on the review of my publications and the correction of this thesis. I owe them a big part of my knowledge in magnetism. I am also grateful to Professor Eiji Ohta for his careful review of my graduation thesis.

I would like to thank Aizawa-san for her unconditional support as well as Kuroda-san for his invaluable help on the TEM analyses.

My special thanks to Dr. Pierre-André Mortemousque, a former member of Itoh group, for guiding me through the Japanese lifestyle during my first months in Japan, and for being one of my best friends. Although we did not share the same research project, discussions with him have always been of benefit to me.

I would also like to express my gratitude to Atom Watanabe for his efficiency and good performance in research, and also for his unconditional friendship and support in daily life. To my mind, he is a brilliant Bachelor student who has everything to become a competent professor in the future. I am convinced that his dreams will come true and I wish him good luck for his Ph.D. program at Georgia Tech.

It has also been a real pleasure working with Ryotaro Kiga, a new member. I wish he joined our group earlier, the atmosphere would have been even more pleasant.

A special thought for the other Bachelor students: Yuri Kusano, Kazuki Itoh, Yuhi Aikyo, Yu Miyajima and Kento Sasaki. They are all hard-working and I wish them a lot of success in their projects.

Although few of the group members were directly involved in my project, their research activities and spirits among many other things, affected me in several ways, and all the other past and present group members are worthy of acknowledgements: Atsunori Tanaka, Akitomo Naoi, Shun Hyodo, Naoyuki Shibayama, Manabu Otsuka, Kohei Ohashi, Michihiro Yamada, Takahisa Tanaka, Taiga Isoda, Eri Sato, Kaito Yamada, Keisuke Takai, Chuting Wang, Isabell Gross, Samuel Rosenius, Christophe Culan, Simon Berger, Dong Ok Kim, Rémi Debette and Marc Appleton.

On the financial aspect, this work was supported in part by Grant-in-Aid for Scientific Research by MEXT, in part by NanoQuine, in part by JSPS Core-to-Core program, in part by the Cooperative Research Project of the Research Institute of Electrical Communication, Tohoku University, and in part by the Collaborative Research Project of the Materials and Structures, Tokyo Institute of Technology.

Contents

1	Introduction	1
1.1	Background and motivation	2
1.1.1	Nanomagnetism	2
1.1.2	Diluted magnetic semiconductors	4
1.1.3	The Mn-rich compound Mn_5Ge_3	6
1.2	Organization of this thesis	8
	Bibliography	9
2	Thin film growth and structural characterization	12
2.1	The molecular beam epitaxy technique	13
2.1.1	The fundamentals of epitaxial growth	13
2.1.2	The solid phase epitaxy	19
2.2	Reflection high-energy electron diffraction	21
2.3	The $\text{Mn}_5\text{Ge}_3(001)/\text{Ge}(111)$ epitaxial relation	27
2.4	The crystallography of Mn_5Ge_3	33
	Bibliography	58
3	Magnetometry and magnetic properties	60
3.1	Superconducting quantum interference device	61
3.2	Magnetic anisotropy	67
3.3	Irreversibility in the temperature dependence of the magnetization	70

3.3.1	Superparamagnetism	70
3.3.2	Spin glasses	73
	Bibliography	77
4	Angular dependence of the ferromagnetic resonance in Mn_5Ge_3	80
4.1	Introduction	81
4.2	Preliminary study of the magnetization cycles at several temperatures	82
4.3	Free energy of the system	85
4.4	Resonance condition for the angular dependent FMR in the hexagonal symmetry	90
4.5	Summary	100
	Bibliography	102
5	Interfacial spin-glass-like state in $\text{Mn}_5\text{Ge}_3/\text{Ge}(111)$	104
5.1	Introduction	105
5.2	Experimental details and structural characterization	106
5.3	Characterization of the irreversible thermal magnetization	109
5.3.1	Zero-field-cooling and field-cooling magnetization curves . . .	109
5.3.2	Analysis of the ac susceptibility in Mn_5Ge_3	113
5.3.3	Possible origin of the spin-glass-like behavior	121
5.4	Influence of the growth conditions on the spin-glass-like behavior . . .	124
5.4.1	Influence of the solid phase epitaxy temperature	124
5.4.2	Influence of the thickness	126
5.5	Summary	129
	Bibliography	130
6	Conclusion	134

Chapter 1

Introduction

It is a well-known fact that the materials science at nanoscale can reveal novel properties in electronics and magnetism. Nanomagnetism and spintronics form a discipline that combines both ferromagnetism and electronics, which holds wide prospects for technological applications and understanding new physics.

The first part of this chapter will explain the motivations of this work (section 1.1), then it will describe the organization of this thesis (section 1.2).

1.1 Background and motivation

The effect of size confinement due to small dimensionality has an important influence on the properties of materials. The nanostructure can be divided in three structures: thin films (2D), nanowire (1D), and nanodots (0D). This thesis focuses on the properties of Mn_5Ge_3 in the form of thin films.

1.1.1 Nanomagnetism

The ferromagnetic ordering is a complex phenomenon that involves several competing energies, each of which act on different length scales. Ferromagnetism mainly arises from the exchange interaction between magnetic moments, whose origin is the fact that the wave function of electrons must be antisymmetric. That is to say, for two electrons of space and spin coordinates \mathbf{r}_1, s_1 and \mathbf{r}_2, s_2 , the wave function must follow this relation $\Psi(\mathbf{r}_1, s_1, \mathbf{r}_2, s_2) = -\Psi(\mathbf{r}_2, s_2, \mathbf{r}_1, s_1)$. Due to the Pauli principle, the wave function becomes zero when the two electrons are identical. The exchange interaction is responsible for the ordering of the spins, and its range is limited to neighboring spins \mathbf{S}_1 and \mathbf{S}_2 : $E_{\text{ex}} = -2J\mathbf{S}_1 \cdot \mathbf{S}_2$, with J being the exchange coupling constant. Contrary to the exchange interaction, the dipolar interaction is a long range interaction. Together with the spin-orbit interaction, this magnetic dipolar interaction is responsible for the magnetocrystalline anisotropy, as will be discussed later, and competes with the exchange interaction to form magnetic domains. The exchange interaction favors wider domains while the magnetocrystalline anisotropy acts towards reducing their size.

The size confinement plays a role in two-dimensional structures. For metals, ferromagnetism appears when the Stoner criterion [1] is verified: $ID(E_F) > 1$, where I

is the exchange integral and $D(E_F)$ is the density of state at the Fermi level. The electronic structure at the surface of a material differs from that of the bulk because the different coordination number of surface atoms and the presence of incomplete bonds can alter the density of states. For example, palladium (Pd) is normally a paramagnetic material in its bulk state, however, very thin layers of Pd have been proved to show ferromagnetic ordering [2]. Many other non-magnetic bulk systems have been shown to become ferromagnets at low dimensions [3, 4, 5, 6, 7]. The low dimensionality also affects the magnetization reversal process, the properties of the magnetic domains and the way the domain walls nucleate. Thin films will indeed tend to form Néel wall rather than Bloch walls [8]. New kinds of magnetic anisotropy can also arise from surface effects [9, 10].

The competition between the exchange interaction and the magnetic anisotropy leads to the existence of a critical size below which ferromagnetic nanoparticles have uniform magnetization and are made of a single domain. Materials including such nanoparticles tend to lose their ferromagnetic properties and become to superparamagnets, due to fluctuation of magnetic moments caused by the thermal energy. The presence of an activation energy is a sign of slow magnetization dynamics at low temperature.

Another kind of magnetic materials with slow magnetization dynamics is the spin glasses. Spin-glasses arise from random and frustrated exchange interactions among the magnetic moments. An important fact is the possibility of formation of spin-glass phases at surfaces or interfaces of magnetically ordered phases [11, 12, 13, 14]. Such interfacial spin-glass phase can drastically change the magnetic properties by causing disorder and frustration in the ordered phase. The formation of surface spin glasses has been shown to occur mainly around ferromagnetic particles so far. A section

of the present work experimentally demonstrates that ferromagnetically ordered epitaxial layers of Mn_5Ge_3 on $\text{Ge}(111)$ have a slow magnetization dynamics below the Curie point, due to the presence of a naturally formed spin-glass-like layer at the $\text{Mn}_5\text{Ge}_3/\text{Ge}$ interface. Thus, the properties of the material as a thin film are very much different from the bulk material because of the disorder present at the interface with the substrate.

1.1.2 Diluted magnetic semiconductors

The aim of spintronics is to exploit both charge and spin degrees of freedom of the electrons, in order to develop faster and less power-consuming nonvolatile memory devices. The potential of a material for spintronics applications relies on its ability to inject spins and detect spin-polarized currents in a semiconductor [15, 16].

In ferromagnetic materials the density of states at the Fermi level for majority and minority carriers is not the same, thus electrical currents in ferromagnets are spin-polarized, while it is not the case in non-ferromagnetic materials. In order to obtain spin-polarized currents in a semiconductor, spin-injection from a ferromagnet to a semiconductor is a possible method. However, due to the fact that ferromagnets are generally metals, the spin-injection efficiency is reduced by the conductivity mismatch at the interface between the ferromagnet and the semiconductor. A possible solution to the conductivity mismatch is to fabricate ferromagnetic semiconductors, which would have both ferromagnetic ordering and lower conductivities than metals. The growth of such materials began with the experimental and theoretical studies of diluted magnetic semiconductors based on rare-earth chalcogenide and chromite spinels. Ferromagnetism was then achieved in p-type Mn-doped semiconductors from groups IV-VI (Ref. [17]), III-V (Refs. [18, 19, 20]), and II-VI (Refs. [21, 22]). $\text{In}_{1-x}\text{Mn}_x\text{As}$

[23] and $\text{Ga}_{1-x}\text{Mn}_x\text{As}$ [19, 24, 25] are notable group III-V diluted magnetic semiconductors, which Curie points ranged from 35 to 110 K. Despite their relatively low Curie temperatures, new properties were found from the interplay between ferromagnetism and semiconducting properties, such as the colossal magnetoresistance [26]. However, the experimental study of diluted magnetic semiconductors is hard to carry out further, due to the difficulties related to the fabrication of those materials, despite the use of low-temperature molecular beam epitaxy.

Diluted magnetic semiconductors based on Si or Ge would be of interest due to their possible integration in Si or Ge-based electronics and complementary metal-oxide semiconductor device [27, 28]. The well-known work from Park *et al.* (see Ref. [29]) reported the epitaxial growth of p-type $\text{Ge}_{1-x}\text{Mn}_x$ diluted magnetic semiconductors, in which the ferromagnetic order was mediated by holes. Calculations using density functional theory indicate that the interaction between Mn atoms is antiferromagnetic at short range and ferromagnetic at long range, and that the long range ferromagnetic interactions were dominant, which explains the overall ferromagnetic order. This report from Park *et al.* also established that the Curie temperature increases linearly with the Mn concentration in the Ge host semiconductor, however the material suffered from low Curie temperature (20 to 120 K for $0.6\% < x < 3\%$), similar to group III-V ferromagnetic semiconductors. Nevertheless, this linear relationship is only valid for low Mn concentrations, because Mn has a low solubility in Ge thus resulting in phase separations into Mn-rich phases and Ge-rich phases [30, 31] and yielding high inhomogeneity. Some stoichiometries of such formed Mn-rich clusters have ferromagnetic orders, and therefore they produce extrinsic ferromagnetism, which is not mediated by charge carriers as it should be in diluted magnetic semiconductors.

1.1.3 The Mn-rich compound Mn_5Ge_3

Due to the difficulties of fabricating homogeneous diluted magnetic semiconductors with high Curie temperatures, efforts have been concentrated on improving the spin injection efficiency from ferromagnetic metals to semiconductors. The main challenge is to keep the polarization of the spin while they are injected through the ferromagnet/semiconductor interface. In order to reduce the impedance mismatch, doped semiconductors can be used [32]. The nature of the interface is also important.

For the fabrication of a ferromagnet/semiconductor heterostructure, the metallic compound Mn_5Ge_3 has recently become attractive for the spin injection in the group IV semiconductor Ge. This Mn-Ge alloy has a hexagonal structure and it was proved theoretically and experimentally to grow epitaxially on Ge(111) substrates [33, 34, 35, 36, 37, 38], with a lattice mismatch less than 3% [39, 40]. An illustration of the lattice of $\text{Mn}_5\text{Ge}_3(001)$ on Ge(111) is given in Fig. 1-1. In the form of a thin film, its Curie temperature is about 296 K, which is close to room temperature. Moreover, recent studies demonstrated that the Curie point can be increased by carbon doping up to 430 K [41], thus rendering the compound more attractive for practical applications. The spin polarization in Mn_5Ge_3 was evaluated to be about 54% [42]. The spin polarization is usually much lower than 100% because of the possible intermixing between the metallic ferromagnet and the semiconductor, the presence of defects at the interface [43, 44, 45].

As many groups already focus on the properties of spin currents in Mn_5Ge_3 on Ge(111), performing spin injection is not the direct goal of this thesis. In fact, the characterization of the magnetic properties at the $\text{Mn}_5\text{Ge}_3/\text{Ge}$ interface is an important step towards understanding and possibly optimizing the magnetic properties of the heterostructure. Therefore the aim of this thesis is to thoroughly analyze

fundamental properties of Mn_5Ge_3 epitaxial thin films that have not been clearly explained so far, such as the magnetic anisotropy. Indeed, in-plane magnetization hysteresis cycles show relatively weak remanence ratios, which is a sign of anisotropy. However, this work will show that despite the presence of an out-of-plane magnetocrystalline anisotropy, the in-plane magnetization is actually unaffected by this out-of-plane anisotropy. This fact motivates the measurements of zero-field-cooling and field-cooling magnetizations in order to detect any possible nonhomogeneous interactions. A thermal irreversibility in the magnetization is indeed evidenced, and further analyses done in this work will show that the $\text{Mn}_5\text{Ge}_3/\text{Ge}$ interface is, in fact, made of a disordered magnetic phase, similar to a spin glass. Previous reports also stated that Mn_5Ge_3 films of high thicknesses have magnetic properties which are very far from that of the bulk. Thus, this work states the importance of the interfacial magnetic interactions in the $\text{Mn}_5\text{Ge}_3/\text{Ge}$ heterostructure.

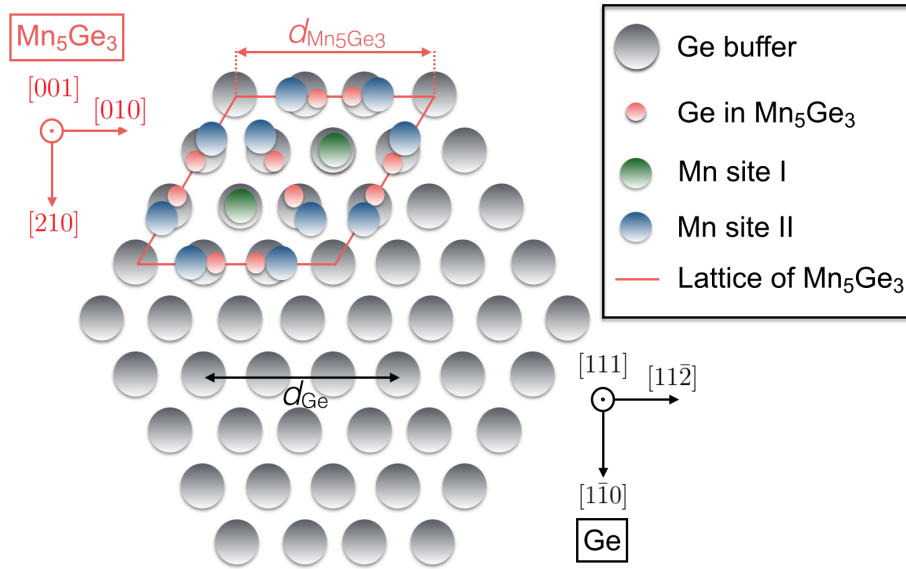


Figure 1-1: Schematic of the lattice of $\text{Mn}_5\text{Ge}_3(001)$ grown on $\text{Ge}(111)$. The distances $d_{\text{Mn}_5\text{Ge}_3}$ and d_{Ge} are the in-plane distances for Mn_5Ge_3 and Ge in the $[010]$ and $[11\bar{2}]$ directions, respectively.

1.2 Organization of this thesis

Chapter 1 provided the motivation for the research performed in this thesis. Chapter 2 gives a general background on epitaxial growth and a structural characterization of $\text{Mn}_5\text{Ge}_3(001)$ on $\text{Ge}(111)$. Chapter 3 introduces the physics related to the magnetic properties and phenomena that are relevant to this thesis.

Chapter 4 introduces the ferromagnetic resonance technique as a way to characterize the magnetocrystalline anisotropy in a ferromagnet. The study of magnetocrystalline anisotropy in Mn_5Ge_3 is motivated by the fact that the magnetic hysteresis undergoes an abrupt change between 200 and 290 K. It is shown that despite the dominance of the shape anisotropy in Mn_5Ge_3 epitaxial thin films, a perpendicular anisotropy exists due to the epitaxial relationship between $\text{Mn}_5\text{Ge}_3(001)$ and $\text{Ge}(111)$. However, this perpendicular anisotropy is too weak to contribute to the decrease in remanence ratio observed in the hysteresis curves at low temperatures.

Chapter 5 evidences the presence of a thermal irreversibility in the temperature dependence of the in-plane magnetization of the Mn_5Ge_3 thin films. Despite being a single crystal and having no apparent signs of randomness or frustration, the Mn_5Ge_3 epitaxial layers shows a slow magnetization dynamics just below the Curie point. Such property is attributed to the presence of a “ferromagnetically dead” layer at the $\text{Mn}_5\text{Ge}_3/\text{Ge}$ interface, and the slow dynamics is caused by the interaction between Mn_5Ge_3 and the interfacial layer. The analysis of the ac susceptibility measurements indicate that the irreversible behavior is similar to that of a spin glass. It is also demonstrated that the magnetic properties of the spin-glass-like layer are very sensitive to the growth conditions. Thus the properties of the ferromagnetic Mn_5Ge_3 are considerably altered by the frustrated magnetic interactions at the interface with Ge.

Chapter 6 summarizes and concludes the results obtained in this work.

Bibliography

- [1] E. C. Stoner, Proc. R. Soc. London, Ser. A **154**, 656 (1936). [Cited on page(s) 2.]
- [2] S. Sakuragi, T. Sakai, S. Urata, S. Aihara, A. Shinto, H. Kageshima, M. Sawada, H. Namatame, M. Taniguchi, and T. Sato, Phys. Rev. B **90**, 054411 (2014). [Cited on page(s) 3.]
- [3] T. Taniyama, E. Ohta, and T. Sato, Europhys. Lett. **38**, 195 (1997). [Cited on page(s) 3.]
- [4] T. Shinohara, T. Sato, and T. Taniyama, Phys. Rev. Lett. **91**, 197201 (2003). [Cited on page(s) 3.]
- [5] B. Sampedro, P. Crespo, A. Hernando, R. Litrán, J. C. Sánchez Lopez, C. López Cartes, A. Fernandez, J. Ramírez, J. González Calbet, and M. Vallet, Phys. Rev. Lett. **91**, 237203 (2003). [Cited on page(s) 3.]
- [6] Y. Yamamoto, T. Miura, Y. Nakae, T. Teranishi, M. Miyake, and H. Hori, Phys. B (Amsterdam, Neth.) **329-333**, 1183 (2003). [Cited on page(s) 3.]
- [7] Y. T. Jeon and G. H. Lee, J. Appl. Phys. **103**, 094313 (2008). [Cited on page(s) 3.]
- [8] S. Middelhoek, J. Appl. Phys. **34**, 1054 (1963). [Cited on page(s) 3.]
- [9] R. R. Birss: *Symmetry and Magnetism*, Series of Monographs on selected Topics in Solid State Physics, ed by E. P. Wohlfarth (North-Holland Publishing Co., Amsterdam, John Wiley and Sons, New York 1966). [Cited on page(s) 3, 86, and 88.]
- [10] P. Bruno and J. P. Renard, Appl. Phys. A **49**, 499 (1989). [Cited on page(s) 3 and 68.]
- [11] T. Zhu, B. G. Shen, J. R. Sun, H. W. Zhao, and W. S. Zhan, Appl. Phys. Lett. **78**, 3863 (2001). [Cited on page(s) 3, 105, and 122.]
- [12] B. Martínez, X. Obradors, Ll. Balcells, A. Rouanet, and C. Monty, Phys. Rev. Lett. **80**, 181 (1998). [Cited on page(s) 3, 105, 118, and 122.]
- [13] S. B. Xi, W. J. Lu, H. Y. Wu, P. Tong, and Y. P. Sun, J. Appl. Phys. **112**, 123903 (2012). [Cited on page(s) 3, 105, and 122.]
- [14] P. Dey, T. K. Nath, P. K. Manna, and S. M. Yusuf, J. Appl. Phys. **104**, 103907 (2008). [Cited on page(s) 3 and 122.]
- [15] S. A. Wolf, D. D. Awschalom, R. A. Buhrman, J. M. Daughton, S. von Molnár, M. L. Roukes, A. Y. Chtchelkanova, D. M. Treger, Science **294**, 1488 (2001). [Cited on page(s) 4.]

-
- [16] R. Jansen, *Nat. Mater.* **11**, 400 (2012). [Cited on page(s) 4.]
- [17] T. Story, R. R. Galazka, R. B. Frankel, and P. A. Wolff, *Phys. Rev. Lett.* **56**, 777 (1986). [Cited on page(s) 4.]
- [18] H. Ohno, H. Munetaka, T. Penney, S. von Molnár, and L. L. Chang, *Phys. Rev. Lett.* **68**, 2664 (1992). [Cited on page(s) 4.]
- [19] H. Ohno, A. Shen, F. Matsukura, A. Oiwa, A. Endo, S. Katsumoto and Y. Iye, *Appl. Phys. Lett.* **69**, 363 (1996). [Cited on page(s) 4 and 5.]
- [20] A. van Esch *et al.*, *Phys. Rev. B* **56**, 13103 (1997). [Cited on page(s) 4.]
- [21] A. Haury, A. Wasiela, A. Arnoult, J. Cibert, S. Tatarenko, T. Dietl, and Y. Merle d'Aubigné, *Phys. Rev. Lett.* **79**, 511 (1997). [Cited on page(s) 4.]
- [22] D. Ferrand *et al.*, *J. Cryst. Growth* **214-215**, 387 (2000). [Cited on page(s) 4.]
- [23] H. Munetaka, H. Ohno, S. von Molnár, A. Segmüller, L. L. Chang, and L. Esaki, *Phys. Rev. Lett.* **63**, 1849 (1989). [Cited on page(s) 5.]
- [24] J. De Boeck, R. Oesterholt, A. Van Esch, H. Bender, C. Bruynseraede, C. Van Hoof, and G. Borghs, *Appl. Phys. Lett.* **68**, 2744 (1996). [Cited on page(s) 5.]
- [25] H. Ohno, *Science* **281**, 951 (1998). [Cited on page(s) 5.]
- [26] L. Brey and F. Guinea, *Phys. Rev. Lett.* **85**, 2384 (2000). [Cited on page(s) 5.]
- [27] Y. Zhou, W. Han, L. T. Chang, F. Xiu, M. Wang, M. Oehme, I. A. Fischer, J. Schulze, R. K. Kawakami, and K. L. Wang, *Phys. Rev. B* **84**, 125323 (2011). [Cited on page(s) 5.]
- [28] C. Sürgers, G. Fischer, P. Winkel, H. v. Löhneysen, *Phys. Rev. B* **90**, 104421 (2014). [Cited on page(s) 5.]
- [29] Y. D. Park, A. T. Hanbicki, S. C. Erwin, C. S. Hellberg, J. M. Sullivan, J. E. Mattson, T. F. Ambrose, A. Wilson, G. Spanos and B. T. Jonker, *Science* **295**, 651 (2002). [Cited on page(s) 5.]
- [30] R. Gunnella, L. Morresi, N. Pinto, A. Di Cicco, L. Ottaviano, M. Passacantando, A. Verna, G. Impellizzeri, A. Irrera and F. d'Acapito, *J. Phys.: Condens. Matter* **22**, 216006 (2010). [Cited on page(s) 5.]
- [31] C. Bihler, C. Jaeger, T. Vallaitis, M. Gjukic, M. S. Brandt, E. Pippel, J. Woltersdorf and U. Gösele, *Appl. Phys. Lett.* **88**, 112506 (2006). [Cited on page(s) 5.]

-
- [32] A. Hirohata, Y. B. Xu, C. M. Guertler, J. A. C. Bland, and S. N. Holmes, *J. Magn. Magn. Mater.* **226-230**, 914 (2001). [Cited on page(s) 6.]
- [33] C. Zeng, S. C. Erwin, L. C. Feldman, A. P. Li, R. Jin, Y. Song, J. R. Thompson and H. H. Weitering, *Appl. Phys. Lett.* **83**, 5002 (2003). [Cited on page(s) 6, 29, and 105.]
- [34] C. Zeng, W. Zhu, S. C. Erwin, Z. Zhang, and H. H. Weitering, *Phys. Rev. B* **70**, 205340 (2004). [Cited on page(s) 6 and 105.]
- [35] L. Sangaletti, D. Ghidoni, S. Pagliara, A. Goldoni, A. Morgante, L. Floreano, A. Cossaro, M. C. Mozzati, and C. B. Azzoni, *Phys. Rev. B* **72**, 035434 (2005). [Cited on page(s) 6 and 105.]
- [36] L. Sangaletti, E. Magnano, F. Bondino, C. Cepek, A. Sepe, and A. Goldoni, *Phys. Rev. B* **75**, 153311 (2007). [Cited on page(s) 6 and 105.]
- [37] S. Olive-Mendez, A. Spiesser, L. A. Michez, V. Le Thanh, A. Glachant, J. Derrien, T. Devillers, A. Barski, and M. Jamet, *Thin Solid Films* **517**, 191 (2008). [Cited on page(s) 6.]
- [38] J. Hirvonen Grytzeli, H. M. Zhang, and L. S. O. Johansson, *Phys. Rev. B* **86**, 125313 (2012). [Cited on page(s) 6 and 105.]
- [39] P. De Padova *et al.*, *Surf. Sci.* **605**, 638 (2011). [Cited on page(s) 6 and 107.]
- [40] A. Truong, A. O. Watanabe, P. A. Mortemousque, K. Ando, T. Sato, T. Taniyama, and K. M. Itoh, *Phys. Rev. B* **91** 214425 (2015). [Cited on page(s) 6, 96, and 111.]
- [41] A. Spiesser, I. Slipukhina, M. T. Dau, E. Arras, V. Le Thanh, L. Michez, P. Pochet, H. Saito, S. Yuasa, M. Jamet, and J. Derrien, *Phys. Rev. B* **84**, 165203 (2011). [Cited on page(s) 6.]
- [42] R. P. Panguluri, C. Zeng, H. H. Weitering, J. M. Sullivan, S. C. Erwin, and B. Nadgorny, *Phys. Stat. Sol.* **242**, R67 (2005). [Cited on page(s) 6.]
- [43] K. Inomata, S. Okamura, R. Goto, and N. Tezuka, *Jpn. J. Appl. Phys.* **42**, L419 (2003). [Cited on page(s) 6.]
- [44] J. Schamlhorst, S. Kämmerer, M. Sacher, G. Reiss, A. Hütten, and A. Scholl, *Phys. Rev. B* **70**, 024426 (2004). [Cited on page(s) 6.]
- [45] C. T. Tanaka, J. Nowak, and J. S. Moodera, *J. Appl. Phys.* **81**, 5515 (1997). [Cited on page(s) 6.]

Chapter 2

Thin film growth and structural characterization

This chapter mainly deals with the principles of epitaxial growth. Because it allows the growth of films with high crystal quality, the molecular beam epitaxy technique is a very important tool for this work, therefore a description of its working mechanism will be given in section 2.1. The solid phase epitaxy is a particular case of epitaxial growth process, which is used for Mn_5Ge_3 thin films in this thesis, and it will also be explained. In section 2.2, the fundamentals of reflection high-energy electron diffraction will be discussed, since the technique allows the in-situ characterization of the surface of the samples. In section 2.3 a structural analysis of the Mn_5Ge_3 thin films is provided, and finally, the crystallography of Mn_5Ge_3 for the x-ray diffraction analysis will be described in section 2.4.

2.1 The molecular beam epitaxy technique

2.1.1 The fundamentals of epitaxial growth

MBE apparatus The growth of epitaxial thin films has become a fascinating area in solid state physics because of the challenge it represents to properly identify the atomic processes and their interaction that lead to certain morphologies for the films. The term “epitaxial growth” refers to the growth of a crystalline layer on the surface of a crystalline substrate, where the crystalline order of the grown layer is imposed by the crystallographic orientation of the surface of the substrate. The notion of epitaxy and the growth mechanisms will be discussed in the next paragraph. Molecular beam epitaxy (MBE) is a technique for epitaxial thin film deposition from molecular or atomic beams on a crystalline substrate under ultra-high vacuum (UHV) conditions. Typically, UHV conditions correspond to a background pressure less than 10^{-8} Pa, which guaranties minimal interference between impurities and the molecular beams or the substrate. Under such conditions, the mean free path of molecules in the MBE chamber is at the order of several kilometers, which is way above the dimensions of the growth chamber, thus making the MBE chamber not accountable for being a source of impurities in the grown materials. The low growth rates used in the MBE technique allow a precise control of the number of deposited layers and the morphology of the surface by allowing the atoms or molecules to organize on the surface of the substrate. Relatively low substrate temperatures can also be used to perform out-of-equilibrium growth by decreasing the reactivity of the grown material with the substrate, thus allowing to obtain layers in a metastable state when required. In the case of this work, the atomic beams are generated by Knudsen-type effusion cells [see Fig. 2-1(a)] that contain solid sources of the elements used for the growth of the

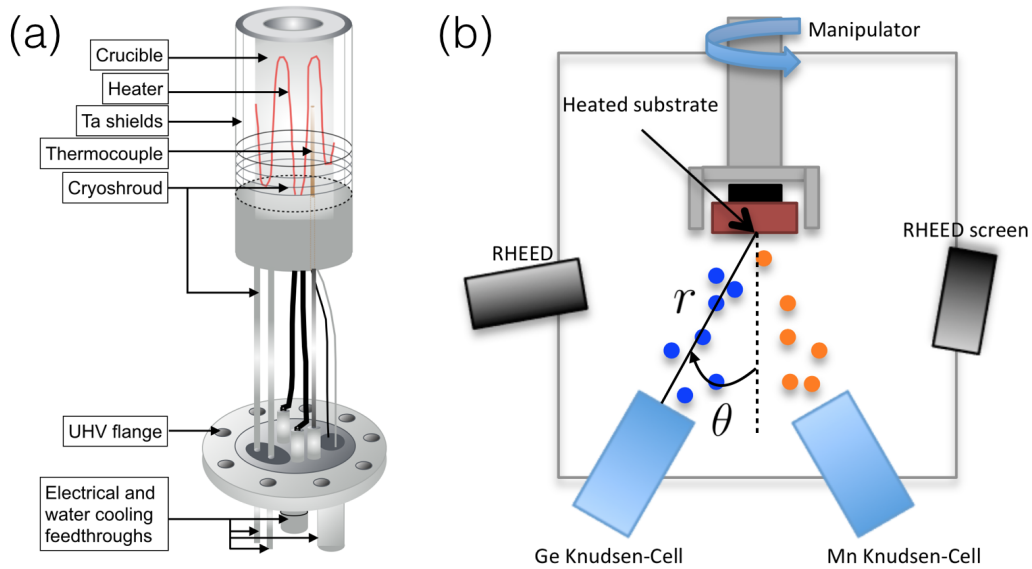


Figure 2-1: (a) Schematic of a Knudsen-type effusion cell. (b) Schematic representation of the MBE growth chamber. The angle θ is the angle between the normal axis of the substrate holder and the furnace axis of the Knudsen cell. The RHEED is a method for monitoring the quality of the surface and will be discussed later.

epitaxial thin films.

The Knudsen cells have cone-shaped pyrolytic boron nitride (PBN) crucibles, with large apertures to increase the atom flux. PBN can resist to temperatures up to 1300° and starts to outgas at appreciable rates for temperatures above this limit. Each crucible contains a solid source and is heated by a furnace pointing towards the substrate. Each furnace is connected to a tungsten-rhenium thermocouple ($W_{0.95}Re_{0.05}/W_{0.74}Re_{0.26}$ stable up to $2320^\circ C$) in order to monitor and control the temperature within the cell. The flux of the atom beam is strongly dependent on the temperature of the Knudsen cell. Under the assumption that the size of the cell aperture is lower than the mean free path of the vapor molecule/atom inside the cell, one can apply the ideal gas law to evaluate the molecular/atomic flux j from the

effusion cell. For an isotropic effusion, one obtains [1]:

$$j = \frac{A}{\pi r^2} \frac{P_{\text{K-cell}}}{(2\pi m k_B T_{\text{K-cell}})^{1/2}} \cos \theta, \quad (2.1)$$

where A is the aperture size of the cell, r is the distance between the cell and the substrate, m is the molecular mass, k_B is the Boltzmann constant, $P_{\text{K-cell}}$ is the equilibrium vapor pressure in the cell and $T_{\text{K-cell}}$ is the cell temperature. The parameters r and θ are defined in Fig. 2-1(b).

In reality, the effusion is not isotropic and the flux also depends on the quantity of source remaining in the cell, more precisely on the volume occupied by the source in the crucible. Consequently, in practice it is important to calibrate the growth rate of each cell on a regular basis. For such calibration, some MBE machines are equipped with a quartz microbalance, which is sensitive to the number of monolayers deposited on the substrate. In the present work, ex-situ x-ray reflection (XRR) measurements are performed to evaluate the thickness of the reference samples for the calibration.

The different growth modes The description of the epitaxial growth mode originally came from three distinct theories [2] that were later shown to be complementary and thus were unified. The Frank-van der Merwe model employed the elasticity theory to describe the existence of a critical misfit, which appears in the monolayer-by-monolayer growth mechanism [3]. The Volmer-Weber model assumed a three-dimensional growth mode and the crystalline thin films are formed from the three-dimensional nuclei on the substrate. The relative number of nuclei and their growth rate depends on the surface energy of the substrate and the energy of the interface between the substrate and the grown material [4]. The Stranski-Krastanov model assumed that the initial step of the growth was the formation of a few two-

dimensional layers, and then a three-dimensional growth mode occurs on top of the two-dimensional layers [5]. The three growth modes of epitaxy are illustrated in Fig. 2-2 and can be summarized as follows:

- The Frank-van der Merwe (FM) mode: two-dimensional, **layer-by-layer** growth mode.
- The Volmer-Weber (VW) mode: three-dimensional, **island** growth mode.
- The Stranski-Krastanov (SK) mode: initially two-dimensional and then three-dimensional after a critical thickness, **layer-plus-island** growth mode.

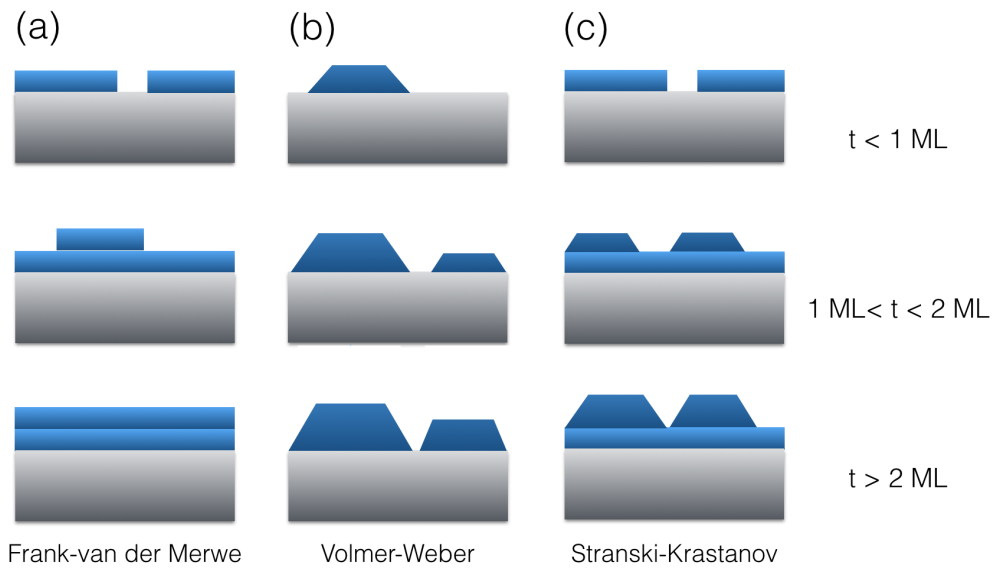


Figure 2-2: The three different growth modes at different stages of the growth defined by the number of deposited monolayers (ML): (a) FM mode, (b) VW mode, and (c) SK mode.

The unification of the three theories on the growth modes [6] was done by considering a thermodynamical approach, involving the surface tensions for the different interfaces: $\gamma_{\text{overlayer}}$, $\gamma_{\text{substrate}}$, and $\gamma_{\text{interface}}$, which correspond to the surface free energy at the overlayer/vacuum interface, the substrate/vacuum interface, and the

overlayer/substrate interface respectively. The relative magnitude of those surface energies will determine the growth mode for a given material on a given substrate. Indeed, when $\gamma_{\text{overlayer}}$ and $\gamma_{\text{interface}}$ are small compared to $\gamma_{\text{substrate}}$, the formation of the overlayer/substrate interface will be favored and the grown layer will wet and cover the surface of the substrate, thus leading to a FM growth mode. On the contrary, if the relationship between the surface energies is reversed, one will obtain layers that partially cover the surface due to the unfavorable formation of interfaces between the overlayer and the substrate, which corresponds to a VW growth mode. Therefore, for a film made of n monolayers, the criterion for a FM growth mode is given by:

$$\gamma_{\text{overlayer}}(n) + \gamma_{\text{interface}}(n) \leq \gamma_{\text{substrate}} \quad (2.2)$$

Equality in Eq.(2.2) can be obtained in the case of homoepitaxy, for which an epitaxial growth in the FM mode is usually verified if the growth is performed in the thermodynamic equilibrium conditions. For the case of heteroepitaxy, since $\gamma_{\text{interface}}(n)$ is usually non-negligible, the FM mode is only obtained for $\gamma_{\text{overlayer}}(n) \ll \gamma_{\text{substrate}}$. Thus the growth mode becomes a VW mode for $\gamma_{\text{overlayer}}(n) > \gamma_{\text{substrate}}$.

The dependence of $\gamma_{\text{overlayer}}$ and $\gamma_{\text{interface}}$ on n takes into account the variation of free energy due to the strain accumulation or the change in lattice constant in the overlayer [7]. For the case of heteroepitaxial growth, the lattice mismatch between the overlayer and the substrate increases monotonously with the film thickness until the critical thickness, given by a critical number of layers n_c , is reached. As a result, due to the existence of n_c , the relation given by Eq.(2.2) changes into $\gamma_{\text{overlayer}}(n) + \gamma_{\text{interface}}(n) > \gamma_{\text{substrate}}$ for thicknesses above the critical value, thus switching the growth mode from a two-dimensional mode to a three-dimensional one. This phenomenon reflects an epitaxial growth in the SK mode.

The consideration on the surface energies is valid when the growth is performed close to the thermodynamic equilibrium. However, as mentioned above, the epitaxial growth can be done out-of-equilibrium, thus it is ruled by kinetics rather than thermodynamics. The kinetic process of the growth is determined by the migration of the atoms on the surface and energy barriers they encounter in the migration path. The energy barriers define the diffusion rates and the morphologies of the film. A kinetic growth process has the advantage of yielding metastable morphologies for the thin films, which are not accessible close to the thermodynamic equilibrium. The atomic processes at the surface are summarized in Fig. 2-3.

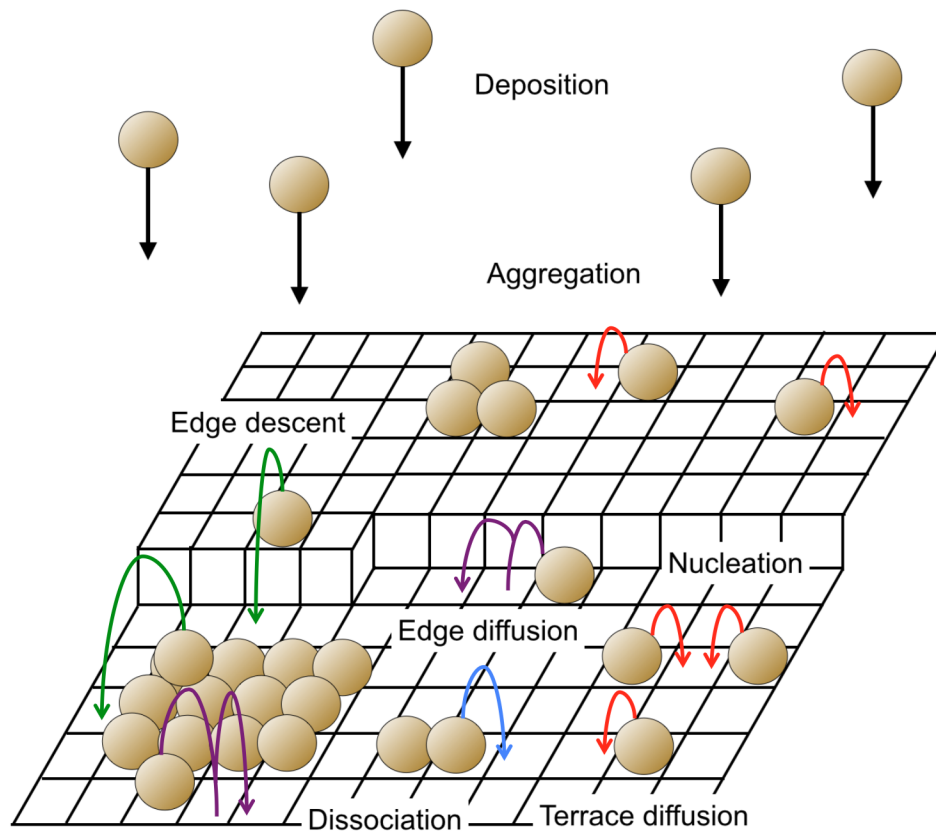


Figure 2-3: Atomic diffusion processes occurring at the surface during the epitaxial growth, when the deposition is performed far from the thermodynamical equilibrium.

2.1.2 The solid phase epitaxy

The solid phase epitaxy is a process which consists in the recrystallization of an amorphous layer of a material grown on a single crystal, by thermal annealing. Atoms from the disordered layer get reconstructed on the single crystal template layer by layer. This method proved to be convenient for the fabrication of nanometer scale devices [8, 9, 10]. It is also an attractive process that can be used to regenerate the crystallinity of a semiconductor locally damaged and amorphized by the ion implantation doping technique [11]. However, despite its apparent simplicity, the solid phase epitaxy is actually a complicated process, which involves many effects such as the roughening of the amorphous-crystalline interface, the creation of defects, the diffusion of impurities, all of which depend on the growth conditions and solid state regrowth rate. Theoretical models [12, 13, 14] have been proposed in order to describe the mechanisms behind the migration of the amorphous-crystalline interface, although they will not be discussed here because they depend on the nature of the materials. Although solid phase epitaxy is a commonly used method for fabricating Mn_5Ge_3 on Ge(111), mathematical models for the $\text{Mn}_5\text{Ge}_3/\text{Ge}$ interface motion have not been established so far.

In the case of amorphous silicon on crystalline silicon, the solid state regrowth mechanism during the thermal annealing is shown to be anisotropic, i.e. to depend on the crystalline orientation of the substrate [100], [110], and [111] (see Ref. [15]). For the interface migration in the [100] direction, the process is quasi-planar, involving a diffusion of atoms in the amorphous layer followed by a partial ordering at the amorphous-crystalline interface. The propagation of the interface is done by the incorporation of other atoms. Regarding the [110] direction, the recrystallization front has a roughness of a few atomic planes. The solid phase epitaxy in the [111]

direction is the most complex, involving a non-planar propagation of the interface and the formation of defects, like twins. The recrystallization in [110] and [111] actually involve two regrowth modes with different interface migration velocities [11].

In case of heteroepitaxy, which is of higher interest in the present work, the difference of lattice mismatch between the materials favors the formation of misfit dislocations in order to relieve the strain beyond a critical thickness. As an example, for the case of the regrowth of SiGe on Si, it is shown that there exists a defect-free region [16, 17], whose thickness depends on the Ge concentration. Indeed incorporating more or less Ge in SiGe has an influence on the strain in the heterostructure. During the regrowth the amorphous part is usually considered to undergo negligible strain compared to the recrystallized part. As the thickness of the recrystallized part increases through the propagation of the amorphous-crystalline interface, it accumulates strain, which leads to the nucleation of defects above the critical thickness thus causing the interface to roughen and slowing down solid phase epitaxy velocity [16, 17].

This work deals with the case of Mn_5Ge_3 on Ge(111). The purpose of the previous examples is to show that solid phase epitaxy actually involves a complex mechanism. A detailed study of the solid phase epitaxy process would be necessary in order to be able to understand the mechanism of interface propagation, to have a better control of the thickness of epitaxial layer, and to understand the reason why a relatively flat $\text{Mn}_5\text{Ge}_3/\text{Ge}$ interface can be formed. Consequently, growth parameters such as the annealing temperature and the annealing time have an important effect on the quality of a film crystallized by the solid phase epitaxy technique.

2.2 Reflection high-energy electron diffraction

RHEED instrumentation Reflection high-energy electron diffraction (RHEED) is a technique for surface analysis, which has become widely used because of its compatibility with methods of vapor deposition and growth of epitaxial thin films under ultra-high vacuum, thus allowing thin film growth and analysis simultaneously. The implementation only requires an electron gun, a phosphor screen and a clean surface for the sample to analyze. The typical range of energy for the finely collimated electron beam is from 8 to 20 KeV, although energies as high as 100 keV can be used in some cases. RHEED is mainly sensitive to the structure in the first few atomic planes of a crystal lattice, due to the interaction between the electrons and the atoms which only allows a small penetration depth of the incident electrons. The electron beam is directed at very low incidence angle to the surface of the sample, thus having important effects on the resulted diffraction patterns. For example, atomic steps can result in significant changes in the intensity and the shape of the diffracted beam.

The RHEED patterns are commonly used to extract information about [18]: the periodicity in atomic arrangement, the flatness of the surface, the size of the grains or domains of surface structures, epitaxial relation between the grown film and the substrate, growth style of thin films and numbers of atomic layer grown. The RHEED apparatus is described in Fig. 2-4. The incident angle θ_g of the electron beam can be changed by deflection coils, and θ_g should be less than a few degrees. Due to the grazing incidence, the RHEED pattern is usually an average in a macroscopic area.

It is also common to place a CCD camera in front of the phosphor screen in order to record the RHEED intensity as a function of time. The RHEED intensity is a periodic function of time and the period corresponds to the time required for the growth of one monolayer [20, 21, 22]. However, such method was not used in the

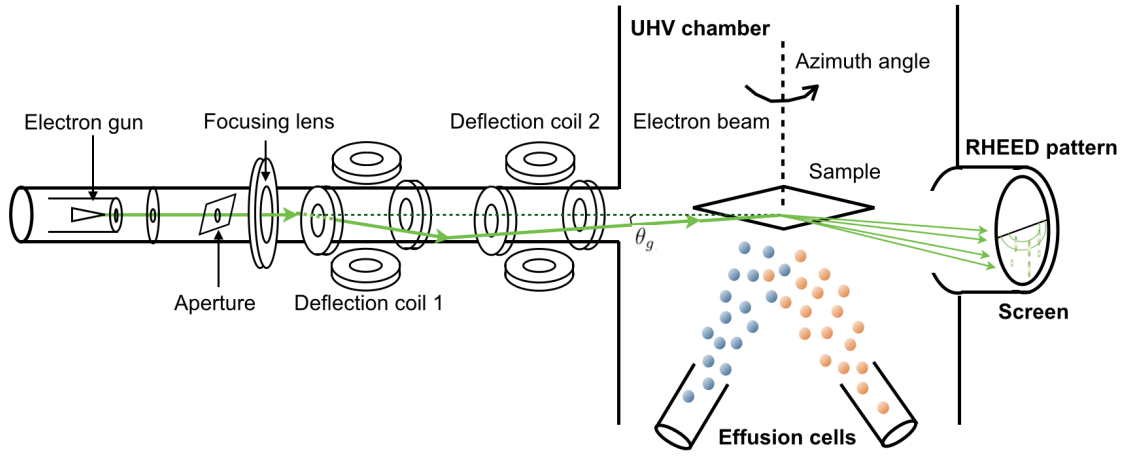


Figure 2-4: Representation of RHEED apparatus. The electron gun accelerates the electrons through a small aperture. The deflection coils are used to modify the glancing angle θ_g of the electron beam on the surface of the sample.

present work, additional ex-situ measurements were performed instead.

Ewald construction and surface lattices The Ewald construction combines energy and momentum conservation, and establishes the relation between the reciprocal space and the geometrical features of a RHEED pattern. The diffraction condition is based on the occurrence of constructive interference. If one considers elastic scattering, the magnitude of the wavevector (\mathbf{k}) is the same for incident (θ_g) and diffracted (θ_f) waves. The parallel components of the incident and diffracted waves must differ by a multiple of 2π times the reciprocal lattice constant ($1/a$):

$$k \cos \theta_g - k \cos \theta_f = \frac{2\pi n}{a}. \quad (2.3)$$

Because of the elastic scattering, the end points of the diffracted wavevectors describe a sphere with radius k , which is called the Ewald sphere. In the hypothesis on an elastic scattering, the center of the sphere is the common origin for all the diffracted waves. The Ewald sphere intersects with the reciprocal lattice and results in a series

of concentric circles, each of which corresponds to a Laue zone. In a square lattice of equidistant atoms [see Fig. 2-5(a)], the reciprocal lattice is the intersection of the two series of planes rotated by 90° to each other, which is a set of rods. As a result, when both elastic scattering and diffraction condition are verified, the RHEED pattern emerges from the intersection between the Ewald sphere and the rods in the reciprocal space, thus leading to diffraction spots [see Fig. 2-5(c)]. Consequently, the diffraction spots are always located on concentric circles in the case of RHEED. The spots can be elongated into streaks depending on the incident angle of the electron beam and the crystal domain size at the surface of the sample. An explanation of the RHEED streaks is given in Fig. 2-5.

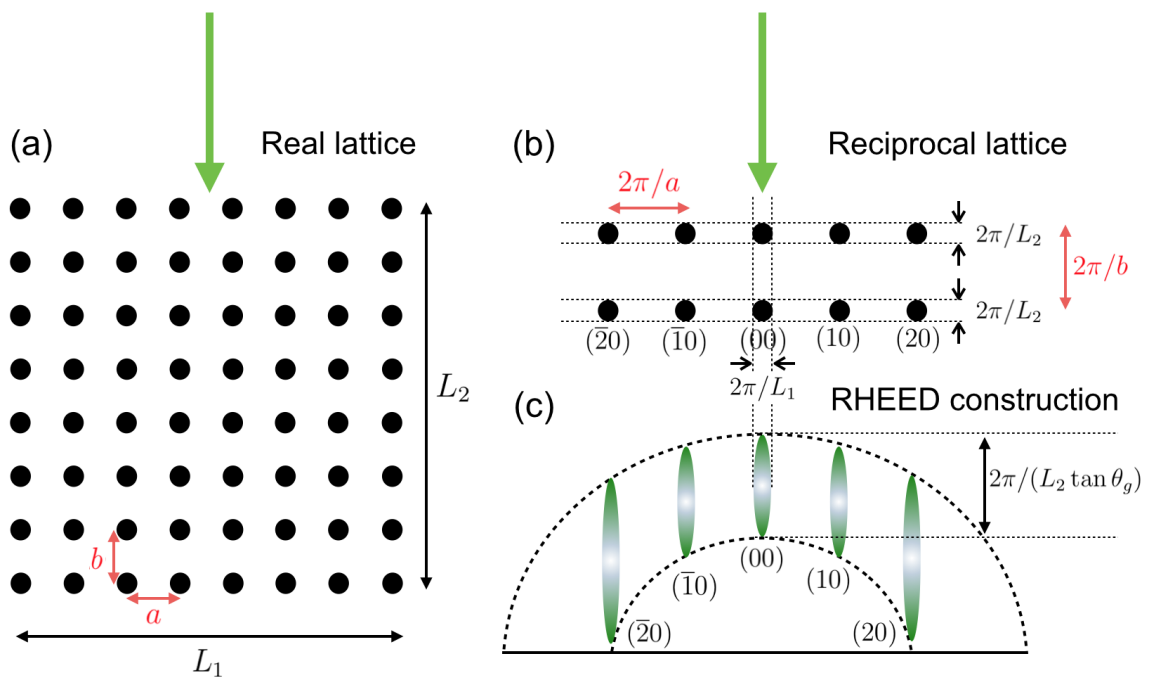


Figure 2-5: Origin of the RHEED streaks. The vertical arrow defines the direction of the electron beam. (a) Arrangement of the two-dimensional array of lattice points in the real space. (b) Reciprocal lattice for the arrangement in (a). (c) RHEED construction obtained from (b). The length of the streaks depend on the glancing angle θ_g and the size of the domains at the surface.

Because the coordination of atoms at the surface is not the same as in the bulk, the atoms at the surface can undergo rearrangements in order to minimize the surface energy, this process is called *surface reconstruction*. Depending on the type of reconstruction, the periodicity at the surface may differ from that of the bulk crystal. Since the RHEED patterns only give information about a few layers from the surface, one needs to define two-dimensional lattices that may be different from the full three-dimensional lattices. Such two-dimensional lattice can be given by the vector

$$\mathbf{R}_n = n_1 \mathbf{a}_1 + n_2 \mathbf{a}_2, \quad (2.4)$$

where n_1 and n_2 are integers, and \mathbf{a}_1 and \mathbf{a}_2 are the unit mesh vectors of the surface lattice. Similar to the case of three-dimensional lattices, a reciprocal vector can be defined by $\mathbf{B}_m = m_1 \mathbf{a}_1^* + m_2 \mathbf{a}_2^*$, where

$$\begin{aligned} \mathbf{a}_1^* &= 2\pi \frac{\mathbf{a}_2 \times \mathbf{n}}{\mathbf{a}_1 \cdot (\mathbf{a}_2 \times \mathbf{n})} \\ \mathbf{a}_2^* &= 2\pi \frac{\mathbf{a}_1 \times \mathbf{n}}{\mathbf{a}_2 \cdot (\mathbf{a}_1 \times \mathbf{n})} \end{aligned} \quad (2.5)$$

The vector \mathbf{n} is the unit vector normal to the surface of the sample. The base vectors of the reconstructed surface \mathbf{b}_1 and \mathbf{b}_2 can be expressed as a function of the fundamental basis vectors \mathbf{a}_1 and \mathbf{a}_2 as follows:

$$\begin{pmatrix} \mathbf{b}_1 \\ \mathbf{b}_2 \end{pmatrix} = \begin{pmatrix} n_{11} & n_{12} \\ n_{21} & n_{22} \end{pmatrix} \begin{pmatrix} \mathbf{a}_1 \\ \mathbf{a}_2 \end{pmatrix} \quad (2.6)$$

Thus the reconstructed surface lattice and the bulk structure are related to each other by a transformation matrix. The reconstructed surface can also be labeled in

Wood's notation, e.g. 2×1 structure of Si(001). The spots on the 0th and 1st Laue zone, called fundamental spots, are usually strong in intensity and originate from the scattering not only from the topmost atomic layer but also several atomic layers in the bulk region. Between the fundamental spots, one can find the superlattice spots, which correspond to the reconstructed surface. By analyzing the spacings between the superlattice spots and compare them with that of the fundamental spots, one can find the periodicity of the unit cell of the reconstructed surface.

In practical cases, the surfaces of the samples are not ideal [18]. The surfaces may not be totally flat or they possess domains with various sizes, similar to polycrystals. Consequently, the RHEED patterns are modified from the ideal case (see Fig. 2-6 for the most common cases), thus giving information on the nature of the surface imperfections. The width of the reciprocal rod is inversely proportional to the average size of the domain, so sharp patterns featuring dots imply large domain sizes [Fig. 2-6(a)] contrary to elongated streak patterns, which correspond to smaller domain sizes [Fig. 2-6(b)]. Steps at the surface lead to modulated patterns [Fig. 2-6(c) and (d)]. Vicinal surfaces result in inclined streaks [Fig. 2-6(e)]. A three-dimensional growth mode in MBE is usually recognized by the presence of transmission spots in the RHEED pattern, as illustrated in Fig. 2-6(f).

Inelastic scattering of electrons, involving phonons and plasmons [23, 24], also have an influence on the RHEED patterns, resulting in the so-called Kikuchi lines. The Kikuchi lines depend on the morphology of the surface, and sharp lines are obtained crystal for perfect surfaces and bulk lattices [19]. The formation of the Kikuchi lines will not be discussed here.

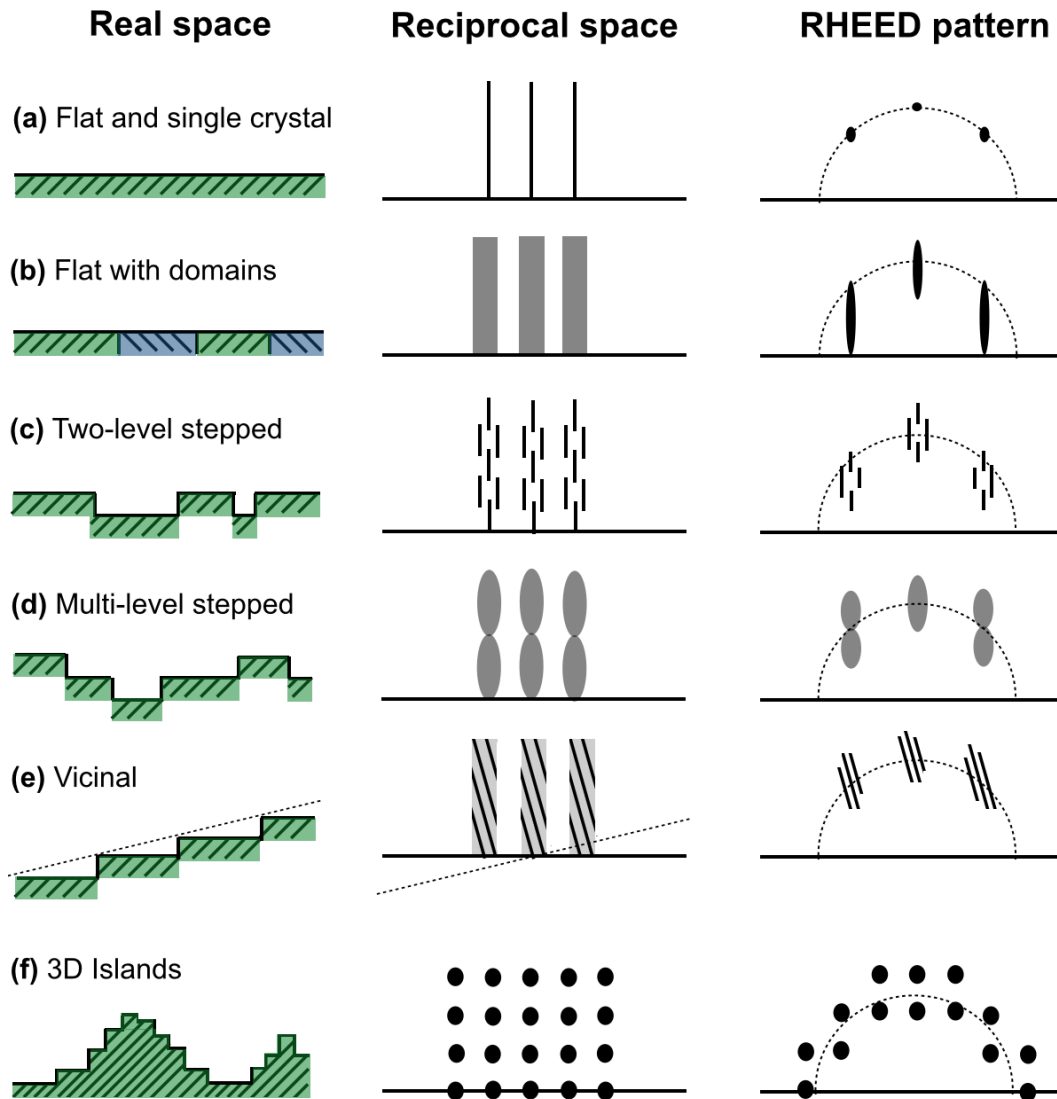


Figure 2-6: Schematic representation of the morphology of the RHEED patterns depending on the kind of surface. Imperfections in the structure of the surface can affect the RHEED pattern: (a) sharp spots appear for perfectly flat and single crystalline surfaces, (b) streaks are obtained for flat surfaces with smaller domain sizes, (c) satellite streaks and (d) modulated streaks correspond to multi-level steps on the surface, (e) inclined streaks are the result of vicinal surfaces, and (f) transmission spots are the sign of three-dimensional growth.

2.3 The $\text{Mn}_5\text{Ge}_3(001)/\text{Ge}(111)$ epitaxial relation

In this thesis, the Mn_5Ge_3 thin films were grown by using the MBE technique, at a base pressure lower than 8×10^{-8} Pa. Solid phase epitaxy proved to be the most efficient way to grow Mn_5Ge_3 . Indeed, a codeposition of Mn and Ge requires a perfect calibration of the relative flux of the two respective Knudsen-cells in order to get the precise stoichiometry. Any small deviations of flux led to unwanted stoichiometries. The quality of the sample's surface was monitored in-situ by RHEED, in both $[1\bar{1}0]$ and $[11\bar{2}]$ directions of the Ge(111) substrate. The sample's internal structure was observed ex-situ by transmission electron microscopy (TEM).

The substrate was degassed at 600°C for 2 hours. A Ge buffer layer was grown on the Ge(111) substrate at a substrate temperature T_{sub} of 600°C , in order to keep a good crystallinity. An annealing at 700°C for 1 hour followed by a cooling below 200°C resulted in the well-known $c(2 \times 8)$ reconstruction of the clean Ge(111) surface [Figs. 2-7(a) and 2-7(b)]. Mn was then deposited on this $c(2 \times 8)$ surface at $T_{\text{sub}} = 40^\circ\text{C}$. The RHEED patterns during the growth of the Mn layer revealed a three-dimensional growth, characterized by the presence of transmission spots [Figs. 2-7(c) and 2-7(d)]. A solid-state reaction between manganese and germanium was activated by annealing the sample at T_{SPE} , leading to the $\sqrt{3} \times \sqrt{3}$ reconstruction, indicating the (001) surface of Mn_5Ge_3 [Figs. 2-7(e) and 2-7(f)]. In this work, several samples were grown by choosing T_{SPE} from 150 to 450°C . In order to prevent the manganese germanide layer from oxidizing, which is crucial to keep its magnetic properties, an amorphous Ge capping layer was grown with a low growth temperature so that the segregation of Mn_5Ge_3 to the surface is suppressed. Such segregation was demonstrated in Ref. [25]. The thickness of the deposited Mn layer was 11.4 or 22.8

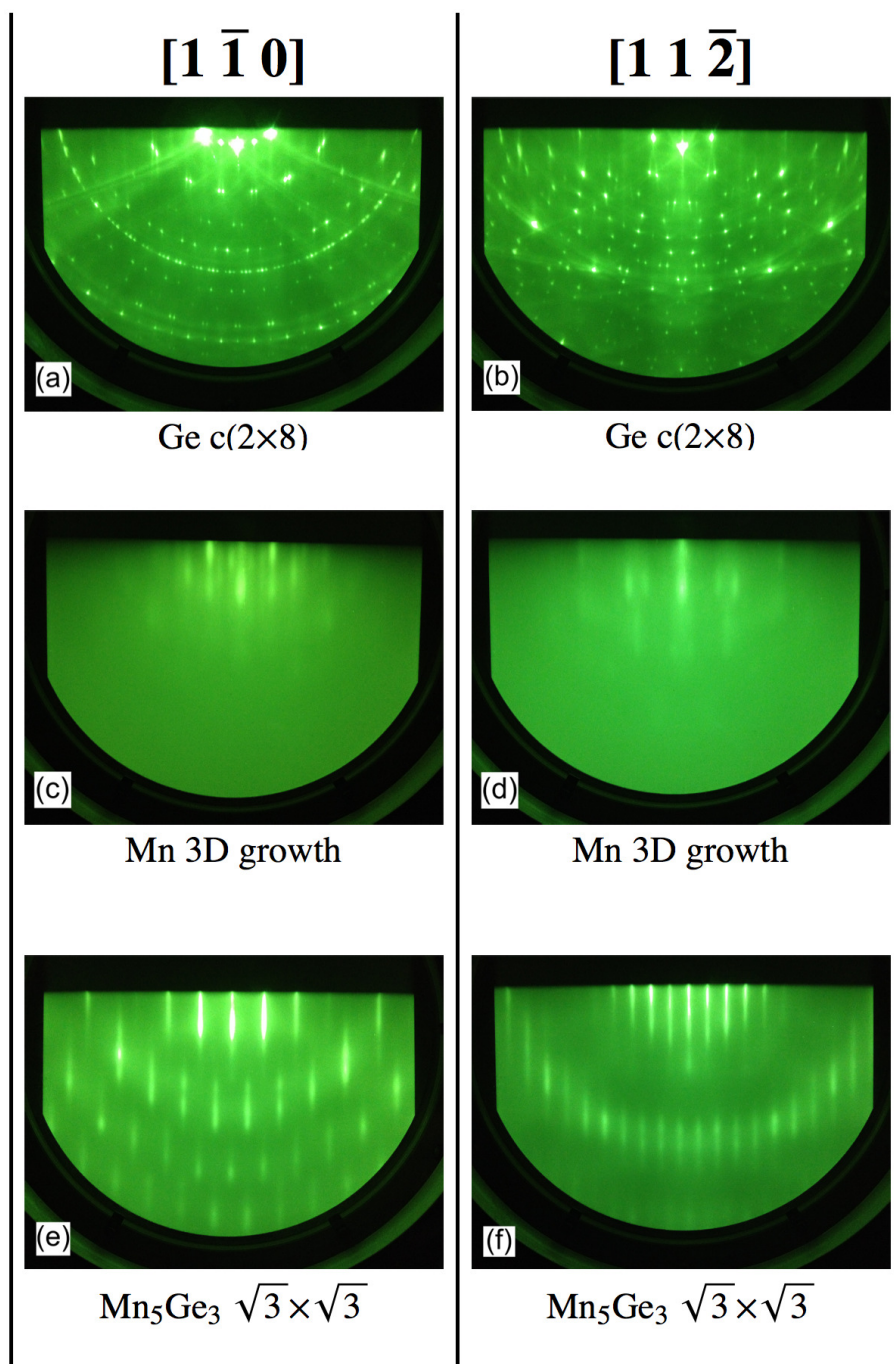


Figure 2-7: RHEED patterns in the $[1\bar{1}0]$ and $[11\bar{2}]$ directions of the Ge(111) substrate, with an acceleration energy of 12 keV, at different steps of the growth: (a) and (b) the $c(2 \times 8)$ reconstructed surface of Ge buffer layer; (c) and (d) transmission patterns after the growth of the Mn layer; (e) and (f) the $\sqrt{3} \times \sqrt{3}$ structure of Mn_5Ge_3 after the solid state reaction.

nm, depending on the sample. During the post-Mn-deposition annealing, a part of the Ge buffer layer was consumed for the solid-state growth to form a 17 or 33 nm thick Mn_5Ge_3 layer. In order to confirm the crystallographic structure of the samples, x-ray diffraction (XRD) patterns were measured by performing θ - 2θ scans on the thin film. A pure Ge(111) substrate was also measured by XRD, as a reference sample. In the obtained XRD spectra shown in Fig. 2-8, we identified the peaks from the Ge(111) substrate and the $\text{Mn}_5\text{Ge}_3(001)$ film, which are consistent with the results obtained in previous studies [26, 27]. According to this XRD pattern, the lattice parameters were $a(\text{Ge}) = 5.664 \text{ \AA}$ for the cubic Ge, consistent with the value found in literature [28], and $c(\text{Mn}_5\text{Ge}_3) = 5.057 \text{ \AA}$ for the hexagonal Mn_5Ge_3 . The hexagonal basal plane lattice parameter of Mn_5Ge_3 was evaluated to be $a(\text{Mn}_5\text{Ge}_3) = 7.112 \text{ \AA}$, by using an off-normal angle XRD measurement. The unit cell parameters of the Mn_5Ge_3 film measured in this work are close to the values found for the bulk [29] and consistent with the previous work on thin films [30]. Energy dispersive x-ray (EDX) measurements of the Mn-Ge layer showed a Mn:Ge composition of 62%:38%, which corresponds to the stoichiometry in Mn_5Ge_3 . The homogeneity of the composition was confirmed by performing EDX measurements at many random locations in the manganese germanide layer. The cross-sectional TEM images in Fig. 2-9 show the structure of the Mn_5Ge_3 thin film on the Ge(111) buffer layer. One can see that the growth is epitaxial, with no clusters and the interfaces are relatively smooth.

Moreover, it is found that Mn_5Ge_3 always forms coherently on Ge(111), with its hexagonal [010] in-plane direction always being parallel to the cubic $[11\bar{2}]$ in-plane direction of the Ge substrate. This is likely due to the fact that the in-plane atomic spacing $d_{\text{Mn}_5\text{Ge}_3} = 7.112 \text{ \AA}$ in the [010] direction of Mn_5Ge_3 is about the same as the in-plane atomic spacing $d_{\text{Ge}} = 6.937 \text{ \AA}$ in the $[11\bar{2}]$ direction of Ge.

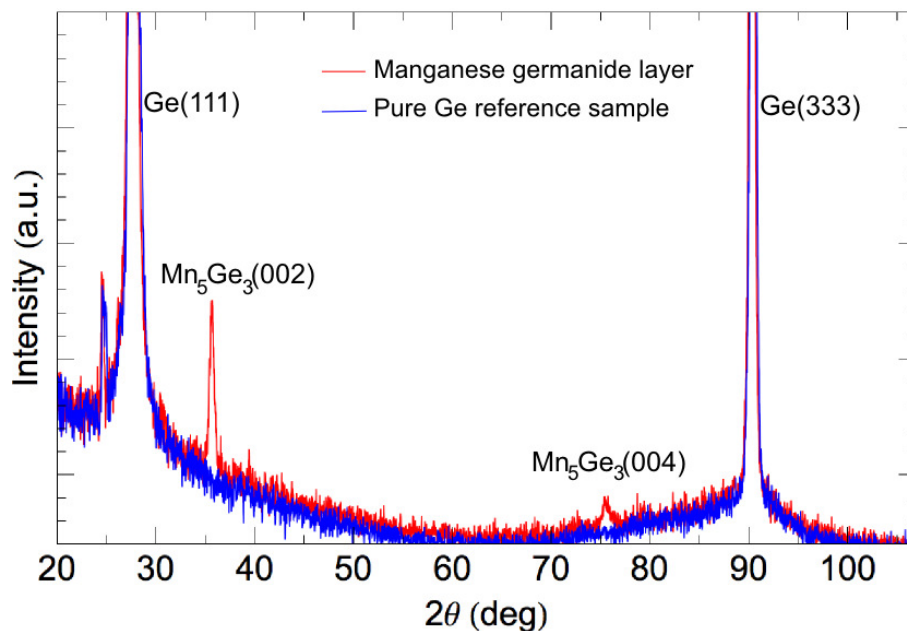


Figure 2-8: An x-ray diffraction pattern for the MBE grown Mn_5Ge_3 thin film (red curve), measured by θ - 2θ method, using $\text{Cu K}\alpha$ radiation ($\lambda = 0.15418$ nm). A pure Ge substrate has also been measured and serves as a reference (blue curve). The peak at $2\theta = 24.6^\circ$ corresponds to a signal coming from the germanium irradiated by $\text{Cu K}\beta$ radiation originating from the x-ray source.

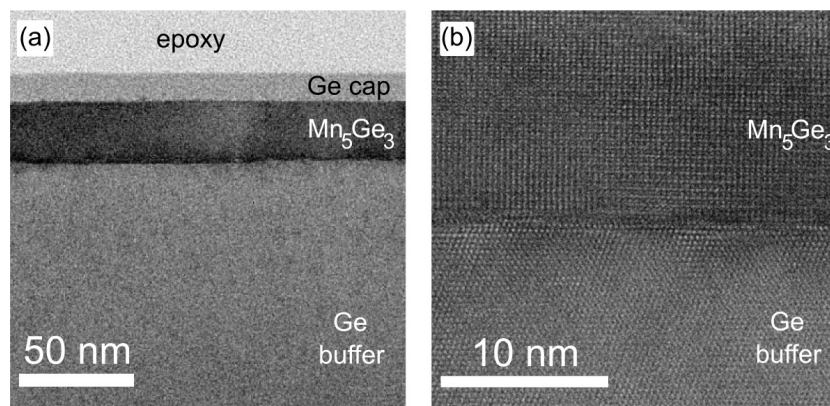


Figure 2-9: Cross-sectional TEM images of the epitaxial Mn_5Ge_3 layer. (a) An overview of the structure shows relatively smooth interfaces. (b) A close-up view on the $\text{Mn}_5\text{Ge}_3/\text{Ge}$ interface shows the epitaxial growth of $\text{Mn}_5\text{Ge}_3(001)$ on $\text{Ge}(111)$.

Although Mn_5Ge_3 epitaxial layers are stable on $\text{Ge}(111)$, the growth of epitaxial $\text{Ge}(111)$ on $\text{Mn}_5\text{Ge}_3(001)$ is proved to be unfavored, most likely due to the respective surface energies of Ge and Mn_5Ge_3 , which do not allow Ge to wet on the crystalline Mn_5Ge_3 . A high growth temperature ($T_{\text{sub}} = 600^\circ\text{C}$) is used for the growth of Ge, and such high temperature seems to favor the segregation of Mn_5Ge_3 . In an attempt to grow $\text{Mn}_5\text{Ge}_3/\text{Ge}/\text{Mn}_5\text{Ge}_3$ multilayers, the Mn_5Ge_3 layers tend to merge and float above the crystalline Ge layer, as can be seen in the TEM image shown in Fig. 2-10. It is therefore difficult to realize $\text{Mn}_5\text{Ge}_3/\text{Ge}/\text{Mn}_5\text{Ge}_3$ heterostructures. In Ref. [25], the deposition of a carbon delta-layer allowed to prevent the segregation of the Mn_5Ge_3 epitaxial layer and an single crystalline layer of Ge could be grown on top the the carbon delta-layer. However, the orientation of the overgrown Ge layer was $[100]$ and not $[111]$.

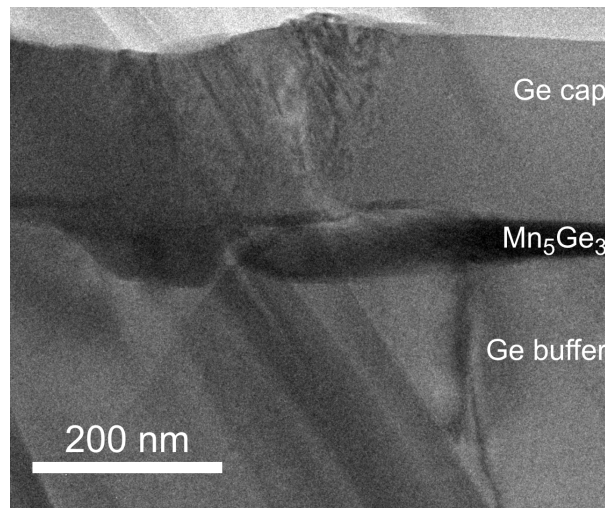


Figure 2-10: This sample was intended to be a $\text{Mn}_5\text{Ge}_3/\text{Ge}/\text{Mn}_5\text{Ge}_3$ multilayer. The TEM image shows that an epitaxial layer of Ge cannot be stabilized on Mn_5Ge_3 , probably due to a surface energy effect. The roughness of the $\text{Mn}_5\text{Ge}_3/\text{Ge}$ interface became high and some defects are visible in the Ge layer.

Attempts to grow a crystalline Ge layer on Mn_5Ge_3 usually results in mixed $c(2 \times 8)$ and $\sqrt{3} \times \sqrt{3}$ patterns, indicating that the surface is made of mixture of Ge domains and Mn_5Ge_3 domains [Fig. 2-11 (a) and (b)]. This shows that during the growth of Ge on Mn_5Ge_3 , the high growth temperature makes Mn_5Ge_3 segregate to the surface. By comparing the $c(2 \times 8)$ and $\sqrt{3} \times \sqrt{3}$ patterns in Figs. 2-7 and 2-11, one can notice that the streaks in the $\sqrt{3} \times \sqrt{3}$ pattern are elongated while the Ge(111) surface shows sharp spots. As a result, the domain size of the Ge(111) surface is larger than that of the $\text{Mn}_5\text{Ge}_3(001)$ surface.

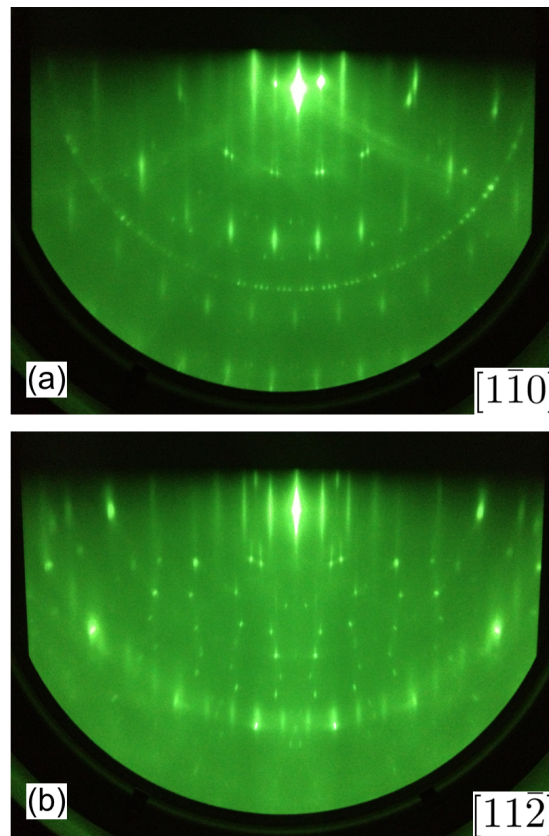


Figure 2-11: Mixed $c(2 \times 8)$ and $\sqrt{3} \times \sqrt{3}$ RHEED patterns in the (a) $[\bar{1}\bar{1}0]$ and (b) $[\bar{1}\bar{1}2]$ directions of the Ge substrate. Such patterns indicate that both Ge domains and Mn_5Ge_3 domains are present at the surface. The Ge domains do not cover the entire surface during the growth of Ge on Mn_5Ge_3 at high growth temperatures, typically 600°C .

2.4 The crystallography of Mn_5Ge_3

Crystallographic notations and formulae In general, a Bravais lattice is identified by the six lattice parameters, (a, b, c) in lengths and (α, β, γ) in angles. Lattice points \mathbf{R} in an ideal crystal are represented with integers (X, Y, Z) as

$$\mathbf{R} = X\mathbf{a} + Y\mathbf{b} + Z\mathbf{c}, \quad (2.7)$$

which is noted briefly as $\mathbf{R} = [X \ Y \ Z]$ and used to represent a direction in the real space. Then, the unit cell volume is described for any lattice system as follows

$$\begin{aligned} V_{\text{real}} &= (\mathbf{a} \times \mathbf{b}) \cdot \mathbf{c} \\ &= abc\sqrt{1 - \cos^2 \alpha - \cos^2 \beta - \cos^2 \gamma + 2 \cos \alpha \cos \beta \cos \gamma}. \end{aligned} \quad (2.8)$$

For hexagonal lattices such as the one of Mn_5Ge_3 , the previous formula becomes

$$V_{\text{real}} = a^2 c \sin \gamma. \quad (2.9)$$

A reciprocal lattice point is represented as

$$\mathbf{G} = h\mathbf{a}^* + k\mathbf{b}^* + l\mathbf{c}^*, \quad (2.10)$$

in which, h , k , and l are integers and \mathbf{a}^* , \mathbf{b}^* , and \mathbf{c}^* are reciprocal lattice vector units, which are defined as $\mathbf{a}^* = \mathbf{b} \times \mathbf{c} / V_{\text{real}}$, $\mathbf{b}^* = \mathbf{c} \times \mathbf{a} / V_{\text{real}}$, and $\mathbf{c}^* = \mathbf{a} \times \mathbf{b} / V_{\text{real}}$, for the real lattice vector units $(\mathbf{a}, \mathbf{b}, \mathbf{c})$, which can be nonprimitive. This is briefly noted as $\mathbf{G} = (h \ k \ l)$, which is known as the Miller index notation.

A displacement vector \mathbf{d} in the real space is represented with the real numbers x , y , and z , as

$$\mathbf{d} = x\mathbf{a} + y\mathbf{b} + z\mathbf{c} = [x \ y \ z]. \quad (2.11)$$

On the other hand, a group of periodic lattice planes in the real space can be specified rather by a reciprocal lattice vector $\mathbf{G} = (h \ k \ l) = h\mathbf{a}^* + k\mathbf{b}^* + l\mathbf{c}^*$, which is normal to this plane and has a magnitude inverse to the distance d between these planes, i.e.,

$$\mathbf{G} \cdot \mathbf{d} = Gd = 1, \quad (2.12)$$

for any displacement $\mathbf{d} = \mathbf{r}_i - \mathbf{r}_j$ between an adjacent pair of planes among them. Hence, $\mathbf{d} = x\mathbf{a} + y\mathbf{b} + z\mathbf{c}$ satisfies

$$hx + ky + lz = 1, \quad (2.13)$$

indicating that the intercepts with the \mathbf{a} , \mathbf{b} , and \mathbf{c} axes are $x = 1/h$, $y = 1/k$, and $z = 1/l$, respectively, when the origin is set on one of these planes. Thus, the Miller index is used to represent both the reciprocal lattice point \mathbf{G} as in Eq. (2.10) and a group of real lattice planes satisfying Eq. (2.13). In a general case, the directions of $\mathbf{G} = (h \ k \ l)$ and $\mathbf{d} = [h \ k \ l]$ are different, while they coincide for cubic lattices.

$$\begin{aligned} \mathbf{G} \times \mathbf{d} &= (h \ k \ l) \times [h \ k \ l] \\ &= h^2\mathbf{a}^* \times \mathbf{a} + k^2\mathbf{b}^* \times \mathbf{b} + l^2\mathbf{c}^* \times \mathbf{c} \\ &\quad + kl(\mathbf{b}^* \times \mathbf{c} + \mathbf{c}^* \times \mathbf{b}) + lh(\mathbf{c}^* \times \mathbf{a} + \mathbf{a}^* \times \mathbf{c}) + hk(\mathbf{a}^* \times \mathbf{b} + \mathbf{b}^* \times \mathbf{a}). \end{aligned} \quad (2.14)$$

For an orthorhombic lattice

$$\mathbf{G} \times \mathbf{d} = kl(c/b - b/c)\mathbf{a}/a + lh(a/c - c/a)\mathbf{b}/b + hk(b/a - a/b)\mathbf{c}/c. \quad (2.15)$$

Only for a cubic lattice ($a = b = c$), this vector vanishes for arbitrary integers h , k , and l and then $(h \ k \ l)$ and $[h \ k \ l]$ are parallel to each other.

Hexagonal lattice For hexagonal lattices ($a = b$, $\alpha = \beta = 90^\circ$, and $\gamma = 120^\circ$), the four-component Miller-Bravais index may also be used in place of the three-component Miller notation. A reciprocal lattice point, and hence the corresponding lattice planes in the real space is denoted as:

$$(h \ k \ l) = (h \ k \ j \ l), \quad (2.16)$$

where the inserted third component $j = -(h + k)$ is redundant and is completely determined by the first and second components and makes no change in the actual vector \mathbf{G} . However, this notation makes it easier to find symmetrically equivalent reciprocal lattice points. The direction \mathbf{d} of a hexagonal lattice point in the real space may also be represented by the Miller-bravais notation, in which the third component corresponds to an additional third axis $(-\mathbf{a} - \mathbf{b})$, which is symmetrically equivalent to the first and second axes, \mathbf{a} and \mathbf{b} :

$$\mathbf{d} = x\mathbf{a} + y\mathbf{b} + 0(-\mathbf{a} - \mathbf{b}) + z\mathbf{c} = [x \ y \ 0 \ z], \quad (2.17)$$

which is identical to Eq. (2.11). In the conventional Miller-Bravais notation as a four-component index, the sum of the first three components is set to zero:

$$\mathbf{d} = x'\mathbf{a} + y'\mathbf{b} + (-x' - y')(-\mathbf{a} - \mathbf{b}) + z\mathbf{c} = [x' \ y' \ (-x' - y') \ z]. \quad (2.18)$$

For this \mathbf{d} to be identical to \mathbf{d} in Eq. (2.18), $x = 2x' + y'$ and $y = 2y' + x'$, and inversely $x' = (2x - y)/3$, $y' = (2y - x)/3$, and $-x' - y' = (-x - y)/3$. This notation is useful to find the real space vector \mathbf{d} parallel to the reciprocal space vector $\mathbf{G} = (x' \ y' \ (-x' - y') \ 0)$ in the $a^* - b^*$ plane: simply given by $\mathbf{d} = [x' \ y' \ (-x' - y') \ 0]$.

Scattering factor and its extinction The atomic form factor $f(\mathbf{Q})$, representing an elastic scattering by an atom, is a function of the scattering vector $\mathbf{Q} = \mathbf{k}_i - \mathbf{k}_f$ of the incident (\mathbf{k}_i) and scattered (\mathbf{k}_f) wavevectors, and is given by

$$\begin{aligned} f(\mathbf{Q}) &= \int \rho(\mathbf{r}) \exp(2i\pi\mathbf{Q} \cdot \mathbf{r}) d^3\mathbf{r}, \\ &= 2\pi \int_{-1}^{+1} \int_0^\infty r^2 \rho(r) \exp(2i\pi Qr \cos \theta) dr \, d(\cos \theta), \\ &= \int_0^\infty 4\pi r^2 \rho(r) \frac{\sin(2\pi Qr)}{2\pi Qr} dr, \end{aligned} \quad (2.19)$$

in which the last equality is valid for an electron density distribution $\rho(\mathbf{r})$ of the given atom if it is spherical $\rho(r)$. From this definition, f is real for any \mathbf{Q} . However, in reality, it can be complex when there is inelastic scattering, or absorption by the atom. The structure factor F composed of the atomic form factors of all atoms in a unit cell is

$$F(\mathbf{Q}) = \sum_j f_j(\mathbf{Q}) e^{i\mathbf{Q} \cdot \mathbf{r}_j}, \quad (2.20)$$

where j represents the atom species at a specific site \mathbf{r}_j . One can note that because f is real, $F(-\mathbf{Q})$ is the complex conjugate of $F(\mathbf{Q})$. The x-ray diffraction intensity

has the inversion symmetry as $|F(-\mathbf{Q})|^2 = |F(\mathbf{Q})|^2$ since it is proportional to the absolute square $|F|^2$ in the kinematic approximation. There is also an extinction rule: while in general $F(\mathbf{Q})$ has a finite value if and only if \mathbf{Q} matches a reciprocal lattice vector \mathbf{G} , it may vanish at particular reciprocal lattice points \mathbf{G} , depending on the atomic positions in the given unit cell, if the given unit cell is not primitive or contains many atoms of the same element.

The scattering factor S of an entire sample of single crystal contains the contribution of the structure scattering factors from all the unit cells:

$$\begin{aligned} S(\mathbf{Q}) &= \sum_{\mathbf{R}} F(\mathbf{Q}) e^{2i\pi\mathbf{Q}\cdot\mathbf{R}} \\ &= F(\mathbf{Q}) \sum_{X,Y,Z} e^{2i\pi(hX+kY+lZ)}, \end{aligned} \quad (2.21)$$

where $\mathbf{Q} = h\mathbf{a}^* + k\mathbf{b}^* + l\mathbf{c}^*$. The absolute value of the last summation term for a large number N of the lattice points (a large enough crystal $V = NV_{\text{real}}$) is

$$\left| \sum_{X,Y,Z} e^{2i\pi(hX+kY+lZ)} \right| = \begin{cases} N & (h, k, \text{ and } l \text{ are integers.}) \\ 0 & (h, k, \text{ or } l \text{ is not an integer.}) \end{cases} \quad (2.22)$$

Thus S has a finite value only if the scattering vector matches a reciprocal lattice point $\mathbf{Q} = \mathbf{G} = (h \ k \ l)$, where h , k , and l are integers. Indeed, for $0 \leq X < N_1$, $0 \leq Y < N_2$, and $0 \leq Z < N_3$ with $N = N_1N_2N_3$,

$$\begin{aligned}
\left| \sum_{X,Y,Z} e^{2i\pi(hX+kY+lZ)} \right| &= \left| \sum_{X=0}^{N_1-1} e^{2i\pi hX} \sum_{Y=0}^{N_2-1} e^{2i\pi kY} \sum_{Z=0}^{N_3-1} e^{2i\pi lZ} \right| \\
&= \left| \frac{e^{2i\pi h N_1} - 1}{e^{2i\pi h} - 1} \frac{e^{2i\pi k N_2} - 1}{e^{2i\pi k} - 1} \frac{e^{2i\pi l N_3} - 1}{e^{2i\pi l} - 1} \right| \quad (2.23) \\
&= \left| \frac{\sin(i\pi h N_1)}{\sin(i\pi h)} \frac{\sin(i\pi k N_2)}{\sin(i\pi k)} \frac{\sin(i\pi l N_3)}{\sin(i\pi l)} \right| \\
&\simeq N_1 N_2 N_3.
\end{aligned}$$

Here, the approximation is valid if N_1 , N_2 , and N_3 are large. Otherwise, i.e., if a crystal volume is not so large, the sinc function is finite at certain fractional values of h , k , l .

When the unit cell contains more than one atom of the same element, $F(\mathbf{Q})$ and hence $S(\mathbf{Q})$ may vanish even if \mathbf{Q} is equal to the reciprocal lattice vector \mathbf{G} . This condition on $\mathbf{G} = (h \ k \ l)$ is called an extinction rule, which depends on the relative atomic positions in a given unit cell. The following paragraph consists in the determination of the extinction conditions for Mn_5Ge_3 and Ge.

The structure of the Ge crystal Germanium has a *diamond* lattice with $a = 5.664 \text{ \AA}$ (at room temperature), and its structure factor extinction rule is obtained easily as follows. The atomic positions in a conventional cubic unit cell are given by

$$\{(0, 0, 0), (0, 1/2, 1/2), (1/2, 0, 1/2), (1/2, 1/2, 0)\} \otimes \{(0, 0, 0), (1/4, 1/4, 1/4)\} \quad (2.24)$$

in units of $(\mathbf{a}, \mathbf{b}, \mathbf{c})$. Therefore,

$$F(\mathbf{G})/f_{\text{Ge}}(G) = (1 + e^{i\pi(k+l)} + e^{i\pi(l+h)} + e^{i\pi(h+k)}) \times (1 + e^{i\pi(h+k+l)/2}), \quad (2.25)$$

leading to

$$|F(\mathbf{G})/f_{\text{Ge}}(G)| = \begin{cases} 8 & \text{if } h, k, \text{ and } l \text{ are all even with } (h + k + l) \bmod 4 = 0, \\ 4\sqrt{2} & \text{if } h, k \text{ and } l \text{ are all odd,} \\ 0 & \text{otherwise.} \end{cases} \quad (2.26)$$

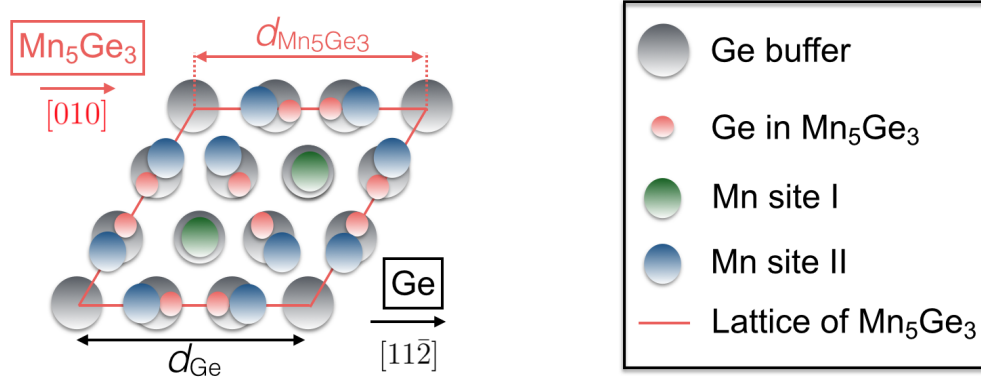


Figure 2-12: Top-view of the unit cell of the hexagonal Mn_5Ge_3 crystal. The green large-sized balls correspond to Mn_{I} sites, including the masked Mn_{I} sites located at $c/2$. The unit cell includes ten Ge atoms, four Mn_{I} atoms and six Mn_{II} atoms.

The structure of Mn_5Ge_3 The Mn_5Ge_3 crystal has a hexagonal D_{6h}^3 , i.e., $P6_3/mcm$ space-group symmetry [31]. Its crystal structure is called $D8_8$ and has the following lattice parameters (length and angles) [32]:

$$\begin{aligned} a = b = 7.112 \text{ \AA}, \quad c = 5.057 \text{ \AA}, \\ \alpha = \beta = 90^\circ, \quad \gamma = 120^\circ. \end{aligned} \quad (2.27)$$

The unit cell, represented in Fig. 2-12, contains six Ge and ten Mn atoms [31] at the following sites with two parameters $v = 0.61$ and $u = 0.25$ [29]:

$$\text{Ge} = (-v, 0, 0), (0, -v, 0), (v, 0, 1/2), (0, v, 1/2), (v, v, 0), (-v, -v, 1/2) \quad (2.28)$$

$$\text{Mn} = \begin{cases} \text{Mn}_{\text{I}} : (\frac{-1}{3}, \frac{-1}{3}, \frac{1}{4}), (\frac{-1}{3}, \frac{1}{3}, \frac{-1}{4}), (\frac{1}{3}, \frac{-1}{3}, \frac{1}{4}), (\frac{1}{3}, \frac{1}{3}, \frac{-1}{4}); \\ \text{Mn}_{\text{II}} : (-u, 0, 0), (0, -u, 0), (u, 0, \frac{1}{2}), (0, u, \frac{1}{2}), (u, u, 0), (-u, -u, \frac{1}{2}). \end{cases} \quad (2.29)$$

Here, the Mn sites are classified into two groups Mn_{I} and Mn_{II} , in each of which all the sites are symmetrically equivalent (transferred by symmetry operations).

For the Mn_5Ge_3 crystal structure, $F(\mathbf{G})$ at $\mathbf{G} = (h \ k \ l)$ is calculated as follows:

$$\begin{aligned} F(\mathbf{G}) &= F_{\text{Ge}}(\mathbf{G}) + F_{\text{Mn}_{\text{I}}}(\mathbf{G}) + F_{\text{Mn}_{\text{II}}}(\mathbf{G}) \\ &= \sum_{j=1}^6 f_{\text{Ge}}(G) e^{i\mathbf{G}\cdot\mathbf{r}_j} + \sum_{j=7}^{10} f_{\text{Mn}}(G) e^{i\mathbf{G}\cdot\mathbf{r}_j} + \sum_{j=11}^{16} f_{\text{Mn}}(G) e^{i\mathbf{G}\cdot\mathbf{r}_j} \\ &= f_{\text{Ge}}(G) \{ e^{-2\pi i v h} + e^{-2\pi i v k} + e^{2\pi i v h} e^{\pi i l} + e^{2\pi i v k} e^{\pi i l} + e^{2\pi i v(h+k)} + e^{-2\pi i v(h+k)} e^{\pi i l} \} \\ &\quad + f_{\text{Mn}}(G) \{ e^{-2\pi i u h} + e^{-2\pi i u k} + e^{2\pi i u h} e^{\pi i l} + e^{2\pi i u k} e^{\pi i l} + e^{2\pi i u(h+k)} + e^{-2\pi i u(h+k)} e^{\pi i l} \} \\ &\quad + f_{\text{Mn}}(G) \left\{ e^{\frac{2\pi i(-h+k)}{3}} e^{\frac{\pi i l}{2}} + e^{\frac{2\pi i(-h+k)}{3}} e^{-\frac{\pi i l}{2}} + e^{\frac{2\pi i(h-k)}{3}} e^{\frac{\pi i l}{2}} + e^{\frac{2\pi i(h-k)}{3}} e^{-\frac{\pi i l}{2}} \right\} \\ &= 2f_{\text{Ge}}(G) e^{\frac{i\pi l}{2}} \left\{ \cos(2\pi v h + \frac{\pi l}{2}) + \cos(2\pi v k + \frac{\pi l}{2}) + \cos[2\pi v(h+k) - \frac{\pi l}{2}] \right\} \\ &\quad + 2f_{\text{Mn}}(G) e^{\frac{i\pi l}{2}} \left\{ \cos(2\pi u h + \frac{\pi l}{2}) + \cos(2\pi u k + \frac{\pi l}{2}) + \cos[2\pi u(h+k) - \frac{\pi l}{2}] \right\} \\ &\quad + 4f_{\text{Mn}}(G) \cos\left[\frac{2\pi(h-k)}{3}\right] \cos\left(\frac{\pi l}{2}\right). \end{aligned} \quad (2.30)$$

Thus, $F_{\text{Mn}_{\text{I}}}$, corresponding to the contribution of Mn_{I} , is described by a single term:

$$\begin{aligned} F_{\text{Mn}_{\text{I}}}(\mathbf{G})/f_{\text{Mn}}(G) &= 4 \cos(2\pi(h-k)/3) \cos(\pi l/2) \\ &= \begin{cases} 0 & \text{if } l \text{ is odd,} \\ \pm 4 & \text{if } l \bmod 4 = 1 \mp 1 \text{ and } (h-k) \bmod 3 = 0, \\ \mp 2 & \text{if } l \bmod 4 = 1 \mp 1 \text{ and } (h-k) \bmod 3 = 1, \\ \pm 2 & \text{if } l \bmod 4 = 1 \mp 1 \text{ and } (h-k) \bmod 3 = 2. \end{cases} \end{aligned} \quad (2.31)$$

As a result, this term vanishes if and only if l is an odd number irrespective of the values of h and k , because of $\cos(\pi l/2) = 0$. F_{MnI} has a nonvanishing value $4f_{\text{Mn}}$ or $2f_{\text{Mn}}$ in its magnitude for an even number of l , as summarized in Table 2.1.

Since l appears only as the definite form $\pi l/2$ in the entire expression of $F(\mathbf{G})$, it can be classified by the remainder of l divided by 4 ($l \bmod 4 = 0, 1, 2$, or 3). If $l \bmod 4 = 0$,

$$\begin{aligned} F(\mathbf{G}) = F(h \ k \ 0) &= 2f_{\text{Ge}}(G)\{\cos(2\pi vh) + \cos(2\pi vk) + \cos[2\pi v(h+k)]\} \\ &+ 2f_{\text{Mn}}(G)\{\cos(2\pi uh) + \cos(2\pi uk) + \cos[2\pi u(h+k)]\} \\ &+ 4f_{\text{Mn}}(G) \cos[2\pi(h-k)/3]. \end{aligned} \quad (2.32)$$

For any other even values of l , i.e., $l \bmod 4 = 2$,

$$\begin{aligned} F(\mathbf{G}) = F(h \ k \ 2) &= 2f_{\text{Ge}}(G)\{\cos(2\pi vh) + \cos(2\pi vk) + \cos[2\pi v(h+k)]\} \\ &+ 2f_{\text{Mn}}(G)\{\cos(2\pi uh) + \cos(2\pi uk) + \cos[2\pi u(h+k)]\} \\ &- 4f_{\text{Mn}}(G) \cos[2\pi(h-k)/3], \end{aligned} \quad (2.33)$$

which differs from $F(h \ k \ 4)$ only in the sign of the last term F_{MnI} . For any other values of l , i.e., any odd numbers irrespective of $l \bmod 4 = 1$ or 3 ,

$$\begin{aligned} F(\mathbf{G}) = F(h \ k \ 1) &= -2if_{\text{Ge}}(G)\{\sin(2\pi vh) + \sin(2\pi vk) - \sin[2\pi v(h+k)]\} \\ &- 2if_{\text{Mn}}(G)\{\sin(2\pi uh) + \sin(2\pi uk) - \sin[2\pi u(h+k)]\}. \end{aligned} \quad (2.34)$$

Since the parameter u for the six Mn_{II} positions is a rational number within the experimental accuracy, the Mn_{II} part of $F(\mathbf{G})$, F_{MnII} , vanishes for many sets of integers $(h \ k \ l)$, while since $v = 0.61$ for the ten positions of Ge is not a rational (with small integers in the denominator and the numerator) the Ge part of $F(\mathbf{G})$ should not van-

ish except for some special cases of $(h \ k \ l)$. These extinction conditions are derived below.

Assuming u is exactly a rational number of $1/4$, the M_{nII} part of $F(\mathbf{G})$ can be written as

$$\frac{F_{M_{nII}}(h \ k \ l)}{f_{Mn}(h \ k \ l)} = 2e^{i\pi l/2} \{ \cos[\pi(h+l)/2] + \cos[\pi(k+l)/2] + \cos[\pi(h+k-l)/2] \}. \quad (2.35)$$

Since the reduced angle values in the cosine terms can be only 0 , $\pm\pi/2$, or π , each cosine term can have values of only $+1$, 0 , or -1 , respectively. Therefore, $F_{M_{nII}}(h \ k \ l)$ vanishes, either (a) if every cosine term is equal to 0 or (b) if all these values ($+1$, 0 , -1) appear simultaneously in these cosine terms. Case (a) is equivalent to that all of $(h+l)$, $(k+l)$, and $h+k-l$ are odd numbers, which means that both h and k are even while l is odd. Case (b) occurs if $(h+l)$, $(k+l)$, and $h+k+l$ have different remainders $(0,1,2)$ or $(0,3,2)$, in no particular order, when divided by 4 . Considering the parities of h , k , and l , the following cases are necessary conditions for $F(\mathbf{G})$ to vanish: (b-1) all odd, or all odd except for either (b-2) h or (b-3) k , as listed in Table 2.1.

In case (b-1), $h+l$ and $k+l$ are even and $h+k-l$ is odd. Hence, the even $h+l$ and $k+l$ need to have different remainders 0 and 2 , when divided by 4 , and thus the odd h and k need to have different remainders 1 and 3 (equivalent to -1). This extinction condition on $(h \ k \ l)$ for this case (b-1) is listed in the row (b-1) in Table 2.2. A shortest example is $\mathbf{G} = (1 \ \bar{1} \ 0 \ \pm 1)$. The other sets of all-odd $(h \ k \ l)$ such as $(\pm 1 \ \pm 1 \ \pm 1)$ not satisfying the extinction condition give $|F_{M_{nII}}/f_{Mn}| = 4$ according to Eq. (2.35). Cases (b-2) and (b-3) are related to case (b-1) by the threefold rotations. In case (b-2), $h+l$ is odd, and hence the even $k+l$ and $h+k-l$ need to have different remainders 0 and 2 , when divided by 4 . Hence, the difference $(k+l) - (h+k-l) = 2l-h$ is $(2l-h) \bmod 4$.

$4 = 2$. Since l is assumed odd, i.e., $2l \bmod 4 = 2$, h needs to have no remainder, i.e., $h \bmod 4 = 0$. The case (b-3) is equivalent to case (b-2) as obvious by swapping h and k .

Table 2.1: Necessary conditions for the extinction of $F_{\text{MnII}}(\mathbf{G})$ and $F_{\text{MnI}}(\mathbf{G})$ at $\mathbf{G} = (h \ k(j) \ l)$. By displaying also the third component j , it is suggested that cases (b-1), (b-2), and (b-3) are symmetrically related to each other but distinct from case (a).

Site in Mn_5Ge_3 (Case)	h	k	(j)	l
MnI	\forall	\forall	(\forall)	odd
MnII (a)	even	even	(even)	odd
MnII (b-1)	odd	odd	(even)	odd
MnII (b-2)	even	odd	(odd)	odd
MnII (b-3)	odd	even	(odd)	odd

Table 2.2: The full extinction conditions of F_{MnII} in the Miller-Bravais notation ($j = -h - k$). (a) ω is an arbitrary odd number, and ϵ_m ($m = 1, 2$) are arbitrary even numbers. (b) ϵ is an even number, and ω_1 and ω'_1 are odd numbers, satisfying $\omega_1 + \omega'_1 + 2\epsilon = 0$, and hence $(\omega_1 + \omega'_1) \bmod 4 = 0$. One can note that for the three cases (b-1), (b-2), and (b-3) with three common parameters $(\omega_1, \omega'_1, \epsilon)$, \mathbf{G} vectors are symmetrically equivalent and related by C_3 rotations about the \mathbf{c}^* axis. The last column shows an example of \mathbf{G} vectors selected as not satisfying the F_{Ge} shown below.

Case	h	k	(j)	l	example
(a)	ϵ_1	ϵ_2	$(-\epsilon_1 - \epsilon_2)$	ω	$(2 \ 2 \ (\bar{4}) \ 1)$
(b-1)	ω_1	ω'_1	(2ϵ)	ω	$(1 \ 3 \ (\bar{4}) \ 1)$
(b-2)	2ϵ	ω_1	(ω'_1)	ω	$(4 \ \bar{3} \ (\bar{1}) \ 3)$
(b-3)	ω'_1	2ϵ	(ω_1)	ω	$(3 \ \bar{8} \ (5) \ \bar{1})$

In all the cases (a), (b-1), (b-2), and (b-3) for which $F_{\text{MnI}}(\mathbf{G})$ vanishes, $F_{\text{MnII}}(\mathbf{G})$ also vanishes, and hence $F_{\text{Mn}}(\mathbf{G}) = F_{\text{MnI}}(\mathbf{G}) + F_{\text{MnII}}(\mathbf{G})$ vanishes.

On the other hand, in cases (b-1), (b-2), and (b-3) in Table 2.1 excluded from the relevant cases in Table 2.2, F_{Mn} does not vanish generally. Below are notable examples,

$$F_{\text{Mn}}(1 \ 1 \ \bar{2} \ \pm 1) / f_{\text{Mn}}(G) = -4i \text{ for case (b-1);} \quad (2.36)$$

$$F_{\text{Mn}}(\bar{2} 1 1 \pm 1)/f_{\text{Mn}}(G) = -4i \text{ for case (b-2);} \quad (2.37)$$

$$F_{\text{Mn}}(1 \bar{2} 1 \pm 1)/f_{\text{Mn}}(G) = -4i \text{ for case (b-3).} \quad (2.38)$$

As derived above, F_{Mn} cannot vanish if l is an even number. Neither the Ge part of F_{Ge} can vanish if l is an even number, since irrespective of $l \bmod 4 = 0$ or 2

$$F_{\text{Ge}}(\mathbf{G})/f_{\text{G}} = -2\{\cos(2\pi vh) + \cos(2\pi vk) + \cos[2\pi v(h+k)]\}, \quad (2.39)$$

with irrational $v = 0.61$. Then, one considers the case of odd l below.

If l is odd including all cases in Table 2.1, the Ge part is given generally by

$$F_{\text{Ge}}(\mathbf{G})/f_{\text{G}} = -2i\{\sin(2\pi vh) + \sin(2\pi vk) - \sin[2\pi v(h+k)]\}. \quad (2.40)$$

This can vanish only if two of the three terms in the right hand side of equation have a same amplitude and the other one vanishes by itself because of irrational v . Therefore, the extinction condition is equivalent to “ $h = 0$, $k = 0$, or $h + k = 0$ ”. Thus,

$$F_{\text{Ge}}(h 0 l) = F_{\text{Ge}}(0 \bar{h} l) = F_{\text{Ge}}(\bar{h} h l) = 0 \quad (2.41)$$

for an arbitrary integer h and an odd l . These three reciprocal spots with common h and l are symmetrically equivalent as they are transferred by C_3 rotations about the \mathbf{c}^* axis. Otherwise, if all of h , k , and $h + k$ have nonzero values, F_{Ge} does not exactly vanish due to irrational v . These extinction conditions of $F_{\text{Ge}}(\mathbf{G})$ are listed in Table 2.3.

Table 2.3: The extinction conditions for $F_{G_e}(h k (j) l)$. ν is an arbitrary integer ($\bar{\nu} = -\nu$), and ω is an independent odd number. As in the cases (b-1), (b-2), and (b-3), the three cases (c-1), (c-2), and (c-3) with common ν and the same ω are related by C_3 rotations about the \mathbf{c}^* axis. The last column shows inequivalent examples.

Case	h	k	(j)	l	\mathbf{G}
(c-1)	ν	0	$(\bar{\nu})$	ω	$(0\ 0\ (0)\ 1)$
(c-2)	0	$\bar{\nu}$	(ν)	ω	$(0\ 1\ (\bar{1})\ 3)$
(c-3)	$\bar{\nu}$	ν	(0)	ω	$(2\ \bar{2}\ (0)\ 1)$

Overall extinction conditions In summary, $F(\mathbf{G})$ vanishes when all the extinction conditions for F_{M_n} (see Tables 2.1 and 2.2) and F_{G_e} (see Table 2.3) are met simultaneously. Indeed, F vanishes in the six cases listed in Table 2.4, and the whole condition can be simply represented by symmetrically equivalent reciprocal lattice points

$$\{\nu\ \bar{\nu}\ 0\ \omega\}. \quad (2.42)$$

This contains $(\nu\ \bar{\nu}\ 0\ \omega)$, $(\bar{\nu}\ 0\ \nu\ \omega)$, and $(0\ \nu\ \bar{\nu}\ \omega)$ with an arbitrary integer ν and an arbitrary odd number ω . Thus, in diffraction spectra a half part (odd l) of the reciprocal lattice points \mathbf{G} located in three particular planes vanishes. All these three planes contain the \mathbf{c}^* axis and either one of the other “three” reciprocal lattice basis vectors and can be denoted by its normal orientation with the real lattice basis vectors as $\mathbf{d} = \langle 2\ \bar{1}\ \bar{1} \rangle$, each of which is parallel to $\mathbf{G} = \{2\ \bar{1}\ \bar{1}\}$, respectively.

Table 2.4: The extinction conditions for the total $F(\mathbf{G})$. ω_1 and ϵ_1 are arbitrary odd and even integers, respectively, and hence an arbitrary integer as a whole. ω_2 is an independent odd number. The last column shows representative examples. One can note that these conditions reduce to Eq. (2.42) without loss of generality.

Case	h	k	(j)	l	\mathbf{G}
(b-3) and (c-1)	ω_1	0	$(\overline{\omega_1})$	ω_2	$(3\ 0\ (\overline{3})\ 1)$
(b-3) and (a)	ϵ_1	0	$(\overline{\epsilon_1})$	ω_2	$(2\ 0\ (\overline{2})\ 1)$
(b-2) and (c-2)	0	$\overline{\omega_1}$	(ω_1)	ω_2	$(0\ \overline{3}\ (3)\ 1)$
(b-2) and (a)	0	$\overline{\epsilon_1}$	(ϵ_1)	ω_2	$(0\ \overline{2}\ (2)\ 1)$
(b-1) and (c-3)	$\overline{\omega_1}$	ω_1	(0)	ω_2	$(\overline{3}\ 3\ (0)\ 1)$
(b-1) and (a)	$\overline{\epsilon_1}$	ϵ_1	(0)	ω_2	$(\overline{2}\ 2\ (0)\ 1)$

Experimental restrictions - Wavelength

As mentioned previously, the x-ray scattering vector \mathbf{Q} is defined as $\mathbf{k}_f = \mathbf{k}_i + \mathbf{Q}$, in which the \mathbf{k}_i and \mathbf{k}_f are the incident and scattered wavevectors of the x-ray, respectively. The necessary condition for x-ray diffraction is that \mathbf{Q} matches a reciprocal lattice vector \mathbf{G} :

$$\mathbf{Q} = \mathbf{k}_f - \mathbf{k}_i = \mathbf{G}, \quad (2.43)$$

while the diffraction intensity may vanish for specific \mathbf{G} due to the extinction rules, described in the previous paragraph. This diffraction condition can be visually described in the Ewald construction. The starting point of the three involved vectors \mathbf{G} , \mathbf{k}_f , and $-\mathbf{k}_i$ are set at the origin \mathbf{O} . Any elastic scattering with a constant wavelength λ is illustrated by \mathbf{k}_f and $-\mathbf{k}_i$ whose ending points are located on the Ewald sphere which center is at \mathbf{O} and which radius is equal to $K = 1/\lambda$. The scattering angle $2\theta = [0, \pi]$ is defined by $\cos(2\theta) = \mathbf{k}_f \cdot \mathbf{k}_i / K^2$.

Thus, for a constant wavelength, Eq. (2.43) gives

$$\begin{aligned}
 \mathbf{G}^2 &= G^2 = K^2 + K^2 - 2\mathbf{k}_f \cdot \mathbf{k}_i = 2K^2(1 - \cos(2\theta)) = (2K \sin \theta)^2, \\
 \mathbf{k}_f^2 &= K^2 = G^2 + K^2 + 2\mathbf{G} \cdot \mathbf{k}_i, \\
 \mathbf{k}_i^2 &= K^2 = G^2 + K^2 - 2\mathbf{G} \cdot \mathbf{k}_f.
 \end{aligned} \tag{2.44}$$

Therefore,

$$\begin{aligned}
 \frac{G}{2K} &= \sqrt{\frac{1 - \hat{\mathbf{k}}_f \cdot \hat{\mathbf{k}}_i}{2}} = \sin \theta, \\
 &= \hat{\mathbf{G}} \cdot (-\hat{\mathbf{k}}_i), \\
 &= +\hat{\mathbf{G}} \cdot \hat{\mathbf{k}}_f.
 \end{aligned} \tag{2.45}$$

Eq. (2.45) is well-known as the Bragg condition. In this case, it is expressed by the reciprocal lattice length G and the wavenumber K rather than the lattice plane distance d and the wavelength λ . This tells that θ is larger for larger G and gives an upper limit on G :

$$G \leq 2K, \tag{2.46}$$

indicating that \mathbf{G} needs to be within the circle of a radius $2K$ centered at \mathbf{O} . On the other hand, Eq. (2.45) also indicates that the angles between \mathbf{G} and $-\mathbf{k}_i$ and between \mathbf{G} and \mathbf{k}_f are both equal to $\pi/2 - \theta$, which is smaller than $\pi/2$ and decreases with decreasing G , represented as a whole by

$$\mathbf{G} \cdot \mathbf{K} \geq 0, \tag{2.47}$$

where $\mathbf{K} = -\mathbf{k}_i$ and \mathbf{k}_f . In the inequation, equality is valid only for $G = 0$. When \mathbf{G} is given, \mathbf{k}_f and $-\mathbf{k}_i$ are along the surface of a cone whose apex angle is given by the scattering angle 2θ and whose intersection with the Ewald sphere is a circle of a radius $\sqrt{K^2 - (G/2)^2} = K \cos \theta$ at a distance of $G/2$. From Eq. (2.43), one can see a limitation is imposed on diffraction due to the x-ray wavelength ($\lambda = 1/K$) and scattering geometry (sample geometry with respect to x-ray incidence and detector). Additionally, from the diffraction condition, one obtains

$$\mathbf{k}_f - \mathbf{G}/2 = -(-\mathbf{k}_i - \mathbf{G}/2), \quad (2.48)$$

$$(\mathbf{k}_f - \mathbf{G}/2) \cdot \mathbf{G} = -(-\mathbf{k}_i - \mathbf{G}/2) \cdot \mathbf{G} = 0. \quad (2.49)$$

According to Eq. (2.45) in the Ewald construction, $\mathbf{K} = -\mathbf{k}_i$ and \mathbf{k}_f are decomposed to the parallel and perpendicular components with respect to \mathbf{G} as

$$\begin{aligned} \mathbf{K} - \frac{1}{2}\mathbf{G} &= -\hat{\mathbf{G}} \times (\hat{\mathbf{G}} \times \mathbf{K}) \\ &= \sqrt{K^2 - (G/2)^2} \frac{(\mathbf{G} \times \mathbf{K}) \times \mathbf{G}}{G^2 K \cos \theta}, \end{aligned} \quad (2.50)$$

which have the same magnitude with signs for $-\mathbf{k}_i$ and \mathbf{k}_f .

For a wavelength of $\lambda = 0.1542$ nm, Eq. (2.45) gives a limitation on G as $G < 2/(0.1542 \text{ nm}) = 12.97 \text{ nm}^{-1}$. For Ge, $G/a_{\text{Ge}}^* = 12.97 \text{ nm}^{-1} \times 0.5664 \text{ nm} = 7.34$, and hence $h^2 + k^2 + l^2 \leq 53$. For Mn_5Ge_3 , $G/a_{\text{Mn}_5\text{Ge}_3}^* = 12.97 \text{ nm}^{-1} \times 0.7112 \text{ nm} = 9.22$, and hence $h^2 + k^2 + hk + l^2 (c_{\text{Mn}_5\text{Ge}_3}^*/a_{\text{Mn}_5\text{Ge}_3}^*)^2 = h^2 + k^2 + hk + 1.406l^2 \leq 86$.

Experimental restrictions - Reflection geometry

Hereafter, one considers a flat sample and the diffraction through its “front” surface, whose outward normal direction is given by a unit vector \mathbf{n} . In this geometry, the incident and scattered waves have negative and positive cosines, respectively, with \mathbf{n} , thus making angles with the outward surface normal larger and smaller than $\pi/2$, respectively:

$$\mathbf{k}_i \cdot \mathbf{n} < 0 \quad \text{and} \quad \mathbf{k}_f \cdot \mathbf{n} > 0, \quad (2.51)$$

and

$$\mathbf{K} \cdot \mathbf{n} > 0 \quad (2.52)$$

as a whole. Based on this condition, derive the measurable condition on \mathbf{G} . The tilt of \mathbf{G} from the surface normal \mathbf{n} by an angle of τ is represented by

$$\mathbf{n} \cdot \mathbf{G}/G = \cos \tau. \quad (2.53)$$

The geometric limitation of Eq. (2.52) provides a necessary condition:

$$\mathbf{n} \cdot \mathbf{G}/G = \mathbf{n} \cdot (\mathbf{k}_f - \mathbf{k}_i)/G > 0, \quad (2.54)$$

$$0 \leq \tau < \pi/2. \quad (2.55)$$

Thus it is necessary for \mathbf{G} to be pointed outward from the surface.

Moreover, reciprocal vectors can be represented by the Cartesian coordinates where z axis is parallel to \mathbf{n} , x axis is parallel to $\mathbf{G} - (\mathbf{n} \cdot \mathbf{G})\mathbf{n} = (\mathbf{n} \times \mathbf{G}) \times \mathbf{n}$,

and hence y axis is parallel to $\mathbf{n} \times \mathbf{G}$ (see Fig. 2-13). Then,

$$\mathbf{n} = \hat{\mathbf{z}}, \quad (2.56a)$$

$$\mathbf{G} = G \cos \tau \hat{\mathbf{z}} + G \sin \tau \hat{\mathbf{x}} = 2K \sin \theta (\cos \tau \hat{\mathbf{z}} + \sin \tau \hat{\mathbf{x}}), \quad (2.56b)$$

$$\begin{aligned} \mathbf{K} &= \frac{1}{2} \mathbf{G} + K \cos \theta [(-\sin \tau \hat{\mathbf{z}} + \cos \tau \hat{\mathbf{x}}) \cos \phi + \hat{\mathbf{y}} \sin \phi] \\ &= K [(\sin \theta \cos \tau - \cos \theta \sin \tau \cos \phi) \hat{\mathbf{z}} + (\sin \theta \sin \tau + \cos \theta \cos \tau \cos \phi) \hat{\mathbf{x}} + \cos \theta \sin \phi \hat{\mathbf{y}}]. \end{aligned} \quad (2.56c)$$

Here, for $\mathbf{K} = -\mathbf{k}_i$ and \mathbf{k}_f , ϕ shall be denoted as ϕ_i and ϕ_f , respectively. According to Eq. (2.43), i.e., $\mathbf{k}_f + (-\mathbf{k}_i) = \mathbf{G}$, Eqs. (2.56b) and (2.56c) give restriction on ϕ_i and ϕ_f : $\cos \phi_i + \cos \phi_f = 0$ and $\sin \phi_i + \sin \phi_f = 0$, i.e.,

$$|\phi_i - \phi_f| = \pi, \quad (2.57)$$

except for the case of $\theta = \pi/2$, which corresponds to $\mathbf{k}_f = -\mathbf{k}_i = \mathbf{G}/2$. Therefore, Eq. (2.52) is equivalent to

$$\sin \theta \cos \tau > \pm \cos \theta \sin \tau \cos \phi \quad (2.58)$$

for both of $\phi = \phi_i$ and ϕ_f . Together with the necessary condition given in Eq. (2.55),

$$0 \leq |\cos \phi| < \tan \theta / \tan \tau. \quad (2.59)$$

Thus, ϕ can take an arbitrary value in the case of $\theta > \tau$, while ϕ is limited around $\pi/2$ in the case of $\theta \leq \tau$. In another form,

$$0 \leq \tan \tau < \tan \theta / |\cos \phi|. \quad (2.60)$$

The last term can have a value in the range $[\tan \theta, \infty]$. Thus, τ can take an arbitrary value satisfying Eq. (2.55) for $\phi = \pm\pi/2$, while this range is narrowed for other values of ϕ , reaching $\tau < \theta$ for $\phi = 0$, which corresponds to the case for which the scattering plane defined by \mathbf{k}_i and \mathbf{k}_f as well as \mathbf{G} contains also the surface normal \mathbf{n} .

In the case of $\sin \phi_i = \sin \phi_f = 0$,

$$1 < \tan \theta / \tan \tau. \quad (2.61)$$

Thus, τ needs to satisfy $\tau < \theta$. In the opposite case, that satisfies $\cos \phi_i = \cos \phi_f = 0$, i.e. $\mathbf{K} - \mathbf{G}/2 \parallel \hat{\mathbf{y}}$, and $0 < \tan \theta / \tan \tau$. Thus, in this case, there is no restriction on τ as far as Eq. (2.55).

By using

$$\tan \theta = \frac{G}{\sqrt{(2K)^2 - G^2}} \quad (2.62)$$

and

$$\tan \tau = \frac{G_t}{G_n}, \quad (2.63)$$

where G_n and G_t are the surface normal and tangential components of \mathbf{G} , respectively.

With $0 \leq \tau < \pi/2$, Eq. (2.59) can be expressed as

$$\cos^2 \phi < \frac{G_n^2 + G_t^2}{(2K)^2 - G_n^2 - G_t^2} \frac{G_n^2}{G_t^2}. \quad (2.64)$$

This is simplified to a quadratic (in)equation of G_n^2 and G_t^2 as follows:

$$(G_n^2)^2 + \cos^2 \phi (G_t^2)^2 + (1 + \cos^2 \phi) G_n^2 G_t^2 - \cos^2 \phi (2K)^2 G_t^2 > 0. \quad (2.65)$$

For $\sin \phi = 0$,

$$G_n^4 + G_t^4 + 2G_n^2 G_t^2 > (2K)^2 G_t^2. \quad (2.66)$$

Hence,

$$G_n^2 + (G_t - K)^2 > K^2. \quad (2.67)$$

Note that the tangential axis is defined for G_t to be positive. This represents that \mathbf{G} needs to be outside of the upper-half of the semicircle, whose radius is K and the center is at $G_t = K$. The reciprocal domain that satisfies this geometrical condition ($\sin \phi = 0$) and also the Bragg condition determined by the wavelength is illustrated in Fig. 2-14 for specific a orientation in Mn_5Ge_3 on $\text{Ge}(111)$.

For $\cos \phi = 0$,

$$G_n^4 + G_n^2 G_t^2 > 0, \quad (2.68)$$

which is satisfied for any vector \mathbf{G} .

The equation is complicated for $\cos \phi \neq 0$.

$$\begin{aligned} & \left(G_n^2 - 4K^2 \frac{\cos^2 \phi (1 + \cos^2 \phi)}{(1 - \cos^2 \phi)^2} \right)^2 + \cos^2 \phi \left(G_t^2 + 8K^2 \frac{\cos^2 \phi}{(1 - \cos^2 \phi)^2} \right)^2 \\ & + (1 + \cos^2 \phi) \left(G_n^2 - 4K^2 \frac{\cos^2 \phi (1 + \cos^2 \phi)}{(1 - \cos^2 \phi)^2} \right) \left(G_t^2 + 8K^2 \frac{\cos^2 \phi}{(1 - \cos^2 \phi)^2} \right) \quad (2.69) \\ & > (4K^2 \cos^2 \phi)^2 \frac{1 + 5 \cos^2 \phi + 2 \cos^4 \phi}{(1 - \cos^2 \phi)^3}. \end{aligned}$$

By a rotation of coordinates as

$$\begin{pmatrix} x \\ y \end{pmatrix} = \begin{pmatrix} \cos \eta & \sin \eta \\ -\sin \eta & \cos \eta \end{pmatrix} \begin{pmatrix} G_n^2 - 4K^2 \frac{\cos^2 \phi (1 + \cos^2 \phi)}{(1 - \cos^2 \phi)^2} \\ G_t^2 + 8K^2 \frac{\cos^2 \phi}{(1 - \cos^2 \phi)^2} \end{pmatrix} \quad (2.70)$$

with

$$\tan \eta = \frac{1 + \cos^2 \phi}{1 - \cos^2 \phi}, \quad \text{it turns out that} \quad \frac{x^2}{R_+^2} + \frac{y^2}{R_-^2} > 1, \quad (2.71)$$

with

$$R_{\pm}^2 = \frac{2(4K^2 \cos^2 \phi)^2 \frac{1 + 5 \cos^2 \phi + 2 \cos^4 \phi}{1 - \cos^2 \phi}}{1 + \cos^2 \phi + \sqrt{1 + \cos^4 \phi}}. \quad (2.72)$$

Thus, (x, y) is outside of the ellipse of radii R_{\pm} , which are functions of $\cos^2 \phi_i = \cos^2 \phi_f$:

$$\begin{aligned} x &= cR_+ \cos \zeta, \\ y &= cR_- \sin \zeta, \end{aligned} \quad (2.73)$$

with a prefactor $c > 1$ and an arbitrary angle ζ . Hence,

$$\begin{pmatrix} G_n^2 \\ G_t^2 \end{pmatrix} = \frac{4K^2 \cos^2 \phi}{(1 - \cos^2 \phi)^2} \begin{pmatrix} 1 + \cos^2 \phi \\ -2 \end{pmatrix} + c \begin{pmatrix} \cos \eta & \sin \eta \\ -\sin \eta & \cos \eta \end{pmatrix} \begin{pmatrix} R_+ \cos \zeta \\ R_- \sin \zeta \end{pmatrix}. \quad (2.74)$$

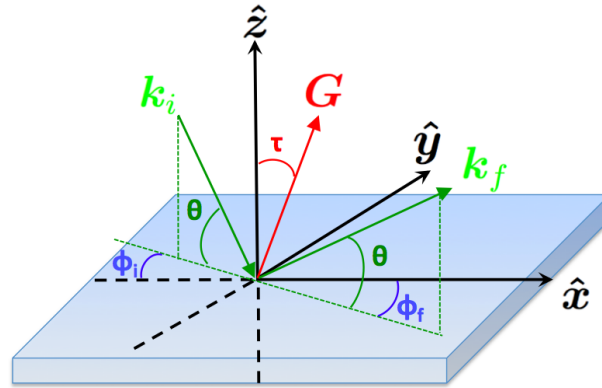


Figure 2-13: Coordinate system used for the reflection geometry. θ is the incidence angle, $\phi = \phi_i$ for $\mathbf{K} = -\mathbf{k}_i$ and $\phi = \phi_f$ for $\mathbf{K} = \mathbf{k}_f$, with $|\phi_i - \phi_f| = \pi$.

Reciprocal domain

x-ray:

$$\lambda = 0.1542 \text{ nm}$$

$$K = 6.486 \text{ nm}^{-1}$$

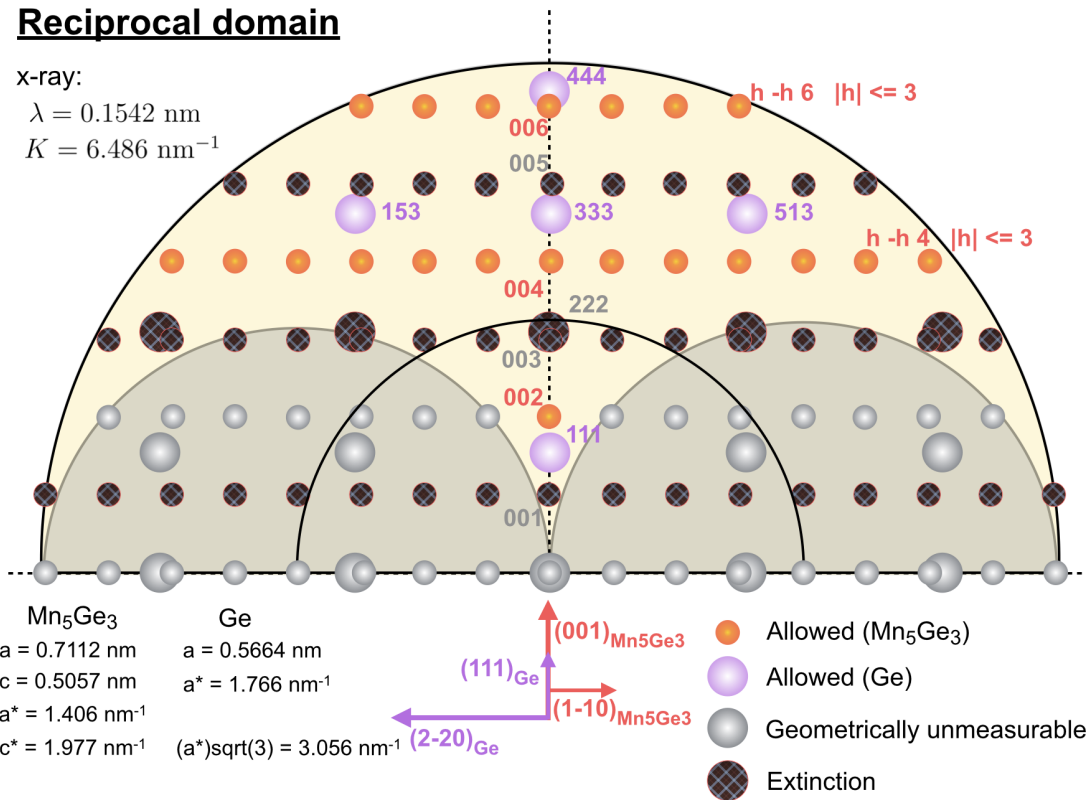


Figure 2-14: Diffraction conditions for the XRD analysis. Red dots and purple dots correspond to the allowed reflections for Mn₅Ge₃ and Ge, respectively. Black striped dots correspond to the extinction conditions calculated in the previous paragraph. The grey dots correspond to XRD limitations mentioned above. The radius of the grey-filled semicircles is K , determined by Eq. (2.67). The radius of the yellow-filled semicircle is $2K$, given by the limitation in x-ray wavelength.

Experimental restrictions - Transmission geometry

Transmissive diffraction can be observed in a different experimental geometry. The observable condition on \mathbf{G} will be obtained similarly to the case of reflective diffraction described above. Now, both the incident and scattered waves, \mathbf{k}_i and \mathbf{k}_f , make an angle with the “front” normal surface \mathbf{n} larger than $\pi/2$:

$$\mathbf{k}_i \cdot \mathbf{n} < 0 \quad \text{and} \quad \mathbf{k}_f \cdot \mathbf{n} < 0, \quad (2.75)$$

Here, the tilt angle τ of \mathbf{G} is defined in Eq. (2.53), but $\mathbf{n} \cdot \mathbf{G}$ can be nonpositive in contrast to the case of reflection. In the case of transmission, Eq. (2.56) is also valid. However, Eq. (2.58) is replaced by

$$\cos \theta \sin \tau \cos \phi_i < \sin \theta \cos \tau < \cos \theta \sin \tau \cos \phi_f, \quad (2.76)$$

indicating possible ranges of values for ϕ_i and ϕ_f as

$$\cos \phi_i < \tan \theta / \tan \tau < \cos \phi_f, \quad (2.77)$$

as τ is defined in $[0, \pi]$ ($\theta \in [0, \pi/2]$). Moreover, due to Eq. (2.57),

$$\cos \phi_f = -\cos \phi_i > \tan \theta / |\tan \tau| \geq 0. \quad (2.78)$$

Another form will be useful to find the range of τ :

$$|\tan \tau| > \tan \theta / \cos \phi_f = \tan \theta / (-\cos \phi_i) \geq 0. \quad (2.79)$$

One can consider a specifically important case, $\sin \phi_i = \sin \phi_f = 0$, in which the four vectors $(\mathbf{G}, \mathbf{n}, \mathbf{k}_i, \mathbf{k}_f)$ are in a single plane. In this case, $\cos \phi_i$ and $\cos \phi_f$ need to be -1 and $+1$, respectively, and thus

$$|\tan \tau| > \tan \theta, \quad \text{and therefore} \quad \theta < \tau < \pi - \theta \quad (2.80)$$

This is the condition opposite to the reflection case for the same values of ϕ_i and ϕ_f as given in Eq. (2.61). On the other hand, $\cos \phi_i = \cos \phi_f = 0$, which allows τ and θ in the entire range for the reflection, is not allowed at all for the transmission. Indeed, in this case, Eq. (2.56c) is simplified into

$$\mathbf{K} = K \sin \theta \cos \tau \hat{\mathbf{z}} + K \sin \theta \sin \tau \hat{\mathbf{x}} + K \cos \theta \sin \phi \hat{\mathbf{y}}, \quad (2.81)$$

indicating $\mathbf{K} \cdot \mathbf{n}$ has the same sign for $-\mathbf{k}_i$ and \mathbf{k}_f violating the transmission geometry restriction in Eq. (2.75).

Keeping in mind that $\tan \theta \geq 0$ and $\cos \phi_f = -\cos \phi_i > 0$, Eq. (2.79) can be expressed with the components of \mathbf{G} .

First, for both $\phi = \phi_f$ and ϕ_i

$$\cos^2 \phi |\tan \tau|^2 > \tan^2 \theta; \quad (2.82)$$

Then,

$$\cos^2 \phi \frac{G_t^2}{G_n^2} > \frac{G^2}{(2K)^2 - G^2}. \quad (2.83)$$

Clearly, this condition for the transmission is the reversed condition of Eq. (2.64) for the reflection. Therefore, the \mathbf{G} domain that does not satisfy the reflection diffraction condition Eq. (2.64) satisfies the transmission diffraction condition Eq. (2.83), while there are additional restrictions due to parameters such wavelength. One can note here that τ is not restricted below $\pi/2$ in the transmission case. As a primary example, the threshold condition for $\sin \phi = 0$ is represented by the circumferences of the two *full* circles centered at $|G_t| = K$, with the same radius K . The purpose of this paragraph is to emphasize the fact that TEM and XRD generally have different regimes of diffraction spots.

Bibliography

- [1] J. P. A. van der Wagt, Ph.D. thesis (1994). [Cited on page(s) 15.]
- [2] K. Wandelt and H. Brune, *Surface and Interface Science: Solid-Solid Interfaces and Thin Films* (Wiley-VCH Verlag GmbH, 2014), Chapter 20. [Cited on page(s) 15.]
- [3] F. C. Frank and J. H. van der Merwe, Proc. R. Soc. London Ser. A **198**, 216 (1949). [Cited on page(s) 15.]
- [4] M. Volmer and A. Weber, Z. Phys. Chem. **119**, 277 (1926). [Cited on page(s) 15.]
- [5] I. N. Stranski and L. Krastanov, Akad. Wiss. Wien, Math.-naturwiss. Kl. IIb **146**, 797 (1938). [Cited on page(s) 16.]
- [6] E. Bauer, I. Z. Kristallogr. **110**, 372 (1958). [Cited on page(s) 16.]
- [7] E. Bauer and J. H. van der Merwe, Phys. Rev. B **33**, 3657 (1986). [Cited on page(s) 17.]
- [8] R. Duffy *et al.*, Appl. Phys. Lett. **90**, 241912 (2007). [Cited on page(s) 19.]
- [9] K. L. Saenger, J. P. de Souza, K. E. Fogel, J. A. Ott, C. Y. Sung, D. K. Sadana, H. Yin, J. Appl. Phys. **101**, 024908 (2007). [Cited on page(s) 19.]
- [10] R. M. B. Agaiby *et al.*, J. App. Phys. **107**, 3319654 (2010). [Cited on page(s) 19.]
- [11] I. Martin-Bragado, Nucl. Instr. Meth. Phys. Res. B **303**, 184 (2013). [Cited on page(s) 19 and 20.]
- [12] W. K. Burton, N. Cabrera, F. C. Frank, Phil. Trans. R. Soc. Lond. A **243**, 866, p. 299-358 (1951). [Cited on page(s) 19.]
- [13] A. A. Chernov, J. Cryst Growth **264**, 499 (2004). [Cited on page(s) 19.]
- [14] L. Pelaz, L. A. Marqués, M. Aboy, P. López and I. Santos, J. Eur. Phys. B **72**, 323 (2009). [Cited on page(s) 19.]
- [15] C. Krzeminski and E. Lampin, Eur. Phys. J. B **88**, 283 (2011). [Cited on page(s) 19.]
- [16] D. C. Paine, N. D. Evans, and N. G. Stoffel, J. Appl. Phys. **70**, 4278 (1991). [Cited on page(s) 20.]
- [17] D. D'Angelo, A. M. Piro, A. Terrasi, M. G. Grimaldi, S. Mirabella, and G. Bongiorno, J. Appl. Phys. **101**, 103508 (2007). [Cited on page(s) 20.]

- [18] S. Hasegawa, *Characterization of Materials* (Wiley, New York, 2012), p. 1925. [Cited on page(s) 21 and 25.]
- [19] A. Ichiyama and P. I. Cohen, *Reflection high energy electron diffraction* (Cambridge University Press, 2004). [Cited on page(s) 25.]
- [20] T. Sakamoto, N. J. Kawai, T. Nakagawa, K. Ohta, and T. Kojima, *Surf. Sci.* **174**, 651 (1986). [Cited on page(s) 21.]
- [21] T. Sakamoto, *Physics, Fabrication, and Applications of Multilayered Structures* (Springer Verlag US, 1988), p.93. [Cited on page(s) 21.]
- [22] G. Lehmppfuhl, A. Ichiyama, and H. Nakahara, *Surf. Sci.* **245**, L159 (1991). [Cited on page(s) 21.]
- [23] B. Müller and V. Zielasek, *Phys. Rev. Lett.* **79**, 4393 (1997). [Cited on page(s) 25.]
- [24] Y. Horio, *Jpn. J. Appl. Phys.* **35**, 3559 (1996). [Cited on page(s) 25.]
- [25] M. T. Dau, V. Le Thanh, L. A. Michez, M. Petit, T. G. Le, O. Abbas, A. Spiesser, and A. Ranguis, *New J. Phys.* **14**, 103020 (2012). [Cited on page(s) 27 and 31.]
- [26] C. Zeng, S. C. Erwin, L. C. Feldman, A. P. Li, R. Jin, Y. Song, J. R. Thompson and H. H. Weiering, *Appl. Phys. Lett.* **83**, 5002 (2003). [Cited on page(s) 6, 29, and 105.]
- [27] T. Nishimura, O. Nakatsuka, S. Akimoto, W. Takeuchi, S. Zaima, *Microelectron. Eng.* **88**, 605 (2011). [Cited on page(s) 29.]
- [28] W. Zhu, H. H. Weiering, E. G. Wang, E. Kaxiras, and Z. Zhang, *Phys. Rev. Lett.* **93**, 126102 (2004). [Cited on page(s) 29.]
- [29] D. H. Day, and R. N. Sinclair, *Acta Crystallogr., Sect B: Struct. Sci.* **26**, 2079 (1970). [Cited on page(s) 29 and 39.]
- [30] A. Spiesser, S. F. Olive-Mendez, M. T. Dau, L. A. Michez, A. Watanabe, V. Le Thanh, A. Glachant, J. Derrien, A. Barski, M. Jamet, *Thin Solid Films* **518**, S113 (2010). [Cited on page(s) 29 and 128.]
- [31] W. Ndiaye *et al.*, *Phys. Rev. B* **87**, 165137 (2013). [Cited on page(s) 39.]
- [32] A. Truong, A. O. Watanabe, T. Sekiguchi, P. A. Mortemousque, T. Sato, K. Ando, and K. M. Itoh, *Phys. Rev. B* **90**, 224415 (2014). [Cited on page(s) 39, 81, and 109.]

Chapter 3

Magnetometry and magnetic properties

In this chapter, the principle of magnetometry using a superconducting quantum interference device is explained. Since the magnetic characterization of Mn_5Ge_3 epitaxial layers is the major part of this work, this chapter also gives a general background on the concepts of magnetic anisotropy and glassy magnetic behaviors, which are important for the next chapters. Section 3.1 describes the superconducting interference device magnetometer, and discusses the possibility of having artifacts from extrinsic contributions. Section 3.2 deals with the origins of magnetic anisotropy and section 3.3 explains the superparamagnetic and spin-glass states.

3.1 Superconducting quantum interference device

Flux quantization According to the Bardeen-Cooper-Schrieffer (BCS) theory [1], the superconducting state exists because the electrons can condensate in bound pairs, called Cooper pairs, which can circulate in a material without being scattered, thus resulting in a resistivity near zero. The Cooper pairs can be destroyed by thermal energy above a critical temperature, by a high current density or by a magnetic interaction above a critical field. Materials in the superconducting state are perfect diamagnets, which means that they have high negative magnetic susceptibility and expel any flux of magnetic field within them. Such flux expulsion is referred to as the Meissner effect [2, 3]. In the particular case where the superconducting materials is shaped as a ring, the flux can go through the inner side of the ring and be trapped. Indeed, when the magnetic field is removed, a current that circulates around the ring is induced, and due to the superconducting nature of the material, this current does not decay (persistent current). The trapping of the magnetic flux in a superconducting ring is illustrated in Fig. 3-1.

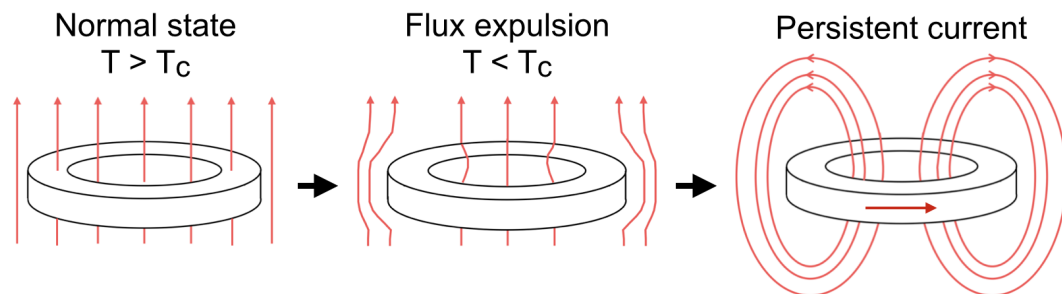


Figure 3-1: Meissner effect for a superconducting ring cooled under an external magnetic field. In the normal state, the magnetic flux can penetrate the material, which is no longer the case in the superconducting state. When the field is turned off, a persistent current is induced in the superconducting ring, thus trapping a magnetic flux.

As long as the ring is kept below its critical temperature T_c , the current continues

to circulate and is expressed as $I = \Phi/L$, where Φ is the flux of the magnetic field through the ring and L is the inductance of the ring. Such trapped flux has a very particular property, which is the fact that one can only trap discrete levels of magnetic flux [4]. As a result, the magnetic flux is quantized and is a multiple of the flux quantum $\Phi_0 = \pi\hbar/e = 2.068 \times 10^{-15} \text{ T}\cdot\text{m}^2$.

Josephson junctions The Josephson effect [5] corresponds to the possibility for electrons to tunnel from a superconductor region to another, through a resistive barrier. Because it involves the tunneling of a Cooper pair, the Josephson effect is much different from the tunnel effect of a single electron and it is possible only for currents lower than the critical current and for resistive barriers with a thickness smaller than the coherence length of the superconductor. Cooper pair tunneling does not require any excitations and can occur without applying voltage. The resistive barrier is called “weak link” and it can be made in several ways: two superconducting phases can be separated by an insulator, or a normal metal phase or even by natural grain boundaries and other imperfections in the superconducting phase. The superconducting quantum interference device (SQUID) magnetometry makes use of the Josephson effect in order to measure very small variations of magnetic flux, and the measurement is performed mainly by converting a magnetic flux in a voltage. A SQUID is a superconducting ring including one or two Josephson junctions. The structure of a SQUID is represented in Fig. 3-2, along with its circuitry.

It is necessary to avoid hysteresis in the I - V characteristic of the SQUID, so shunt resistors are connected in parallel to the Josephson junctions. In the superconducting state, an electrical current can exist without voltage. A bias current I_b is applied to the SQUID, with a value slightly higher than the critical current I_c of the super-

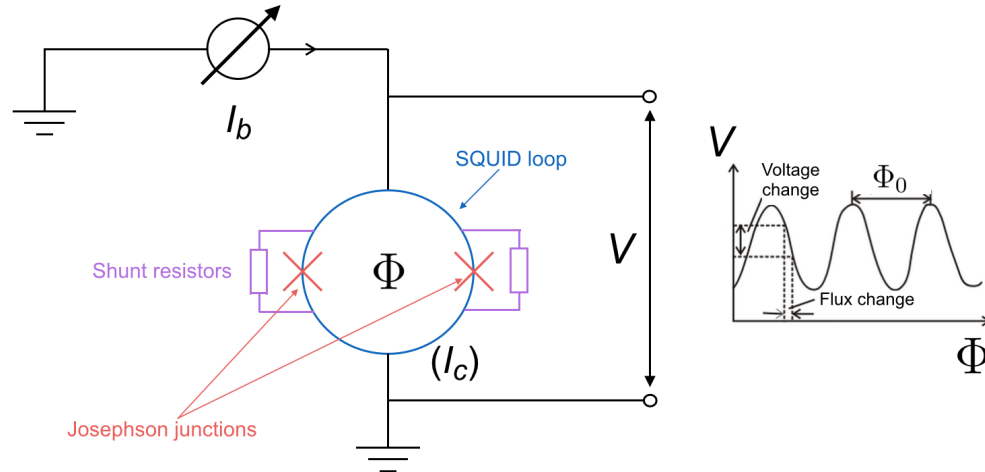


Figure 3-2: SQUID loop including two Josephson junctions. The voltage V varies periodically as a function of the flux Φ , each period corresponds to an increase of one quantum flux. I_c is the critical current of the superconductor.

conductor in order to set the operating point between the superconducting and the resistive behaviors [3]. When no external field is applied, the bias current splits equally in both branches of the SQUID loop. Then, if a field is applied, due to the perfect diamagnetic nature of the superconductor a screening field is induced, thus producing a field that acts towards cancelling the external magnetic flux. When the external magnetic flux increases to half a quantum flux $\Phi_0/2$, because of the quantization of the flux in the SQUID, the screening current in the SQUID is reversed in order to let the magnetic flux increase to Φ_0 , which is energetically more favorable. Therefore, the screening current will reverse each time the magnetic flux equals $(n + \frac{1}{2})\Phi_0$, where n is an integer. As a result, a change in the external magnetic flux induces a change in the voltage in the SQUID loop, and this voltage varies periodically as a function of the flux (the period being the magnetic flux quantum). Therefore, monitoring the variation of voltage in the SQUID loop gives a measure of the magnetic flux that has been coupled to the SQUID.

SQUID magnetometer A variable temperature SQUID magnetometer, shown in Fig. 3-3, has a Dewar with liquid helium, gas helium circuit and a heater in order to perform measurements at several temperatures. The temperature range for such equipment is usually from 1.8 to 400 K. The temperature in the sample space is regulated with a flow of helium gas. The heater is placed below the sample and the thermometer is located above the sample, thus ensuring that the whole sample region is in thermal equilibrium before the measurement. In the case of dc measurements, the applied magnetic field is static and the sample moves by the means of a motor attached to the sample holder. Such SQUID magnetometer has a uniform superconducting magnet to produce a uniform field in the sample area, between the superconducting detection coils. The SQUID is connected in series with the detection coils, and is shielded in a niobium cage. The variation of the flux Φ of the magnetic field in the circuit is related to the variation of the current I induced in the circuit by the following:

$$\frac{dI}{dt} = \frac{1}{L} \frac{d\Phi}{dt} = -\frac{V}{L}, \quad (3.1)$$

where V and L are the voltage induced across the coils and the inductance of the circuit, respectively. The measured quantity is actually a voltage, and when the sample goes through a coil, the flux of the magnetic field in that coil changes by an amount that is proportional to the magnetic moment of the sample. The detection coils are typically made of NbTi, for which the critical field allows measurement at fields as high as 9 T and the sensitivity is kept at 10^{-8} emu [3].

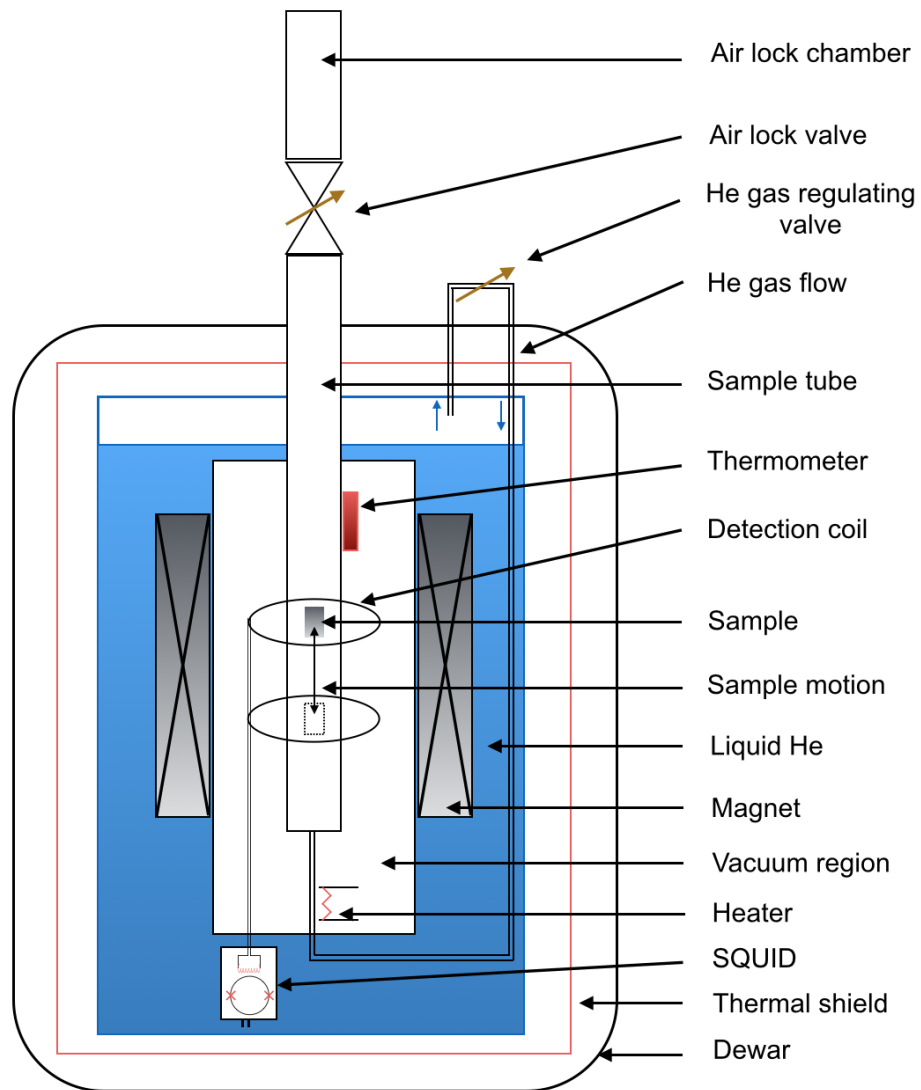


Figure 3-3: The different components of a variable temperature SQUID magnetometer. In this illustration, the SQUID has two Josephson junctions. The SQUID sensor is isolated in niobium shield immersed in liquid helium, so that it can keep its superconducting state by being protected from the sample heater and from the magnet.

Artifacts in SQUID magnetometry A SQUID magnetometer is actually a very sensitive device and care must be taken for the interpretation of the data. More precisely, one must distinguish the intrinsic and extrinsic contributions of the quantities measured by SQUID. Artifacts in the measured signals may have several origins [6], like the contamination of the samples due to the use of improperly cleaned tweezers, sample size effect, power supply of the magnet, which can all result in extrinsic signals leading to conclusions such as, for example, the presence of ferromagnetic order in diamagnetic materials [7, 8, 9, 10]. For this thesis, the main source of artifact comes from the superconducting magnet in the SQUID magnetometer.

As mentioned in the previous paragraph, since the magnetic field is generated by a superconducting coil, one must consider the presence pinned magnetic flux, especially when the magnet is discharged to set the field at zero. Because the superconducting material has defects, some volumes of phases in the normal state can nucleate in the superconducting phase, and therefore allow the magnetic flux to penetrate the material and be trapped after the magnet is discharged. The prediction of the value of such trapped field is difficult. From the experiments conducted for this thesis, the magnitude of the remanent trapped field seems to depend on the value of the highest previously applied field. This artifact field is mainly an issue when performing ultra-low-field measurements or when measuring magnetization cycles of very soft ferromagnets. In the latter case, if the trapped field is negative, a “negative” (anti-clockwise) hysteresis and a negative susceptibility can be measured, thus not representing the real behavior of the sample. Since Mn_5Ge_3 was found to be a very soft ferromagnet close to its Curie point, in order to avoid misleading conclusions, a fluxgate magnetometer was used to remove the trapped field before each measurement, where the information at very low field was required.

3.2 Magnetic anisotropy

The magnetic anisotropy originates from the fact that the energy of the ground state of a magnetic material is dependent on the direction of the magnetization vector. There are numerous kinds of magnetic anisotropy. For example, an anisotropy effect can arise from the rotation of the magnetization vector with respect to the crystallographic axes of the material (magnetocrystalline anisotropy) or with respect to the overall shape of the ferromagnetic sample (shape anisotropy). The easy direction of a ferromagnet is defined by the direction with minimum energy, on which the magnetization vector lies when the applied field is switched to zero. A material can have one or several of those directions. Conversely, a hard direction is for a direction with maximum energy. Easy directions are usually easy axes, although *unidirectional anisotropy* exists for more specific systems with an exchange bias field [11, 12, 13, 14, 15, 16], for which anisotropy is found only on one direction of an axis. In this section, the term *uniaxial anisotropy* will preferably be used. The magnetic anisotropy, along with the exchange interaction, is responsible for the existence of domain walls. The analysis of the magnetic anisotropy by the magnetic hysteresis loops can be difficult due to the formation of magnetic domain walls.

Spin-orbit interaction The source of magnetic anisotropy typically has two contributions: (i) the spin-orbit interaction and (ii) the dipole-dipole interaction. The spin-orbit interaction includes the magnetocrystalline and magneto-elastic contributions of the magnetic anisotropy, while the dipole-dipole interaction results in the shape anisotropy.

The orbital motion of an electron is ruled by a potential, which is imposed by the crystal lattice of a material, thus resulting in an orbit-lattice coupling. Con-

sequently, when a spin-orbit interaction occurs, the spin (i.e. the magnetization) becomes coupled to the crystal lattice. The energy band structure of a ferromagnet can be decomposed in a majority spin (\uparrow) band and a minority spin (\downarrow) band, those two sets of bands are separated by the exchange splitting energy. By considering the spin-orbit interaction as a perturbation of the exchange splitting energy [17], in accordance with the perturbation theory, it is shown that the energy correction and the orbital moment of the minority spin are related by the following relationship: $\Delta E_{\text{spin-orbit}} \propto -\frac{1}{4}\xi\hat{\mathbf{S}} \cdot \mathbf{L}^\downarrow$, where ξ is the radial part of the spin-orbit interaction, $\hat{\mathbf{S}}$ is the unit-vector for the spin direction, and \mathbf{L}^\downarrow is the orbital angular momentum of the minority spin. The magnetic anisotropy energy (MAE) is directly related to the anisotropy of orbital angular momentum, which is defined as the difference of momentum between the directions parallel ($\mathbf{L}^{\downarrow\parallel}$) and perpendicular ($\mathbf{L}^{\downarrow\perp}$) to an anisotropy axis.

$$\text{MAE} = \Delta E_{\text{spin-orbit}}^\perp - \Delta E_{\text{spin-orbit}}^\parallel \propto -\frac{1}{4}\xi (\mathbf{L}^{\downarrow\perp} - \mathbf{L}^{\downarrow\parallel}) \quad (3.2)$$

The easy axis corresponds to the one, for which the orbital angular momentum is the highest [17]. The relationship between the MAE and the anisotropy in orbital angular momentum is more easily observed in thin films [18] or sub-monolayer nanostructure [19].

Single-ion anisotropy The single-ion anisotropy is a model according to which the orbital of a magnetic ion interacts with the surrounding crystal field. The anisotropy in this model arises from the quenching of the orbital moment by the crystal field. The crystal field has the same symmetry as the crystal lattice, therefore through the orbit-lattice coupling, the orbital momentum is strongly coupled to the lattice. Because of the spin-orbit coupling, the interaction with the crystal field is transferred to the

spin momentum, thus weakening the coupling of the spins to the lattice. Therefore, when an external magnetic field is applied, the orbital momentum remains coupled to the lattice, while the spin momentum is more free to turn by the effect of the field due to its weaker interaction with the lattice.

In magnetic thin films, the contribution of the single-ion anisotropy spreads in the entire volume of the layer. In certain cases, the single-ion anisotropy can prevail over the shape anisotropy, which leads to a perpendicular anisotropy. An important aspect of this model is the fact that it allows to predict the temperature dependence of the anisotropy, as follows:

$$\left(\frac{K_n(T)}{K_n(0)}\right) = \left(\frac{M_S(T)}{M_S(0)}\right)^{n(n+1)/2}, \quad (3.3)$$

where $K_n(T)$ and $M_S(T)$ are the n th order anisotropy coefficient at temperature T and the saturation magnetization at temperature T , respectively. The relationship given by Eq. (3.3) is known as the Callen-Callen law [20, 21, 22, 23, 24, 25]. It is derived from models developed by Akulov [26] and Zener [27] and accounts for the fact that the variation of the anisotropy energy has the same origin as that of the magnetization, as explained in the previous paragraph.

The Callen-Callen law predicts that the anisotropy energy decreases much faster than the magnetization when the temperature increases, with a power equal to 3 in the case of uniaxial anisotropy and 10 or 21 in the case of cubic anisotropy.

3.3 Irreversibility in the temperature dependence of the magnetization

Magnetic systems with competitive exchange interactions among spins can lead to a spin-blocking process, thus resulting in a nonreversible thermal magnetization. In systems of ferromagnetic nanoparticles, superparamagnetic behavior can arise from the random magnetization flipping due to the thermal energy. Strong random and frustrated interactions among spins, can lead to materials in a spin-glass state. In addition, both categories of materials exhibit time dependent effects such as the aging, memory and rejuvenation processes.

3.3.1 Superparamagnetism

Superparamagnetism is commonly obtained in systems with weakly interacting magnetic nanoparticles. Below a critical size, which is about a few tens of nanometers, the formation of magnetic domains is no longer favored so that the spins in the nanoparticle rotate coherently. As a result, each nanoparticle is a single domain and behaves as a macrospin, called superspin and the weak interaction between the superspins lead to a superparamagnetic system. Therefore, the magnetic moment of a particle can be considered as a classical vector. The term of *superparamagnetism* was introduced by Bean and Livingston [28], due to the similarity in behavior with paramagnets. The nature of the interaction between the magnetic domains is a dipole-dipole interaction. In superparamagnetic materials, the randomness in the distribution of the domains leads to a frustration in the interaction. The nanoparticles have different anisotropy energy barriers, thus there is a broad distribution of relaxation times, which results in the slow magnetization dynamics and the presence of a blocking temperature T_b .

A schematic phase diagram is shown in Fig. 3-4. Above the Curie temperature, the thermal energy overcomes any exchange interactions that could occur among the spins and the material behaves as a regular paramagnet. For $T_b \leq T \leq T_C$, the nanoparticles order ferromagnetically, thus forming superspins. Although the thermal energy is weak enough to allow the ferromagnetic coupling within a particle, it is too strong to allow any coupling between nanoparticles.

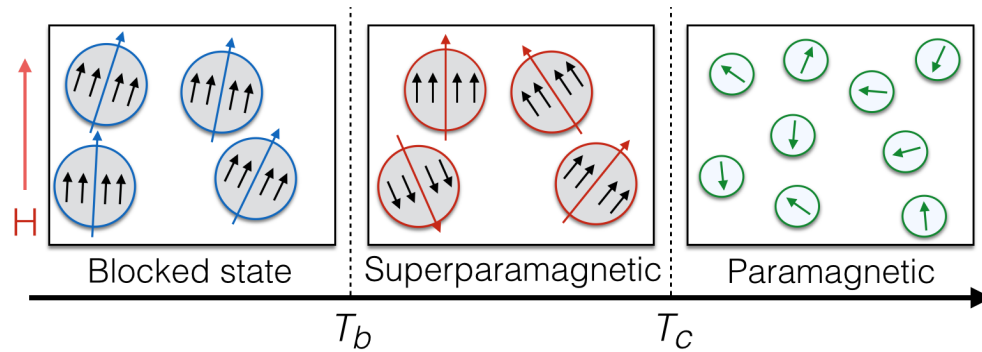


Figure 3-4: Schematic phase diagram of a superparamagnetic material. Above the Curie temperature, the material is a regular paramagnet, where the spins behave independently. For $T_b \leq T \leq T_C$, the nanoparticles order ferromagnetically in single domains. The weak interaction allows the thermal energy to orientate the superparamagnets randomly, thus giving a superparamagnet. Below T_b , the material enters a blocked state.

The result is that the material behaves in a similar manner as a paramagnet, except that the magnetic moment of an entire particle, instead of a single atom, tends to align with an external magnetic field. The energy required to rotate the magnetization of a nanoparticle corresponds to the magnetic anisotropy energy, defined earlier, and it depends on the particle's size and the nature of the material. As the temperature decreases, the alignment of the superspins with the applied field becomes more favorable. Below T_b , the magnetic moment of each nanoparticle is frozen, which results in a blocking state. So, one can distinguish two regimes in a superparamagnetic material, a superparamagnetic regime and a blocked regime.

If one considers an effective uniaxial anisotropy K for the particles, then the energy barriers are proportional to KV , where V is the volume of a nanoparticle. The magnetic energy for a single domain nanoparticle takes into account the anisotropy energy and the influence of the external magnetic field.

$$E_B = KV \sin^2 \theta_M - \mu H \cos(\theta_H - \theta_M), \quad (3.4)$$

where θ_M is the angle between the magnetic moment of a superspin and the easy axis of the particle, θ_H is the angle between the magnetic moment and the applied field, and $\mu = N\mu_{\text{at}}$ is the total magnetic moment of a super spin, with N and μ_{at} the number of spins and the atomic magnetic moment in the particle. The relaxation of the magnetic moment in a superparamagnet follows the Arrhenius law. The characteristic relaxation time is a function of the energy barrier as follows:

$$\tau = \tau_0 \exp(E_B/k_B T), \quad (3.5)$$

where $1/\tau_0$ is the attempt frequency characterizing a spin-flipping between the two directions of the easy axis of a particle, and k_B is the Boltzmann constant. Typical values of $1/\tau_0$ range from 10^9 to 10^{10} Hz [29, 30, 31]. As a result, under a magnetic field, the energy barrier is smaller than the anisotropy energy KV .

A noticeable feature of superparamagnets is the separation of the zero-field cooling and field-cooling magnetizations below the blocking temperature.

3.3.2 Spin glasses

A spin glass can be described as a group of interacting spins whose low-temperature state is frozen with no uniform or periodic pattern as found in ferromagnets or antiferromagnets. However, this disordered state is distinct from the disordered paramagnetic state due to its nonergodicity. Such freezing behavior is the product of the random and competing interactions between the spins, which do not favor any single configurations for the moments.

There has been discussions on whether such spin-glass state is only a progressive freezing process or another kind of magnetic phase [11, 32]. The presence of a cusp in the magnetic susceptibility precisely at the temperature corresponding to the freezing process is an indication of a second order phase transition, thus encouraging the definition of the spin-glass state as a magnetic phase. A spin-glass behavior is characterized by the presence of many metastable configurations for the spins, separated by a distribution of energy barriers. This results in the well-known fact that the magnetization dynamics is slow in such material, and it is usually evidenced by the frequency dependence of the position of the cusp in the susceptibility and by the time dependence of the remanent magnetization. Such features are very distinct from conventional magnetically ordered systems, for which no frequency dependence of the susceptibility is observed at the magnetic phase transition.

The time dependence of the remanent magnetization of spin glasses has been studied extensively using several models. Although no unique pattern was found, most spin glasses were proved to follow one of the following time dependences:

- logarithm law [33]

$$M(t) = M_0 - S_{RM} \ln(t), \quad (3.6)$$

where M_0 is a constant and S_{RM} is the magnetic viscosity accounting for the slow response of the magnetization to a variation in the magnetic field.

- power law [34]

$$M(t) \propto t^{-a(T,H)}, \quad (3.7)$$

where $a(T, H)$ is a temperature and field dependent exponent. For temperatures relatively far from the spin-glass transition, the power law can be written as $t^{-a(T,H)} = \exp[-a(T, H) \ln(t)] \simeq 1 - a(T, H) \ln(t)$, thus being consistent with the previously established logarithm law.

- stretched-exponential law [35]

$$M(t) \propto \exp \left[\frac{-A t^{1-n}}{1-n} \right], \quad (3.8)$$

where A is a constant, n depends on the temperature. For temperatures far from the spin-glass transition, $1 - n \simeq 1/3$, and for temperatures close to the transition the exponent becomes smaller.

The characteristic relaxation time in spin glasses is not verified by the Arrhenius law, contrary to materials with superparamagnetic behaviors, because it is no longer consistent with simple hopping over barriers and result in unphysical values. In order to take into account the magnetic interactions in spin glasses, Vogel and Fulcher adapted the Arrhenius law as follows [36, 37, 38]:

$$\tau = \tau_0 \exp \left[\frac{E_a}{k_{\text{B}}(T - T_0)} \right], \quad (3.9)$$

where E_a is the activation energy to overcome the energy barriers in the glassy state,

T_0 is a characteristic temperature, now called Vogel-Fulcher temperature, which was added in an empirical way to account for the exchange interactions between the spins.

While the magnetization is the order parameter for ferromagnets, it is not so for spin glasses. The spin glasses are defined by an order parameter, which is the third order of the nonlinear susceptibility. A divergence of the nonlinear susceptibility at the transition temperature T_F to the glassy state is expected for a transition to a spin-glass phase. Indeed, this has been predicted in the Edwards and Anderson model [39, 40]:

$$\chi_3 = \lim_{h \rightarrow 0} \frac{\partial M}{\partial h^3} = +\infty \quad (T = T_F) \quad (3.10)$$

$$M = M_s + \chi_1 h + \chi_2 h^2 + \chi_3 h^3 + \dots,$$

where, M_s is the spontaneous magnetization, χ_1 is the linear susceptibility, and χ_2 and χ_3 are the second order and third order non-linear susceptibility, respectively. Therefore, nonlinear susceptibility measurements are one of the most efficient ways to determine the presence of a real spin-glass phase transition.

The spin-glass behavior was first found in metallic materials, more specifically in noble metals including a small percentage of magnetic transition metal impurities, such as AuFe, AgMn, CuMn. The random dispersion of transition metal atoms in the metals produced the frustration and randomness necessary for obtaining a spin-glass state. Similar to the case of diluted metals, some diluted magnetic semiconductors have also been found to behave like spin glasses [41]. Some system based on Ge and Mn can also have spin-glass behavior, whether they are a disordered phase [42] or a $\text{Ge}_{1-x}\text{Mn}_x$ diluted magnetic semiconductor [43].

Spin glasses usually undergo a transition from the paramagnetic (PM) phase to the spin-glass (SG) state. However, some ferromagnetic (FM) materials have been

proved to be able to enter a SG phase [44], thus leading to successive transitions from PM to FM to SG. Such materials are called reentrant spin-glasses.

The phenomena of aging, rejuvenation and memory effects are common features for spin glasses, although they will not be discussed here. Detailed studies are provided in [45, 46, 47, 48, 49, 50]. It has been recently shown that superparamagnetic materials also show aging, rejuvenation, and memory effects [46, 51], just like spin glasses. Consequently, the measurement of such properties is not a proper method for distinguishing superparamagnets from spin-glasses.

Both spin glass and superparamagnetic materials show a thermal irreversibility in the zero-field-cooling and field-cooling magnetizations at relatively low temperatures. However, the field-cooling magnetization tends to increase monotonously for decreasing temperature in the case of superparamagnets, while it remains almost constant below the freezing temperature for spin glasses. This property is due to the fact that the superspins are not interacting in superparamagnets, while in the case of spin glasses, the random interactions between the spins makes it difficult for the external field to align the spins at low temperatures, as long as the field is low enough.

This paragraph on the spin-glass phase is an introduction for the study performed in Chapter 5 on the $\text{Mn}_5\text{Ge}_3/\text{Ge}$ heterostructure.

Bibliography

- [1] J. Bardeen, L. N. Cooper, and J. R. Schrieffer, *Phys. Rev.* **108**, 1175 (1957). [Cited on page(s) 61.]
- [2] W. Meissner and R. Oschensfeld, *Naturwiss.* **21**, 787 (1933). [Cited on page(s) 61.]
- [3] R. L. Fagaly, *Rev. Sci. Instrum.* **77**, 101101 (2006). [Cited on page(s) 61, 63, and 64.]
- [4] R. P. Feynman, R. B. Leighton, and M. Sands, *The Feynman Lectures on Physics*, (Addison-Wesley, Reading, MA, 1965), Vol. 3. [Cited on page(s) 62.]
- [5] B. D. Josephson, *Phys. Lett.* **1**, 251 (1962). [Cited on page(s) 62.]
- [6] M. Sawicki, W. Stefanowicz, and A. Ney, *Semicond. Sci. Technol.* **26**, 064006 (2011). [Cited on page(s) 66.]
- [7] D. W. Abraham, M. M. Frank, and S. Guba, *Appl. Phys. Lett.* **87**, 252502 (2005). [Cited on page(s) 66.]
- [8] M. A. Garcia, E. F. Pinel, J. de la Venta, A. Quesada, V. Bouzas, J. F. Fernández, J. J. Romero, M. S. M. González, and J. L. Costa-Krämer, *J. Appl. Phys.* **105**, 013925 (2009). [Cited on page(s) 66.]
- [9] R. Salzer, D. Spemann, P. Esquizani, R. Hohne, A. Setzer, K. Schindler, H. Schmidt, and T. Butz, *J. Magn. Magn. Mater.* **317**, 185 (2007). [Cited on page(s) 66.]
- [10] A. Bonanni *et al.*, *Phys. Rev. B* **75**, 125210 (2007). [Cited on page(s) 66.]
- [11] F. Hippert and H. Alloul, *J. Phys. (Paris)* **43**, 691 (1982). [Cited on page(s) 67, 73, and 121.]
- [12] J. B. Staunton, B. L. Gyorffy, J. Poulter, and P. Strange, *J. Phys.: Condens. Matter* **1**, 5157 (1989). [Cited on page(s) 67, 121, and 123.]
- [13] P. M. Levy, C. Morgan-Pond, and A. Fert, *J. Appl. Phys.* **53**, 2168 (1982). [Cited on page(s) 67, 121, and 123.]
- [14] T. Sato, *Phys. Rev. B* **41**, 2550 (1989). [Cited on page(s) 67 and 121.]
- [15] Y. Öner and H. Sari, *Phys. Rev. B* **49**, 5999 (1994). [Cited on page(s) 67 and 121.]
- [16] J. S. Kouvel, W. Abdul-Razzaq, and Kh. Ziq, *Phys. Rev. B* **35**, 1768 (1987). [Cited on page(s) 67 and 121.]

- [17] P. Bruno, Phys. Rev. B **39**, 865 (1989). [Cited on page(s) 3 and 68.]
- [18] D. Weller, J. Stöhr, R. Nakajima, A. Carl, M. G. Samant, C. Chappert, R. Mégy, P. Beauvillain, P. Veillet, G. A. Held, Phys. Rev. Lett. **75**, 3752 (1995). [Cited on page(s) 68.]
- [19] H. A. Dürr, G. van der Laan, and B. T. Thole, Phys. Rev. Lett. **76**, 3464 (1996) [Cited on page(s) 68.]
- [20] H.B. Callen, and E. Callen, J. Phys. Chem. Solids. **27**, 1271 (1966). [Cited on page(s) 69.]
- [21] E. R. Callen, and H. B. Callen, Phys. Rev. **129**, 578 (1963). [Cited on page(s) 69.]
- [22] R. Skomski, O. N. Mryasov, J. Zhou and D. J. Sellmyer, J. Appl. Phys. **99**, 08E916 (2006). [Cited on page(s) 69.]
- [23] O. N. Mryasov, U. Nowak, K. Y. Guslienko, and R. W. Chantrell, Europhys. Lett. **69**, 805 (2005). [Cited on page(s) 69.]
- [24] J. B. Staunton, S. Ostanin, S. S. A. Razee, B. L. Gyorffy, L. Szunyogh, B. Ginatempo, and E. Bruno, Phys. Rev. Lett. **93**, 257204 (2004). [Cited on page(s) 69.]
- [25] J. B. Staunton, L. Szunyogh, A. Buruzs, B. L. Gyorffy, S. Ostanin, and L. Udvardi, Phys. Rev. B **74**, 144411 (2006). [Cited on page(s) 69.]
- [26] N. Akulov, Z. Physik **100**, 197 (1936). [Cited on page(s) 69.]
- [27] C. Zener, Phys. Rev. **96**, 1335 (1954). [Cited on page(s) 69.]
- [28] C. P. Bean, and J. D. Livingston, J. Appl. Phys. **30**, 120S (1959). [Cited on page(s) 70.]
- [29] L. Néel, C. R. Acad. Sci., Paris **228**, 664 (1949). [Cited on page(s) 72.]
- [30] L. Néel, Ann. Geophys. **5**, 99 (1949). [Cited on page(s) 72.]
- [31] P. Allia, M. Coisson, M. Knobel, P. Tiberto, and F. Vinai, Phys. Rev. B **60**, 12207 (1999) [Cited on page(s) 72.]
- [32] V. Canella and J. A. Mydosh, Phys. Rev. B **6**, 4220 (1972). [Cited on page(s) 73.]
- [33] F. Holtzberg, J. L. Tholence, and R. Tournier, *Amorphous Magnetism II* (Plenum, New York, 1977), p.155. [Cited on page(s) 73.]
- [34] J. Ferré, J. Rajchenbach, and H. Maletta, J. Appl. Phys. **52**, 1697 (1981). [Cited on page(s) 74.]

- [35] R.V. Chamberlin, G. Mazurkevich, and R. Orbach, *Phys. Rev. Lett.* **52**, 867 (1984). [Cited on page(s) 74 and 112.]
- [36] K. Binder and A. P. Young, *Rev. Mod. Phys.* **58**, 801 (1986). [Cited on page(s) 74 and 112.]
- [37] H. Vogel, *Phys. Z.* **22**, 645 (1921). [Cited on page(s) 74.]
- [38] G. S. Fulcher, *J. Am. Ceram. Soc.* **8**, 339 (1925). [Cited on page(s) 74.]
- [39] M. Suzuki, *Prog. Theor. Phys.* **85**, 1151 (1977). [Cited on page(s) 75.]
- [40] T. Taniguchi, Y. Miyako, and J. Tholence, *J. Phys. Soc. Jpn.* **54**, 220 (1985). [Cited on page(s) 75.]
- [41] P. M. Shand, A. D. Christianson, T. M. Pekarek, L. S. Martison, J. W. Schweitzer, I. Miotkowski, and B. C. Crooker, *Phys. Rev. B* **58**, 12876 (1998). [Cited on page(s) 75.]
- [42] J. J. Hauser, *J. Magn. Magn. Mater.* **15-18**, 1387 (1980). [Cited on page(s) 75 and 121.]
- [43] C. Jaeger, C. Bihler, T. Vallaitis, S. T. B. Goennenwein, M. Opel, R. Gross, and M. S. Brandt, *Phys. Rev. B* **74**, 045330 (2006). [Cited on page(s) 75.]
- [44] T. Sato, T. Ando, T. Ogawa, S. Morimoto, and A. Ito, *Phys. Rev. B* **64**, 184432 (2001). [Cited on page(s) 76.]
- [45] S. Sahoo, O. Petravic, W. Kleemann, P. Nordblad, S. Cardoso, and P. P. Freitas, *Phys. Rev. B* **67**, 214422 (2003). [Cited on page(s) 76.]
- [46] M. Sasaki, P. E. Jönsson, H. Takayama, and H. Mamiya, *Phys. Rev. B* **71**, 104405 (2005). [Cited on page(s) 76.]
- [47] D. Parker, F. Ladieu, J. Hammann, and E. Vincent, *Phys. Rev. B* **74**, 184432 (2006). [Cited on page(s) 76.]
- [48] K. Jonason, E. Vincent, J. Hammann, J. P. Bouchaud, and P. Nordblad, *Phys. Rev. Lett.* **81**, 3243 (1998). [Cited on page(s) 76.]
- [49] V. Dupuis, E. Vincent, J. Hammann, J. E. Greedan, and A. S. Wills, *J. Appl. Phys.* **91**, 8384 (2002) [Cited on page(s) 76.]
- [50] Y. Sun, M. B. Salamon, K. Garnier, and R. S. Averback, *Phys. Rev. Lett.* **91**, 167206 (2003). [Cited on page(s) 76.]
- [51] R. K. Zheng, H. Gu, and X. X. Zhang, *Phys. Rev. Lett.* **93**, 139702 (2004). [Cited on page(s) 76.]

Chapter 4

Angular dependence of the ferromagnetic resonance in Mn_5Ge_3

This chapter gives a detailed characterization of the magnetocrystalline anisotropy in Mn_5Ge_3 epitaxial thin films by ferromagnetic resonance, in both in-plane and out-of-plane geometries. Section 4.2 describes and discusses the preliminary results measured by superconducting quantum interference device. Those results motivates an accurate study of the magnetocrystalline anisotropy in Mn_5Ge_3 , consequently section 4.3 will establish the free energy of the system. Finally, section 4.4 will show experimental and calculated results for the angular dependence of the ferromagnetic resonance field, and establish a temperature dependence for the magnetocrystalline anisotropy.

The content of this chapter was published in Physical Review B.

4.1 Introduction

In ferromagnetic materials, the magnetocrystalline anisotropy usually shows a dependence on temperature [1, 2, 3, 4]. For practical applications, it is therefore important to determine the behavior of the magnetocrystalline anisotropy in a wide temperature range, especially when the ferromagnet is intended to be used at a specific temperature range. While the temperature dependence of the magnetocrystalline anisotropy for ferromagnets with localized magnetic moments can be described quite well by the Callen-Callen law [1, 2], which is based on a single-ion anisotropy model, there are ferromagnetic transition metal alloys that can show more complicated behaviors [2, 3]. In this chapter, the presence of a weak perpendicular anisotropy in addition to the shape anisotropy is shown in a Mn_5Ge_3 thin film. Its contribution is studied experimentally and analytically by ferromagnetic resonance and despite the fact that it increases when the temperature decreases, it remains a lot weaker than the shape anisotropy. The interesting fact in this chapter is the invalidity of the Callen-Callen law for the Mn_5Ge_3 thin film [5].

4.2 Preliminary study of the magnetization cycles at several temperatures

The magnetic hysteresis cycles are measured by superconducting quantum interference device magnetometry, with an external magnetic field applied in the plane of the thin film. Measurements from 290 to 5 K are shown in Fig. 4-1. The temperature dependence of the saturation magnetization is shown in Fig. 4-2 and the Curie temperature is evaluated to be close to room temperature $T_C = 300 \pm 5$ K, which is consistent with the previous work on Mn_5Ge_3 . One can notice that the remanence ratio undergoes a significant change between 200 and 290 K, going from $M_R/M_S \simeq 0.85$ at 290 K to $M_R/M_S \simeq 0.25$ at 200 K [Fig. 4-1(b)-(e)], and it seems to stabilize at a value of 0.25 when the temperature is decreased further. The square shape of the hysteresis in the vicinity of the Curie temperature suggests that the applied magnetic field is almost parallel to the in-plane easy axis of the ferromagnetic thin film. Since this parallel alignment is no longer verified at lower temperature, it can reasonably be assumed that a non-negligible change in the magnetic anisotropy occurs between 200 and 290 K, thus altering the properties of the magnetization at zero field. Since Mn_5Ge_3 is in the form of a thin film in this work, the shape anisotropy is expected to be the dominant form of magnetic anisotropy, which confines the magnetization in the plane of the film. This fact is confirmed by the measurement of the perpendicular magnetization [Fig. 4-1(f) shows the perpendicular magnetization at 30 K], from which we conclude that the remanence and coercive field are very small, and the saturation field is higher than for the in-plane magnetization.

The crystal lattice of Mn_5Ge_3 has a hexagonal structure, which makes the hexagonal c axis become the easy magnetization axis for the bulk material. The epitaxial re-

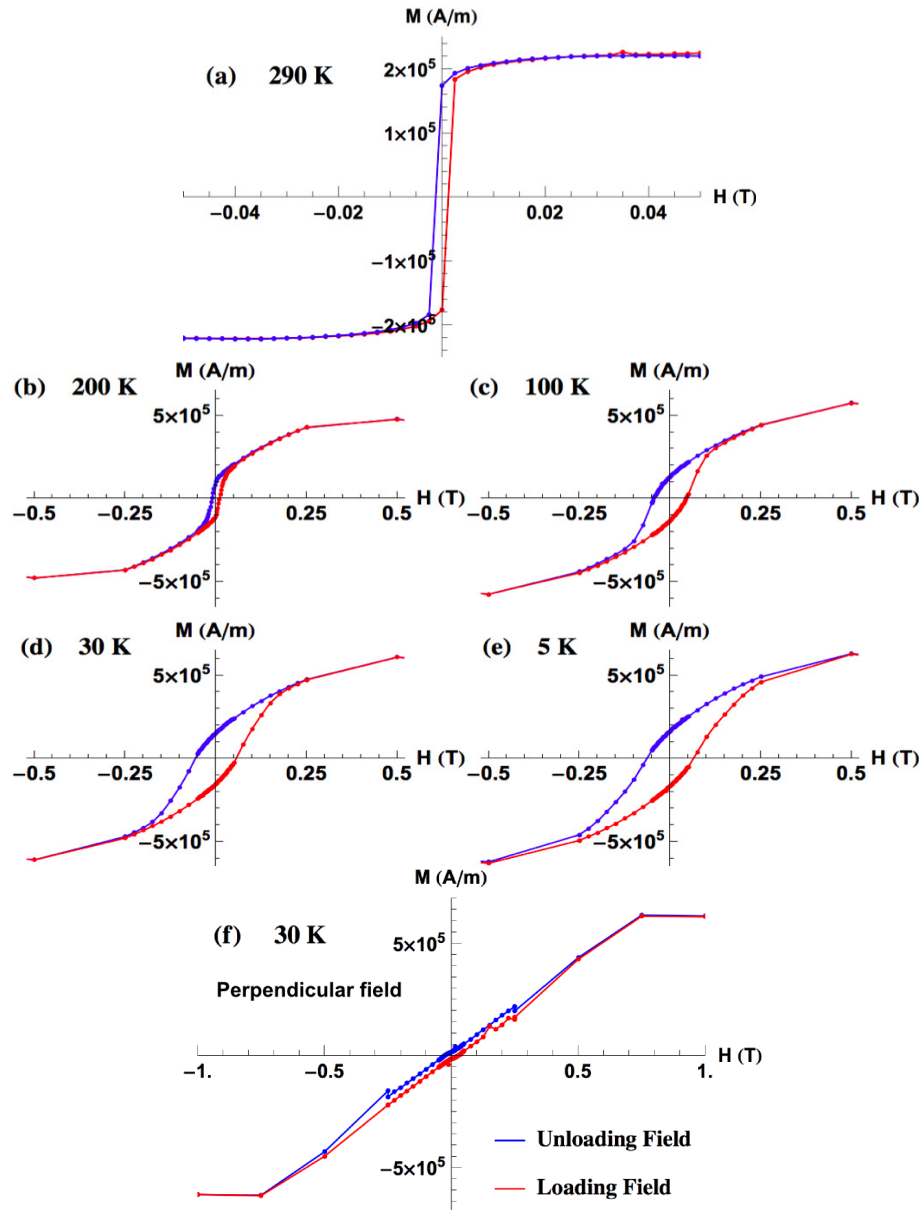


Figure 4-1: Field-dependence of the magnetization at (a) 290 K, (b) 200 K, (c) 100 K, (d) 30 K and (e) 5 K. In (a)-(e) the magnetic field is applied in the plane of the thin film. In (f), the measurement is done at 30 K with a field applied in the normal axis of the thin film

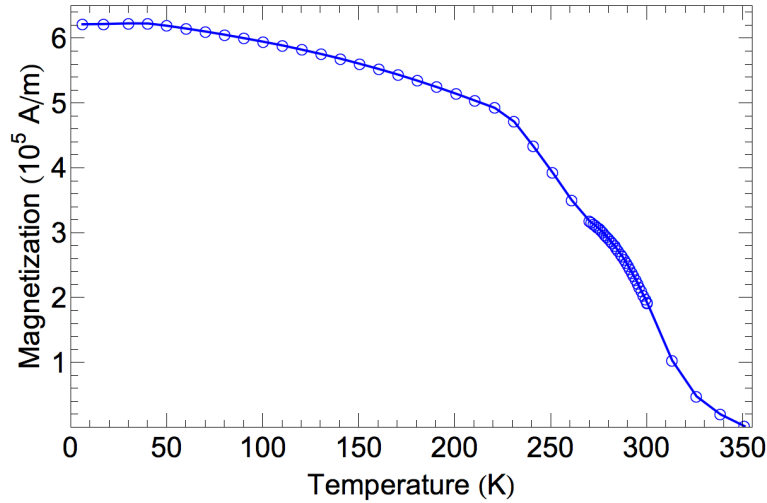


Figure 4-2: Saturation magnetization as a function of temperature, measured by SQUID with an external applied field of 1.5 T. From this data, the Curie temperature is evaluated to be $T_c = 300 \pm 5$ K.

relationship $\text{Mn}_5\text{Ge}_3(001)/\text{Ge}(111)$ allows the ferromagnet to grow on the Ge substrate with its easy axis parallel to the sample's normal axis, which can hypothetically result in a perpendicular magnetocrystalline anisotropy. Even though preliminary SQUID measurements suggest that such perpendicular magnetocrystalline anisotropy is weak, it is necessary to establish its temperature dependence in order to evaluate how much it competes with the shape anisotropy for the entire temperature range. The purpose of the following sections is to determine whether the magnetocrystalline anisotropy in Mn_5Ge_3 thin films, although weak, can have an influence on the magnetization cycles or not.

4.3 Free energy of the system

The ferromagnetic resonance (FMR) technique is a sensitive method to analyze the magnetocrystalline anisotropy in ferromagnetic thin films or heterostructures [6, 7, 8, 9]. In order to perform such analyses, it is essential to determine the mathematical expression of the free energy, which is characterized by the symmetry of the material, and that of the resonance condition. The magnetic anisotropy energy (MAE) corresponds to the work required to rotate the magnetization from an easy axis to another direction. According to the second principle of thermodynamics, for a closed system, the free energy F of the magnetic material is related to the work W_{MAE} and to the entropy S as follows: $dF = -\delta W_{\text{MAE}} - SdT$. FMR measurements are usually performed at constant temperatures, which leads to the variation of the free energy being equal to the work $dF = -\delta W_{\text{MAE}}$. The coordinate system used in this work is defined in Fig. 4-3.

Because Mn_5Ge_3 has a hexagonal lattice, the following will concentrate on the free energy for a hexagonal symmetry. Considering that the magnetic sample is saturated in order to suppress any effects from the magnetic domain walls, one can expand the free energy of directive cosines α_i ($i = 1, 2, 3$), which are defined as the projections of the magnetization on three unit vectors determined by the crystal lattice. Therefore, the general form of the magnetic anisotropy free energy [10] is:

$$F_{\text{MA}} = b_i \alpha_i + b_{ij} \alpha_i \alpha_j + b_{ijk} \alpha_i \alpha_j \alpha_k + b_{ijkl} \alpha_i \alpha_j \alpha_k \alpha_l + \dots \quad (4.1)$$

where the tensors b_{ijkl} reflect the properties of the crystal symmetry. The components of b_{ijkl} can be transformed by a rotation of coordinate axes or can be invariant under the specific symmetry conditions imposed by a particular crystal structure. As a

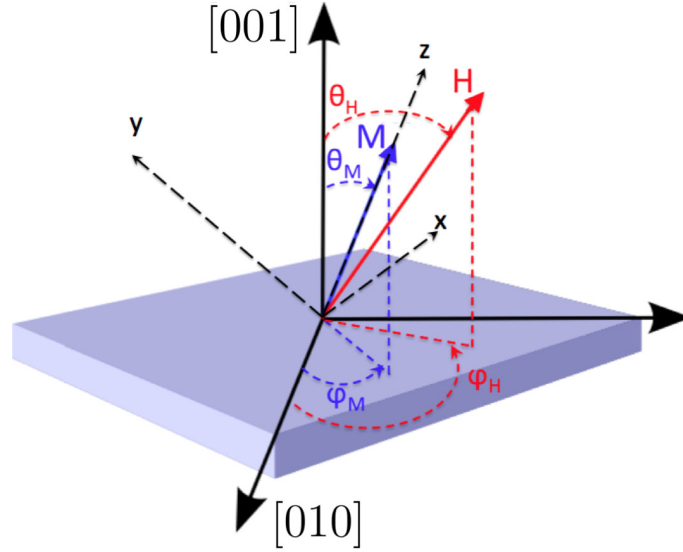


Figure 4-3: Coordinate system used for the theoretical FMR analysis. θ_M and θ_H are the out-of-plane magnetization angle and field angle, respectively. ϕ_M and ϕ_H are the in-plane magnetization and field angle, respectively. The sample's normal axis is the $[001]$ direction of the Mn_5Ge_3 crystal, and (x, y, z) is defined so that the z direction is parallel to the magnetization.

result, the components b_{ijkl} must satisfy:

$$b_{ijkl\dots n} = \sum_{p=1}^3 \sum_{q=1}^3 \sum_{r=1}^3 \dots \sum_{u=1}^3 \sigma_{ip} \sigma_{jq} \sigma_{kr} \dots \sigma_{nu} b_{pqr\dots u}. \quad (4.2)$$

The matrices $[\sigma]$ are generating matrices, which account for the permissive symmetry operations required to describe a crystal structure [10, 11]. It can be shown that all the crystal classes can be described by 10 matrices and their multiplications. The two first matrices represent the unity matrix and the matrix of point inversion through a unit cell, respectively. The two next matrices represent a twofold rotation parallel and perpendicular to the z axis, respectively. The z axis is an arbitrary axis in the crystal lattice. Similarly, the next matrices describe threefold or fourfold rotations, the presence of a bar means that the rotation is followed by a point inversion. The last

matrix is essentially relevant for the cubic symmetry and corresponds to a threefold rotation parallel to the diagonal of the cubic unit cell.

$$\begin{aligned}
 [\sigma^{\text{unit}}] &= \begin{pmatrix} 1 & 0 & 0 \\ 0 & 1 & 0 \\ 0 & 0 & 1 \end{pmatrix} & [\sigma^{\text{inv}}] &= \begin{pmatrix} -1 & 0 & 0 \\ 0 & -1 & 0 \\ 0 & 0 & -1 \end{pmatrix} \\
 [\sigma^{2\perp z}] &= \begin{pmatrix} -1 & 0 & 0 \\ 0 & 1 & 0 \\ 0 & 0 & -1 \end{pmatrix} & [\sigma^{2\parallel z}] &= \begin{pmatrix} -1 & 0 & 0 \\ 0 & -1 & 0 \\ 0 & 0 & 1 \end{pmatrix} \\
 [\sigma^{\bar{2}\perp z}] &= \begin{pmatrix} 1 & 0 & 0 \\ 0 & -1 & 0 \\ 0 & 0 & 1 \end{pmatrix} & [\sigma^{\bar{2}\parallel z}] &= \begin{pmatrix} 1 & 0 & 0 \\ 0 & 1 & 0 \\ 0 & 0 & -1 \end{pmatrix} \\
 [\sigma^{3\parallel z}] &= \begin{pmatrix} -\frac{1}{2} & \frac{\sqrt{3}}{2} & 0 \\ -\frac{\sqrt{3}}{2} & -\frac{1}{2} & 0 \\ 0 & 0 & 1 \end{pmatrix} & [\sigma^{4\parallel z}] &= \begin{pmatrix} 0 & 1 & 0 \\ -1 & 0 & 0 \\ 0 & 0 & 1 \end{pmatrix} \\
 [\sigma^{\bar{4}\parallel z}] &= \begin{pmatrix} 0 & -1 & 0 \\ 1 & 0 & 0 \\ 0 & 0 & -1 \end{pmatrix} & [\sigma^{3\text{dia}}] &= \begin{pmatrix} 0 & 1 & 0 \\ 0 & 0 & 1 \\ 1 & 0 & 0 \end{pmatrix}
 \end{aligned}$$

Hexagonal symmetry The free energy of Mn_5Ge_3 will be deduced by the expression of the free energy of a hexagonal structure in the $[001]$ direction. In this work, the anisotropy energies K are indexed by the anisotropy order, for example K_2 will correspond to a second order uniaxial anisotropy energy and K_4 will correspond to

a fourth order cubic anisotropy energy. For the hexagonal symmetry, the generating matrices are $[\sigma^{\text{inv}}]$, $[\sigma^{2\perp[001]}]$, $[\sigma^{2\parallel[001]}]$, and $[\sigma^{3\parallel[001]}]$. The matrix $[\sigma^{3\parallel[001]}]$ is essential to describe the threefold rotation along the $[001]$ axis of Mn_5Ge_3 , and the product σ^{hex} of all the matrices gives a sixfold symmetry. The use of $[\sigma^{\text{inv}}]$ means that the unit cell is centrosymmetrical, therefore all the odd order anisotropy terms must vanish. The matrix $[\sigma^{2\perp[001]}]$ used along with Eq. (4.2) implies that the components of σ^{hex} are non zero for $i = p$, or $j = q$, or \dots or $n = u$. Moreover, the product $\sigma_{ip}\sigma_{jq}\sigma_{kr}\dots\sigma_{nu}$ equals to -1 when the index 2 appears an odd number of times, which means that the terms that include the index 2 an odd number of times must vanish as well. In a similar manner, $[\sigma^{2\parallel[001]}]$ implies that all the coefficients that contain the index 3 must vanish [11]. Taking all those restrictions into account, the first nonvanishing term is the second order anisotropy energy $b_{ij}\alpha_i\alpha_j = b_{11}(\alpha_1^2 + \alpha_2^2)$. Expanding to the sixth order, the magnetocrystalline anisotropy free energy of the hexagonal structure is given by:

$$F_{\text{MA}} = K_0 + K_{2\perp}(\alpha_1^2 + \alpha_2^2) + K_{4\perp}(\alpha_1^2 + \alpha_2^2)^2 + K_{6\perp}(\alpha_1^2 + \alpha_2^2)^3 + K_{6\parallel}(\alpha_1^2 - \alpha_2^2)(\alpha_1^4 - 14\alpha_1\alpha_2 + \alpha_2^4). \quad (4.3)$$

One can notice that in the hexagonal symmetry, an in-plane magnetocrystalline anisotropy only appears from the sixth order. By using the system coordinate shown in Fig. 4-3, the free energy can be re-written as:

$$F_{\text{MA}} = K_{2\perp} \sin^2 \theta_M + K_{4\perp} \sin^4 \theta_M + K_{6\perp} \sin^6 \theta_M + K_{6\parallel} \sin^6 \theta_M \sin(6\varphi_M). \quad (4.4)$$

Since F_{MA} is an energy, the constant term can be set to zero. For this work, only the second order is kept ($K_{2\perp}$ will be noted K_{\perp}) for the magnetocrystalline anisotropy,

therefore one has

$$F_{\text{MA}} = -K_{\perp} \cos^2 \theta_M. \quad (4.5)$$

Beside the magnetocrystalline contribution of the anisotropy, one must take into consideration the presence of the shape anisotropy, since Mn_5Ge_3 is in the form of a thin film. The shape of a thin films induces a translational symmetry breaking of the ferromagnet, leading to an in-plane distortion in the volume. By using the approximation that the thin film is an infinite plane, the shape anisotropy energy, which favors the alignment of the magnetization in the plane of the thin film can be expressed as:

$$F_{\text{shape}} = 2\pi M^2 \cos^2 \theta_M. \quad (4.6)$$

In addition, the interactions existing at the interface between Mn_5Ge_3 and the Ge substrate can cause the existence of an uniaxial in-plane anisotropy term:

$$F_{\text{uniaxial}} = -\frac{1}{2} M H_{\parallel} \sin^2 \theta_M \cos^2 \left(\varphi_M - \frac{\pi}{3} \right), \quad (4.7)$$

where the angle $\pi/3$ accounts for the hexagonal symmetry and H_{\parallel} is the in-plane uniaxial anisotropy field.

Finally, by including the contribution of the Zeeman energy due to the external magnetic field, the total free energy $F_{\text{hexagonal}}$ is given by the following expression:

$$F_{\text{hexagonal}} = F_{\text{Zeeman}} + F_{\text{shape}} - \frac{1}{2} M H_{\perp} \cos^2 \theta_M - \frac{1}{2} M H_{\parallel} \sin^2 \theta_M \cos^2 \left(\varphi_M - \frac{\pi}{3} \right), \quad (4.8)$$

where $F_{\text{Zeeman}} = -HM[\cos \theta_M \cos \theta_H + \sin \theta_M \sin \theta_H \cos(\varphi_M - \varphi_H)]$ and $H_{\perp} = 2K_{\perp}/M$. This total free energy is used for the characterization by ferromagnetic resonance discussed in the next section.

4.4 Resonance condition for the angular dependent FMR in the hexagonal symmetry

The ferromagnetic resonance technique detects the magnetic excitations occurring in the microwave regime. The resonance condition is found by deriving the free energy and the Landau-Lifshitz-Gilbert (LLG) equation. The theoretical model does not take into account the presence of domain wall dynamics, therefore during the experiments, care has been taken so that the ferromagnetic resonance field is higher than the saturation field of the sample. This ensures that the magnetization in Mn_5Ge_3 can be considered as a macrospin. The LLG equation for the dynamics of the magnetization $\mathbf{M}(t)$ is

$$\frac{d\mathbf{M}(t)}{dt} = -\gamma\mathbf{M}(t) \times \mathbf{H}_{\text{eff}} + \frac{\alpha}{M_S}\mathbf{M}(t) \times \frac{d\mathbf{M}(t)}{dt}, \quad (4.9)$$

where γ is the gyromagnetic ratio, α is the damping constant, and M_S is the saturation magnetization. Only the first term is required to study the angular dependence of the resonance field. The second term, which involves the damping constant, is related to the angular dependence of the linewidth of the FMR signals. As discussed in detail in [12, 13, 14], the resonance condition is determined by deriving the LLG equation and the following relationship with the free energy is established as follows:

$$\left(\frac{\omega}{\gamma}\right)^2 = \frac{1}{M_S^2} \frac{\partial^2 F_{\text{hexagonal}}}{\partial \theta_M^2} \left(\frac{1}{\sin^2 \theta_M} \frac{\partial^2 F_{\text{hexagonal}}}{\partial \varphi_M^2} + \frac{\cos \theta_M}{\sin \theta_M} \frac{\partial F_{\text{hexagonal}}}{\partial \theta_M} \right) - \frac{1}{M_S^2} \left(\frac{1}{\sin \theta_M} \frac{\partial^2 F_{\text{hexagonal}}}{\partial \theta_M \partial \varphi_M} - \frac{\cos \theta_M}{\sin^2 \theta_M} \frac{\partial F_{\text{hexagonal}}}{\partial \varphi_M} \right)^2. \quad (4.10)$$

By using Eq. (4.10), the final form of the resonance condition for a Mn₅Ge₃ thin film is established:

$$\left(\frac{\omega}{\gamma}\right)^2 = [H_{\text{FMR}} \times a_1 + b_1] [H_{\text{FMR}} \times a_1 + b_2] - b_3^2, \quad (4.11)$$

where H_{FMR} is the resonance field, ω is the microwave frequency, and the terms a_1 , b_1 , b_2 , b_3 are calculated to be:

$$a_1 = \cos \theta_M \cos \theta_H + \sin \theta_M \sin \theta_H \cos (\varphi_M - \varphi_H),$$

$$b_1 = - [4\pi M_S - H_{\perp} + H_{\parallel} \cos^2 (\varphi_M - \frac{\pi}{3})] \cos (2\theta_M),$$

$$b_2 = -(4\pi M_S - H_{\perp}) \cos^2 \theta_M - H_{\parallel} \left[(\cos \theta_M \cos (\varphi_M - \frac{\pi}{3}))^2 - \cos 2(\varphi_M - \frac{\pi}{3}) \right],$$

$$b_3 = H_{\parallel} \cos \theta_M \sin (\varphi_M - \frac{\pi}{3}) \cos (\varphi_M - \frac{\pi}{3}).$$

The calculations using Eq. (4.11) and the experimental results will allow to determine the values of the anisotropy fields. The experiments are carried out using X-band electron paramagnetic resonance spectrometer (microwave frequency of 9.08 GHz) using both in-plane and out-of-plane geometries, as illustrated in Fig. 4-4.

In-plane geometry The in-plane FMR spectra are measured for several temperatures between 18 and 300 K. The spectra at 295 and 100 K are shown in Fig. 4-5 and no angle dependence of the ferromagnetic resonance field is visible. The same result is obtained for the whole range of temperature.

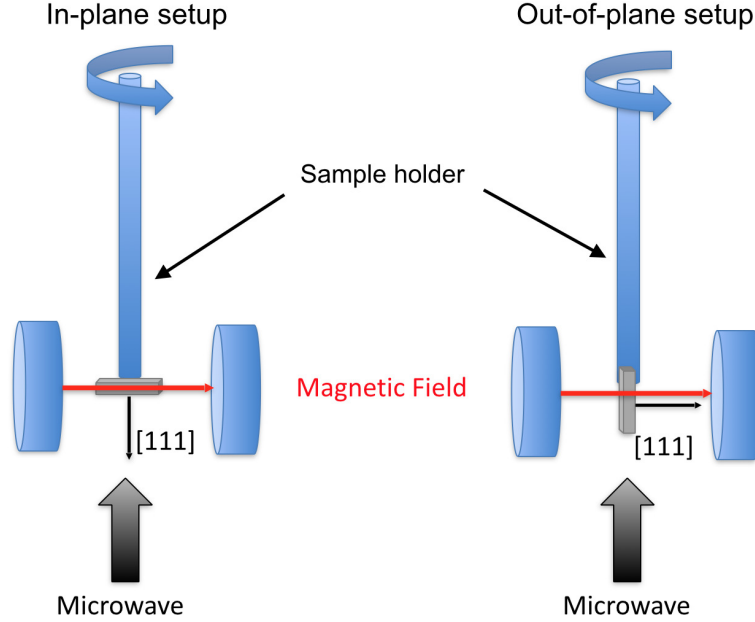


Figure 4-4: In-plane and out-of-plane configurations for the ferromagnetic resonance measurements. The normal direction of the thin film corresponds to the [111] direction of the Ge substrate.

Therefore, with those experimental results, it can be inferred that the plane of the thin film has no magnetic anisotropy, since all the directions seem to be equivalent and the orientation of the magnetic field does not affect the resonance. The consequence for the in-plane uniaxial anisotropy, defined in the previous paragraph, is $H_{\parallel} = 0$ thus making the in-plane uniaxial anisotropy free energy term [Eq. (4.7)] vanish. This result is important for the analysis of the out-of-plane FMR spectra because it significantly simplifies the resonance condition, given in Eq. (4.11), and results in $\varphi_M = \varphi_H$.

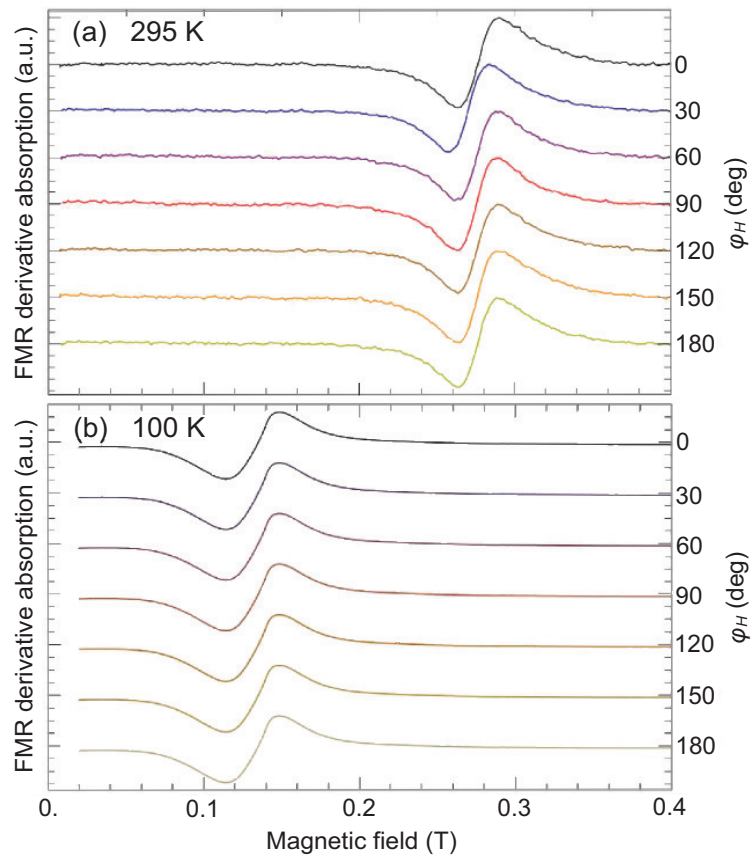


Figure 4-5: FMR signals recorded as the first derivative of the microwave absorption in the in-plane geometry at (a) 295 K and (b) 100 K. The in-plane measurements show no variation of resonance field as a function of angle, so magnetocrystalline anisotropy is absent in the sample's plane. The in-plane FMR measurements were performed by applying a magnetic field in the sample's plane and rotating it along its normal axis.

Out-of-plane geometry The effective magnetic field \mathbf{H}_{eff} includes the external magnetic field and a field \mathbf{H}_M , which takes into account the contributions of the perpendicular anisotropy H_{\perp} and the demagnetizing field induced by the magnetization $\mathbf{M}(t)$. It is defined as $\mathbf{H}_{\text{eff}} = \mathbf{H} + \mathbf{H}_M$ and can be expressed in the (x, y, z) coordinate system, where

$$\mathbf{H} = H \begin{pmatrix} 0 \\ \sin(\theta_M - \theta_H) \\ \cos(\theta_M - \theta_H) \end{pmatrix}, \quad (4.12)$$

$$\mathbf{H}_M = -(4\pi M_S - H_{\perp}) \cos \theta_M \begin{pmatrix} 0 \\ \sin \theta_M \\ \cos \theta_M \end{pmatrix}. \quad (4.13)$$

Since the demagnetizing field and the perpendicular anisotropy have the same symmetry in the thin film, it is natural to include them in the same contribution. The out-of-plane field angle dependence of the ferromagnetic resonance field is obtained from the static equilibrium condition $\mathbf{M} \times \mathbf{H}_{\text{eff}} = \mathbf{0}$, and the ferromagnetic resonance condition. Those two conditions lead to the following set of equations:

$$\left\{ \begin{array}{l} 2H \sin(\theta_H - \theta_M) + 4\pi M_{\text{eff}} \sin 2\theta_M = 0 \\ \left(\frac{\omega}{\gamma}\right)^2 = [H_{\text{FMR}} \cos(\theta_H - \theta_M) - 4\pi M_{\text{eff}} \cos(2\theta_M)] \\ \quad \times [H_{\text{FMR}} \cos(\theta_H - \theta_M) - 4\pi M_{\text{eff}} \cos^2 \theta_M], \end{array} \right. \quad (4.14)$$

where $4\pi M_{\text{eff}} = 4\pi M_S - H_{\perp}$ is the effective magnetization. An out-of-plane FMR series of spectra is given in Fig. 4-6, and it can be seen that a higher magnetic fields

are necessary in order to obtain resonance in the out-of-plane directions. Although the maximum of resonance field is in the perpendicular direction, the spectra themselves give no information about the perpendicular anisotropy.

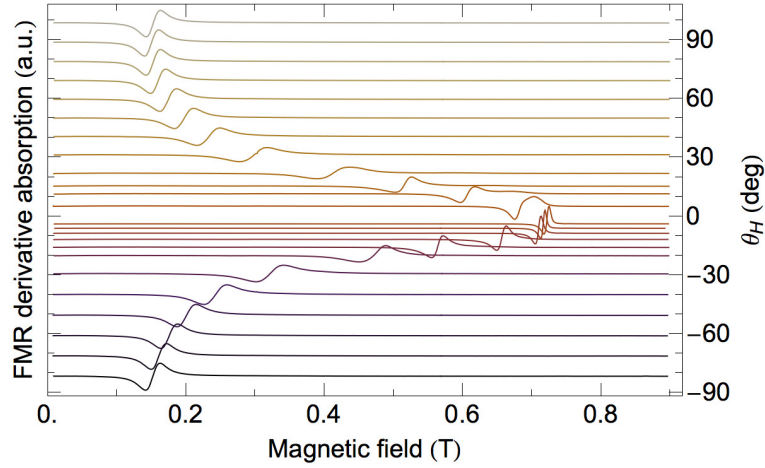


Figure 4-6: FMR spectra in the out-of-plane geometry for the Mn_5Ge_3 thin film, measured at 200 K. One can see that a higher external magnetic field is required in order to obtain the resonance as the direction of the field gets closer to the normal axis of the sample.

According to the above-mentioned model, since the sample has no in-plane magnetocrystalline anisotropy, the only possible form of magnetocrystalline anisotropy is an uniaxial perpendicular anisotropy. Concerning the out-of-plane FMR measurements (Fig. 4-6), the presence of the demagnetizing field makes it difficult to distinguish the contribution of the perpendicular uniaxial anisotropy from that of the demagnetizing field regarding the shift of the resonance field position, when the direction of the field approaches the normal axis of the thin film. For that reason, the values of $4\pi M_{\text{eff}}$ obtained by FMR are compared with the values of $4\pi M_S$ obtained by SQUID in the previous section. A difference between the two magnetizations will show the presence of a perpendicular anisotropy. One can also note in Fig. 4-6 that although the FMR spectra for angles close to 90° have a derivative Lorentzian lineshape, the

spectra close to the [001] direction have an asymmetric lineshape. The lineshape of the FMR spectra is sensitive to inhomogeneity in the out-of-plane directions, and this inhomogeneity probably comes from defects due to the lattice mismatch or to the nonhomogeneous composition at the $\text{Mn}_5\text{Ge}_3/\text{Ge}$ interface [15].

The angular dependencies of the out-of-plane ferromagnetic resonance fields are shown in Fig. 4-7. One can see that, for each temperature, there is a match between the experimental angular dependence of H_{FMR} and the solutions of the set of equations (4.14), so the total free energy was defined in a correct manner and the assumption that $H_{\parallel} = 0$ is reasonable. By solving the set of equations 4.14, one obtains the effective magnetization for each temperature, as summarized in Table 4.1.

Temperature dependence of the magnetocrystalline anisotropy The experimental anisotropy coefficients are plotted as a function of temperature along with the theoretical behavior predicted by the Callen-Callen law [Eq. (3.3)] in Fig. 4-8 (red curve). One can clearly notice that the anisotropy coefficients obtained by FMR deviate from the cubic magnetization law for almost the entire temperature range. Therefore, the Callen-Callen law is not applicable to this case. However, although a

Table 4.1: Comparison between the saturation magnetization obtained by SQUID and the effective magnetization obtained by FMR. The perpendicular anisotropy field is calculated by subtracting the two magnetizations. K_{\perp} is deduced from $H_{\perp} = 2K_{\perp}/M_{\text{S}}$.

T (K)	$4\pi M_{\text{eff}}$ (A/m)	$4\pi M_{\text{S}}$ (A/m)	H_{\perp} (A/m)	K_{\perp} (A ² /m ²)
18	4.4×10^5	6.2×10^5	1.8×10^5	5.6×10^{10}
100	4.0×10^5	5.8×10^5	1.8×10^5	5.2×10^{10}
200	3.4×10^5	5.1×10^5	1.7×10^5	4.3×10^{10}
230	3.1×10^5	4.7×10^5	1.6×10^5	3.8×10^{10}
295	1.1×10^5	2.2×10^5	1.1×10^5	1.2×10^{10}

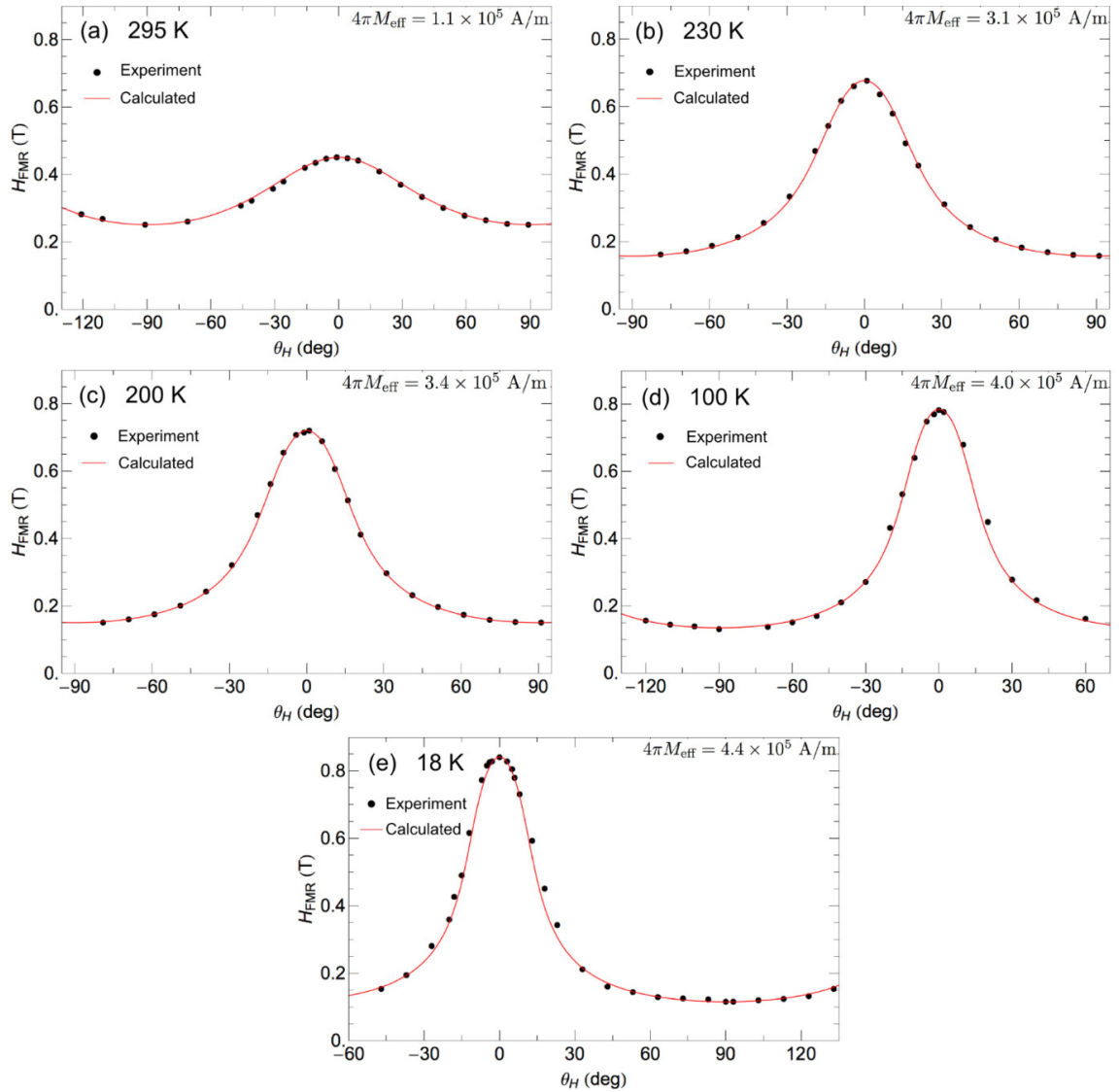


Figure 4-7: Resonance field as a function of the field angle to the normal axis of the sample for different temperatures. The experimental data is given by the black dots and the solutions of the set of equations (4.14) are given by the red curves. The effective magnetizations at each temperature are calculated from the above-mentioned model. The theoretical model for FMR in Mn_5Ge_3 fits well the experimental measurements.

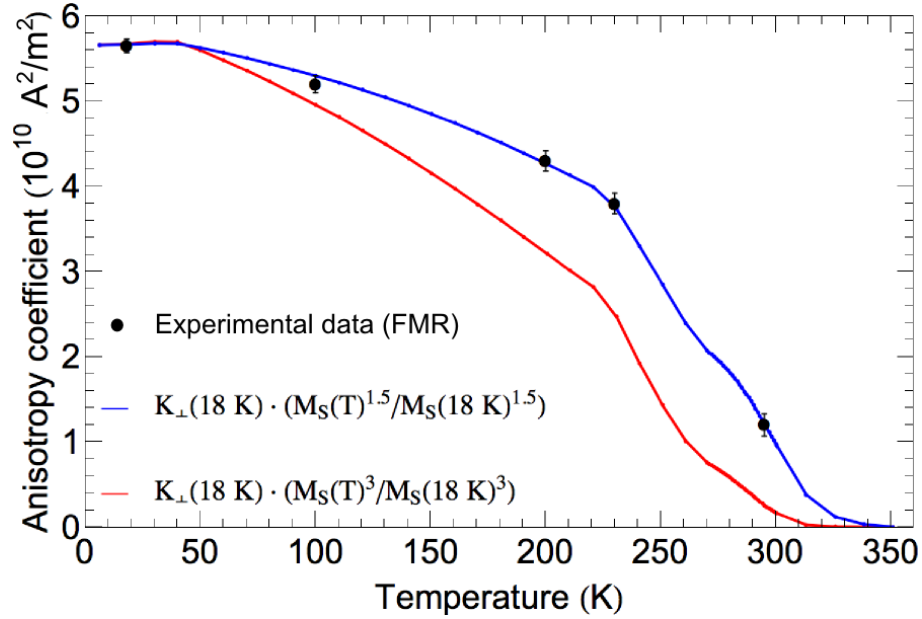


Figure 4-8: The red curve represents the calculated prediction from the Callen-Callen law for a second order uniaxial anisotropy, and the blue curve represents the calculated temperature dependence of the anisotropy energy coefficient assuming that it varies as the cubic square root of the magnetization. The calculations are based on the results given in Fig. 4-2. A cubic square root law seems to be more adapted to describe magnetocrystalline anisotropy in Mn_5Ge_3 than the cubic relationship predicted by the Callen-Callen law. The Callen-Callen law appears to be valid only at low temperatures (< 40 K). The fact that the experimental values of the magnetocrystalline anisotropy energy still follow a power law of the magnetization suggests that a coupling between the crystal field and the magnetization still exists, however in a different way than suggested by the single-ion anisotropy model.

cubic law is not valid for Mn_5Ge_3 , the experimental points seem to vary as the cubic square root of the magnetization. A relatively good fit with the corresponding curve can be seen in Fig. 4-8 (blue curve). The red and blue curves in Fig. 4-8 are calculated from the temperature dependence of the magnetization measured by SQUID in Fig. 4-2. In ferromagnets, the magnetocrystalline anisotropy usually decreases much faster than the magnetization when the temperature increases, with exponents equal to 10 or 21 for cubic anisotropies and 3 for uniaxial anisotropy [16, 17, 18, 19, 20]. In the present case, the perpendicular anisotropy energy still decreases faster than the magnetization but at a slower pace than what can be found in literature. According to Eq. (4.8) and the result deduced from Fig. 4-8, the perpendicular anisotropy energy can be written as:

$$F_{\perp} = K_{\perp}(18 \text{ K}) \left(\frac{M_S(T)}{M_S(18 \text{ K})} \right)^{1.5} \cos^2 \theta_M. \quad (4.15)$$

As a result, the temperature dependence of the perpendicular anisotropy to shape anisotropy energy ratio is given by the following relationship:

$$\frac{F_{\perp}}{F_{\text{Shape}}} \propto \frac{1}{\sqrt{M_S(T)}} \quad (4.16)$$

Such temperature dependence shows that the out-of-plane anisotropy energy actually becomes a lot weaker than that of the shape anisotropy when the temperature decreases. Consequently, although the presence of a perpendicular magnetocrystalline anisotropy has been evidenced by FMR, it does not explain why the in-plane remanence ratio of the Mn_5Ge_3 thin film decreases at low temperatures. We can thus infer that the decrease of the in-plane remanence ratio has another origin, such as the variation of the strain in the Mn_5Ge_3 crystal, when the temperature decreases.

4.5 Summary

This chapter showed that the squareness of the in-plane magnetization curve changes from a value close to 1 in the Curie temperature range to a much lower value at low temperatures. An out-of-plane magnetocrystalline anisotropy was thought to be the most reasonable candidate to induce such property. The analysis conducted by FMR indicated that a perpendicular anisotropy exists in the Mn_5Ge_3 thin film, however it is shown to be too weak to contribute to the change of the in-plane magnetization at zero field. Knowing that the bulk material has an easy magnetization axis along the hexagonal c axis, the perpendicular anisotropy in the thin film is allowed to exist due to the epitaxial relationship $\text{Mn}_5\text{Ge}_3/\text{Ge}(111)$. Even though the perpendicular anisotropy is not the direct cause of the decrease of the in-plane remanence ratio, its temperature dependence shows interesting and unusual features. It has been reported that the temperature dependence of the magnetocrystalline anisotropy given by the Callen-Callen law represents a relatively good model for ferromagnets with localized magnetic moments [21]. This is because it is based on a single-ion anisotropy model, as described in the previous chapter. In this work, the perpendicular uniaxial anisotropy still follows a power law, but the power is lower than the predicted value. The ferromagnetism in Mn_5Ge_3 has been theoretically predicted to originate from interactions between Mn sites [22]. Due to the half-filled $3d$ electron shell, Mn atoms have a zero orbital angular momentum, thus making the magnetic moments be localized. In the Mn_5Ge_3 compound, the different coordinations of both Mn sites may be the origin of the metallic properties of the material, but the localized character of the magnetic moments would normally allow the single-anisotropy model to be valid. Since Mn is alloyed with Ge in this case, some hybridization between p orbitals of Ge and $3d$ orbitals of Mn sites can decrease the degree of localization of the magnetic

moment, thus contributing to reducing the exponent in the anisotropy energy. It has also been established in a previous study that itinerant ferromagnetism can induce a decrease of the exponent in the power law [21], a notable case is the $L1_0$ phase of FePt, for which the exponent in the temperature dependence is 2.1 instead of 3 for the uniaxial anisotropy [21, 23, 24]. Such temperature dependence has successfully been modeled by using a relativistic description of the electronic structures, which gives a better description of the spin-orbit interaction [23, 24]. The magnetic properties of Mn_5Ge_3 are different from FePt, so the deviation from the Callen-Callen law may not be explained by the same mechanism in both materials. So, the reason why the exponent is decreased from 3 to 1.5 in Mn_5Ge_3 remains to be studied more thoroughly. A Curie-Weiss fitting of high temperature susceptibility measurements could bring more information about the degree of localization of the magnetic moments provided by the Mn sites. However, such measurement at high temperatures may not be straightforward to realize, since it can alter the crystal quality of Mn_5Ge_3 during the process. In addition, one can also note that the assumptions made in the Callen-Callen model do not take into account the variations of internal magnetostriction with thermal expansion [2, 18, 19]. Internal magnetostriction can destroy the power law given by the Callen-Callen model, by introducing lower and higher power terms in the anisotropy energy [25]. When the temperature varies, the c/a ratio of the hexagonal Mn_5Ge_3 can also change and lead to the presence an internal magnetostriction, which represents a magnetic anisotropy that is intrinsic to the material. Further investigations need to be carried out to verify if the internal magnetostriction in Mn_5Ge_3 and the hybridization of the orbitals can be the reason why the temperature dependence of its perpendicular uniaxial anisotropy deviates from the Callen-Callen law.

Bibliography

- [1] H.B. Callen, and E. Callen, *J. Phys. Chem. Solids.* **27**, 1271 (1966). [Cited on page(s) 81.]
- [2] E. R. Callen, and H. B. Callen, *Phys. Rev.* **129**, 578 (1963). [Cited on page(s) 81 and 101.]
- [3] R. Skomski, O. N. Mryasov, J. Zhou and D. J. Sellmyer, *J. Appl. Phys.* **99**, 08E916 (2006). [Cited on page(s) 81.]
- [4] J. F. Herbst, *Rev. Mod. Phys.* **63**, 819 (1991). [Cited on page(s) 81.]
- [5] A. Truong, A. O. Watanabe, T. Sekiguchi, P. A. Mortemousque, T. Sato, K. Ando, and K. M. Itoh, *Phys. Rev. B* **90**, 224415 (2014). [Cited on page(s) 39, 81, and 109.]
- [6] X. Liu, and J. K. Furdyna, *J. Phys.: Condens. Mater.* **18**, 245 (2006). [Cited on page(s) 85.]
- [7] X. Liu, Y. Sasaki, and J. K. Furdyna, *Phys. Rev. B* **67**, 205204 (2003). [Cited on page(s) 85.]
- [8] X. Liu, W. L. Lim, L. V. Titova, M. Dobrowolska, J. K. Furdyna, M. Kutrowski and T. Wojtowicz, *J. Appl. Phys.* **98**, 063904 (2005). [Cited on page(s) 85.]
- [9] Y. Y. Zhou, X. Liu, J. K. Furdyna, M. A. Scarpulla, and O. D. Dubon, *Phys. Rev. B* **80**, 224403 (2009). [Cited on page(s) 85.]
- [10] H. Zabel, and S. D. Bader, *Magnetic heterostructures*, Springer Tracts of Modern Physics (Springer, Berlin Heidelberg 2008). [Cited on page(s) 85 and 86.]
- [11] R. R. Birss: *Symmetry and Magnetism*, Series of Monographs on selected Topics in Solid State Physics, ed by E. P. Wohlfarth (North-Holland Publishing Co., Amsterdam, John Wiley and Sons, New York 1966). [Cited on page(s) 3, 86, and 88.]
- [12] T. L. Gilbert, *Phys. Rev.* **100**, 1243 (1955). [Cited on page(s) 90.]
- [13] H. Goldstein, *Klassische Mechanik*, 11th ed (AULA-Verlag, Wiesbaden 1991). [Cited on page(s) 90.]
- [14] L. Baselgia, M. Warden, F. Waldner, S. L. Hutton, J. E. Drumheller, Y. Q. He, P. E. Wigen, M. Marysko, *Phys. Rev. B* **38**, 2237 (1988). [Cited on page(s) 90.]

- [15] A. Truong, A. O. Watanabe, P. A. Mortemousque, K. Ando, T. Sato, T. Taniyama, and K. M. Itoh, *Phys. Rev. B* **91** 214425 (2015). [Cited on page(s) 6, 96, and 111.]
- [16] C. Zener, *Phys. Rev.* **96**, 1335 (1954). [Cited on page(s) 99.]
- [17] S. Chikazumi, *Physics of Magnetism* (Wiley, New York, 1964), Chap. 12. [Cited on page(s) 99.]
- [18] W. J. Carr, *J. Appl. Phys.* **29**, 436 (1958). [Cited on page(s) 99 and 101.]
- [19] W. J. Carr, *Phys. Rev.* **109**, 1971 (1958). [Cited on page(s) 99 and 101.]
- [20] Y. Fu, I. Barsukov, R. Meckenstock, J. Lindner, Y. Zhai, B. Hjörvarsson, and M. Farle, *J. Appl. Phys.* **115**, 172605 (2014). [Cited on page(s) 99.]
- [21] O. N. Mryasov, U. Nowak, K. Y. Guslienko, and R. W. Chantrell, *Europhys. Lett.* **69**, 805 (2005). [Cited on page(s) 100 and 101.]
- [22] A. Stroppa, M. Peressi, *Mater. Sci. Semicond. Process.* **9**, 841 (2006). [Cited on page(s) 100.]
- [23] J. B. Staunton, S. Ostanin, S. S. A. Razee, B. L. Gyorffy, L. Szunyogh, B. Ginatempo, and E. Bruno, *Phys. Rev. Lett.* **93**, 257204 (2004). [Cited on page(s) 101.]
- [24] J. B. Staunton, L. Szunyogh, A. Buruzs, B. L. Gyorffy, S. Ostanin, and L. Udvardi, *Phys. Rev. B* **74**, 144411 (2006). [Cited on page(s) 101.]
- [25] E. R. Callen and H. B. Callen, *Phys. Rev.* **129**, 578 (1963). [Cited on page(s) 101.]

Chapter 5

Interfacial spin-glass-like state in $\text{Mn}_5\text{Ge}_3/\text{Ge}(111)$

This chapter deals with the fact that despite having no in-plane anisotropy, as demonstrated by the FMR measurements, the $\text{Mn}_5\text{Ge}_3/\text{Ge}(111)$ heterostructure has a thermal irreversibility in the in-plane magnetization. Such irreversibility is attributed to a spin-glass-like behavior, which is the result of the interaction between the ferromagnetic Mn_5Ge_3 and a spin-glass region at the $\text{Mn}_5\text{Ge}_3/\text{Ge}$ interface. The interfacial spin-glass region is reasonably assumed to correspond to the “magnetic dead layer” formed at the $\text{Mn}_5\text{Ge}_3/\text{Ge}$ interface. Section 5.2 describes the samples used for the characterization of the spin-glass-like behavior. It is followed by the analysis of the magnetic properties under dc and ac field (section 5.3). Finally, it is shown that the glassy behavior in the present system is dependent on the growth conditions and the thickness of the ferromagnetic Mn_5Ge_3 layer (section 5.4).

The content of this chapter was published in Physical Review B.

5.1 Introduction

Recently, the emergence of exchange bias was reported for a spin-glass/ferromagnet hybrid system [1, 2]. The exchange bias in spin glasses can lead to the unique property of inverted bias effect [2, 3], which causes the exchange bias field to change sign for a temperature range below the blocking temperature. Interactions of spin currents with spin glasses are also investigated actively [4]. Such phenomena are expected to play important roles in the wide range of future spintronics applications. One of routes to form nanoscale spin-glass/ferromagnet systems are making use of the so-called naturally formed spin-glass layers. Recent studies have shown that a spin-glass behavior can arise at the surface or interface of a magnetically ordered phase due to a surface effect, or a translational symmetry breaking of the lattice [5, 6, 7, 8, 9]. This leads to spin frustration and competing magnetic interactions in the ordered phase. Understanding of such competing interactions at the surface or interface is of great importance because it can significantly alter the properties of magnetic thin films. In this chapter, it is demonstrated that Mn_5Ge_3 in the form of a thin film on $\text{Ge}(111)$ does not show simple ferromagnetism in the entire range of temperature below its Curie point. The zero-field-cooling (ZFC) and field-cooling (FC) curves indicate the presence of an irreversibility in the thermal magnetization. This property is unexpected since Mn_5Ge_3 grows epitaxially on $\text{Ge}(111)$ with no disordered secondary phases [10, 11, 12, 13, 14, 15]. The characterization of the ac susceptibility leads to the conclusion that the nature of the irreversibility is similar to that of a spin glass, despite the fact that no apparent signs of disorder or frustrated interactions can be found in such thin films. The spin-glass-like behavior is attributed to the presence of a “ferromagnetically dead” layer at the $\text{Mn}_5\text{Ge}_3/\text{Ge}$ interface. Indeed, thickness dependence of the ferromagnetism in $\text{Mn}_5\text{Ge}_3/\text{Ge}(111)$ has shown that a thickness of

approximately 1.7 nm of the thin film from the $\text{Mn}_5\text{Ge}_3/\text{Ge}$ interface does not contribute to the total magnetic moment [16]. However, no magnetic characterization of such “ferromagnetically dead” layer was performed in the past. The present work shows that the spin-glass nature attributed to the “dead” layer explains the frustrated interactions observed in the ferromagnetic part of the film. It is also shown that the temperature dependence of the stability of the spin-glass-like state in a magnetic field follows the de Almeida-Thouless line. Although high spin injection efficiency was predicted theoretically [17], the interfacial spin-glass-like behavior shown experimentally in this work could have an influence on the properties of spin currents.

5.2 Experimental details and structural characterization

In this chapter, three specific samples are analyzed, as presented in Table 5.1. Their relative growth conditions are important for the following study. Sample A will be the reference sample and its magnetic properties will be compared to that of sample B, which was grown with a higher growth temperature, and sample C, which is thicker. The following brief structural characterization confirms that the variation of thickness or growth temperature leads to the same structure for the Mn_5Ge_3 layers. The solid state reaction between the Ge single crystal and the deposited Mn is triggered by annealing the samples at 150 (samples A and C) or 200°C (sample B) and leads to the formation of Mn_5Ge_3 . The annealing process yields the well-established $\sqrt{3} \times \sqrt{3}$ structure of the $\text{Mn}_5\text{Ge}_3(001)$ surface, as can be seen from the RHEED patterns in Fig. 5-1(a). The in-plane atomic distances are evaluated to be $d_{\text{Mn}_5\text{Ge}_3} = 7.112 \text{ \AA}$ in the [010] direction of the hexagonal Mn_5Ge_3 and $d_{\text{Ge}} = 6.937 \text{ \AA}$ in the $[11\bar{2}]$ direction

of the cubic Ge substrate, thus leading to a lattice mismatch of about 2.4%, which is in agreement with the previous work [18]. Transmission electron microscope confirms the epitaxial growth of Mn_5Ge_3 on the Ge single crystal and the absence of clusters of other stoichiometries in either layers [see Fig. 5-1(b)]. The XRD patterns shown in Fig. 5-1(c), confirm the epitaxial relationship $\text{Mn}_5\text{Ge}_3(001)/\text{Ge}(111)$ and do not detect the presence of crystals other than Mn_5Ge_3 . The in-plane distances $d_{\text{Mn}_5\text{Ge}_3}$ and d_{Ge} were evaluated from off-normal angle XRD measurements. The XRD and RHEED patterns obtained for the three samples are identical.

The temperature dependence of the magnetic properties of the sample at very low field were measured by superconducting quantum interference device magnetometry. As mentioned earlier, due to the high sensitivity of the Mn_5Ge_3 thin films to negative fields trapped in the SQUID, the residual fields were removed by using a fluxgate magnetometer in a magnetic shield of permalloy in order to perform ultra-low field measurements.

Table 5.1: List of the samples studied in this work. T_{SPE} is the growth temperature and refers to the annealing temperature used for the solid phase epitaxy of Mn_5Ge_3 . The final thickness of Mn_5Ge_3 layer is $t_{\text{Mn}_5\text{Ge}_3}$. The variation of the Curie temperature T_C will be discussed in Section 5.4.

Name	Deposited Mn (nm)	T_{SPE} (°C)	$t_{\text{Mn}_5\text{Ge}_3}$ (nm)	T_C (K)
Sample A	~ 11.4	150	~ 17	294
Sample B	~ 11.4	200	~ 17	290
Sample C	~ 22.8	150	~ 29.5	288

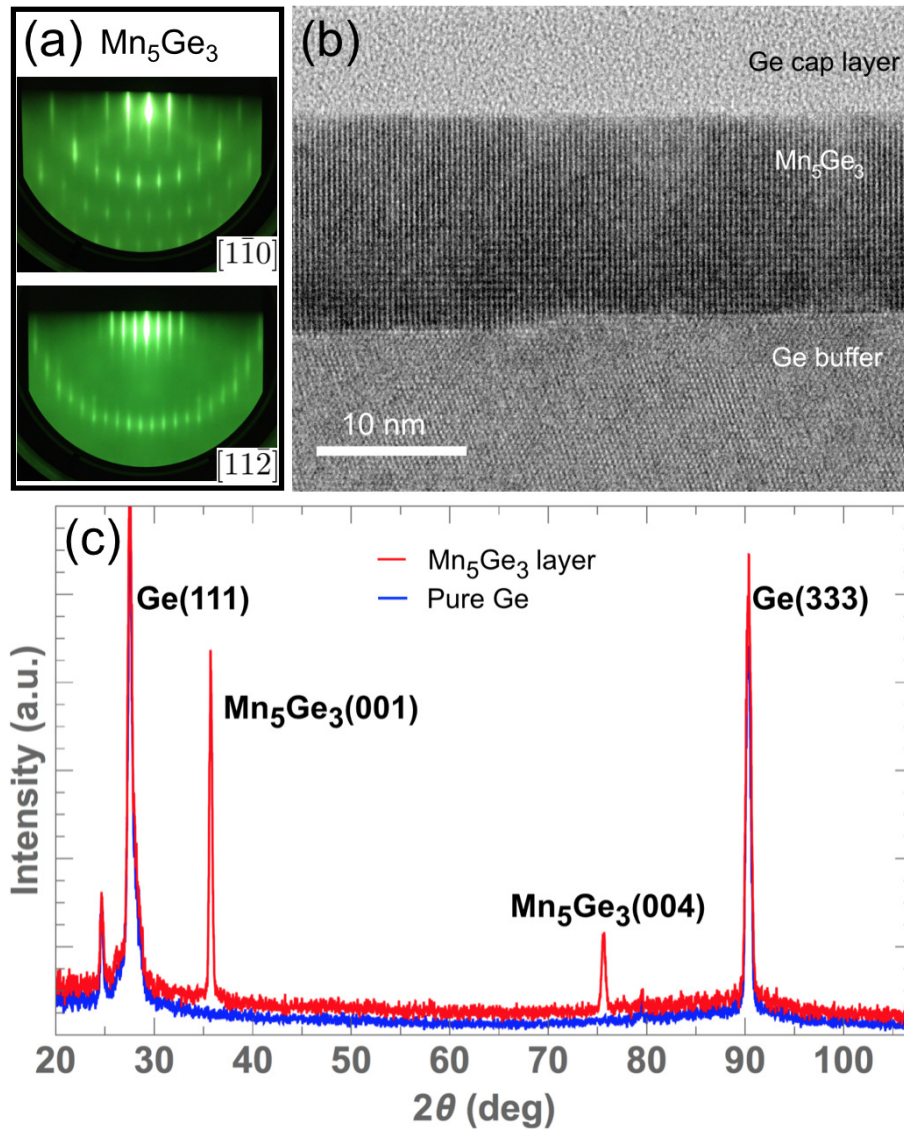


Figure 5-1: (a) RHEED patterns of the $\sqrt{3} \times \sqrt{3}$ structure of Mn_5Ge_3 in the $[1\bar{1}0]$ and $[11\bar{2}]$ directions of the Ge substrate. (b) TEM image of $\text{Mn}_5\text{Ge}_3(001)$ on Ge(111). (c) An XRD pattern of the Mn_5Ge_3 layer (red curve) and a pure Ge sample (blue curve) measured using Cu $K\alpha$ radiation. The peak at $2\theta = 24.6^\circ$ is the signal from Ge under Cu $K\beta$ radiation originating from the x-ray source.

5.3 Characterization of the irreversible thermal magnetization

5.3.1 Zero-field-cooling and field-cooling magnetization curves

In this section, the field and temperature dependencies of the magnetization are studied on sample A, using a static dc field. The properties of samples B and C will be discussed in Section 5.4. The magnetic hysteresis curves undergo a change of squareness depending on the temperature, as discussed in the previous chapter (also see [19]). In the vicinity of the Curie temperature [Fig. 5-2(a)], the magnetization switching is mainly driven by irreversible domain wall motion. However, for lower temperatures, the magnetization process is driven by coherent rotation [see Fig. 5-2(b)]. The remanence ratio is close to unity close to the Curie point, but decreases and stabilizes at a lower value ($M_R/M_S \simeq 0.50$) below 200 K. The strong variation in remanence ratio between 290 and 200 K suggests that a sudden change in the in-plane magnetic anisotropy or in the exchange interaction occurs [20]. However, the analysis by ferromagnetic resonance conducted in the previous work [19], detected no in-plane magnetic anisotropy in Mn_5Ge_3 thin films.

The temperature dependence of the magnetization is measured under the ZFC and FC conditions, as shown in Fig. 5-3. The ZFC (FC) curves are measured by warming the sample from 10 to 350 K after cooling it from room temperature at zero field (at the measuring field). A thermal irreversibility clearly appears for fields below 2000 Oe, as evidenced by the non-zero difference between the FC and ZFC magnetizations. For each field, the presence of a Hopkinson maximum [21, 22, 23] is observed. The FC curves do not vary monotonously; they initially decrease with

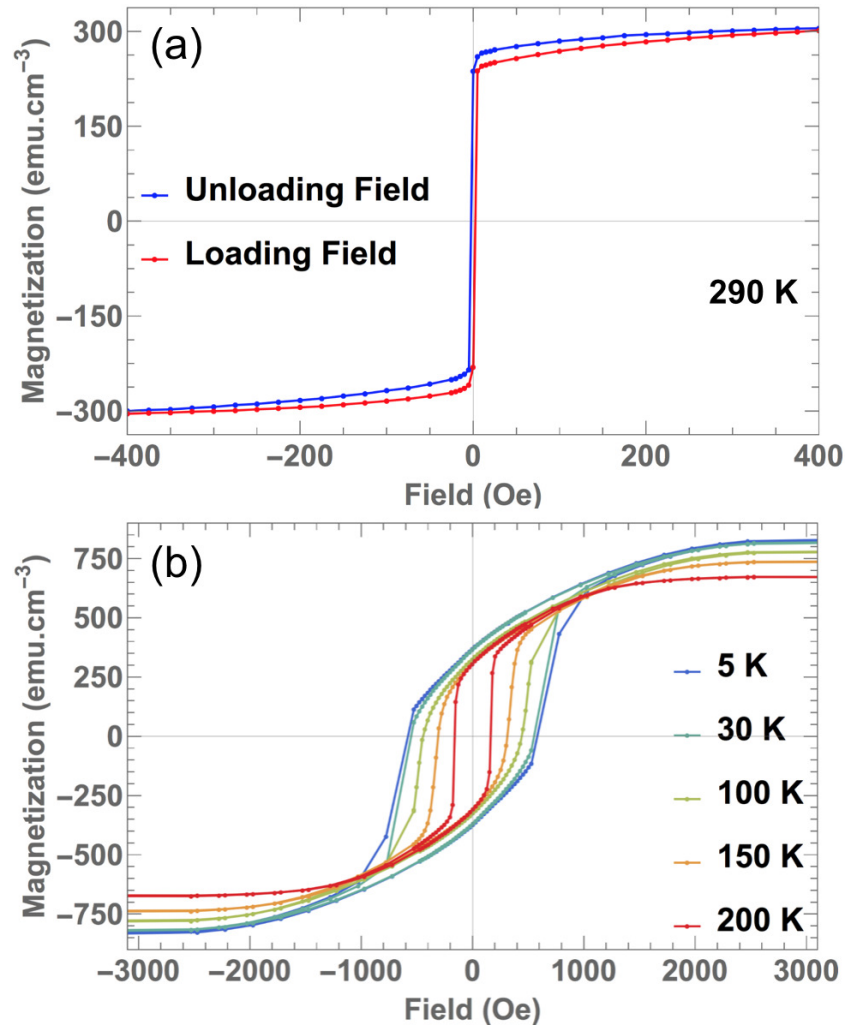


Figure 5-2: Hysteresis curves measured at temperatures (a) close to the Curie temperature and (b) from 5 K to 200 K. In the vicinity of the Curie point, the coercivity is low and the remanence ratio is high, while it is the opposite for lower temperatures.

temperature and increase before reaching the maximum and finally decrease again once the maximum is passed, due to the transition to the paramagnetic phase. This behavior is related to the increase of magnetic domain wall mobility at low magnetic field upon heating, thus leading to an increase in the ZFC magnetization activated by a thermal process. The results in Fig. 5-3 indicate that the interactions between spins becomes non-homogenous below a certain temperature depending on the applied field. Moreover, one can notice a kink in the magnetization at about 65 K for each FC curve (marked by an arrow in Fig. 5-3 only for the curve at 800 Oe). The position of this sudden increase in magnetization for decreasing temperature seems not to be field dependent, although the effect gets weaker at higher fields. Its physical meaning will be discussed later. The thermal irreversibility in the ZFC and FC magnetizations shows that the ferromagnetic order in epitaxial Mn_5Ge_3 on $\text{Ge}(111)$ is affected by some glassy behavior [24].

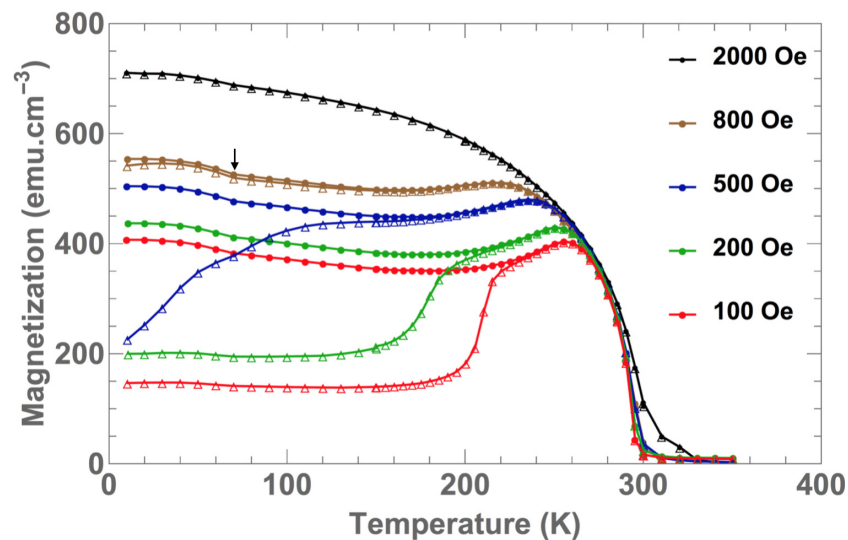


Figure 5-3: ZFC and FC curves for different values of dc magnetic field, open symbols are for ZFC curves, and full symbols are for FC curves. Notice the presence of a kink (marked by the arrows for the curve at 800 Oe) at about 65 K for each ZFC and FC curves.

The thermoremanent magnetization (TRM) is measured by cooling down from the paramagnetic state to a measurement temperature T_m , in the field cooling condition under a field of 800 Oe. When T_m is reached, the applied dc field is turned off and the magnetization is measured as a function of time. In the present case, $T_m = 100$ and 270 K. The reference time corresponds to the time at which the magnetic field is removed. The decay of the thermoremanent magnetization is best fitted with a logarithm function for the laboratory timescale, as seen in Fig. 5-4, by using the following relation:

$$M(t) = M_0 - S_{\text{RM}} \ln(t), \quad (5.1)$$

where M_0 is a constant and S_{RM} is the temperature-dependent magnetic viscosity [25].

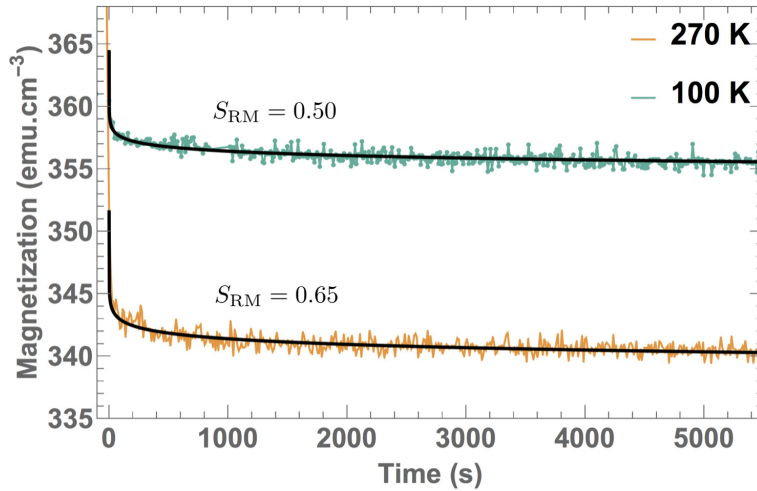


Figure 5-4: Time dependence of the TRM at 100 K and 270 K. The black lines are fits using the logarithm law given in Eq. (5.1).

Although used in some spin-glass systems [26, 27, 28, 29], a stretched exponential function does not give any satisfactory fits in this case. The magnetic viscosity in the time dependence of the magnetization shown in Fig. 5-4, corresponds to a lag between the changes in magnetization in response to the changes in the applied field. It occurs

when energy barriers need to be overcome for the magnetization to decrease when the field is removed. Such slow decay of the TRM is consistent with a spin-glass-like behavior, for which the energy barriers are uniformly distributed [29, 30, 31, 32].

5.3.2 Analysis of the ac susceptibility in Mn_5Ge_3

The ac susceptibility of the Mn_5Ge_3 thin films is measured by applying a driving field $H(t) = H_{\text{ac}} \cos(\omega t)$, where H_{ac} and $\omega/2\pi$ are the driving amplitude and driving frequency, respectively. Measurements of the real part (χ') and imaginary part (χ'') of the susceptibility are performed both without and with a bias dc field, in the zero-field cooling condition. The measurement at zero dc field in Fig. 5-5(a) clearly shows a divergent peak in the real susceptibility at about 294 K. This temperature is consistent with the Curie point, therefore the peak matches with the paramagnetic (PM) to ferromagnetic (FM) transition. In addition to the sharp and intense peak at 294 K, a broad peak with less intensity, whose maximum is located at about 275 K, is also observed. The presence of a maximum in the imaginary part at a temperature slightly lower than that of the real part is a sign of a relaxation process. Interestingly, one can notice that the imaginary part of the ac susceptibility at zero dc field is of the same order of magnitude as the real part, and bigger in absolute value. To our best knowledge, no previous work reported that the contribution of the out-of-phase term could be higher than that of the in-phase term, for a certain range of temperature. The imaginary part represents magnetic losses or irreversible process induced by an energy absorption from the ac magnetic field. In the present case, some unusual energy dissipation may occur at the irreversibility point. In the Mn_5Ge_3 thin film, both real and imaginary parts are sensitive to the presence of a superimposed dc field, even as small as 2 Oe [see Fig. 5-5(b)]. Due to the bias dc field, the intensity

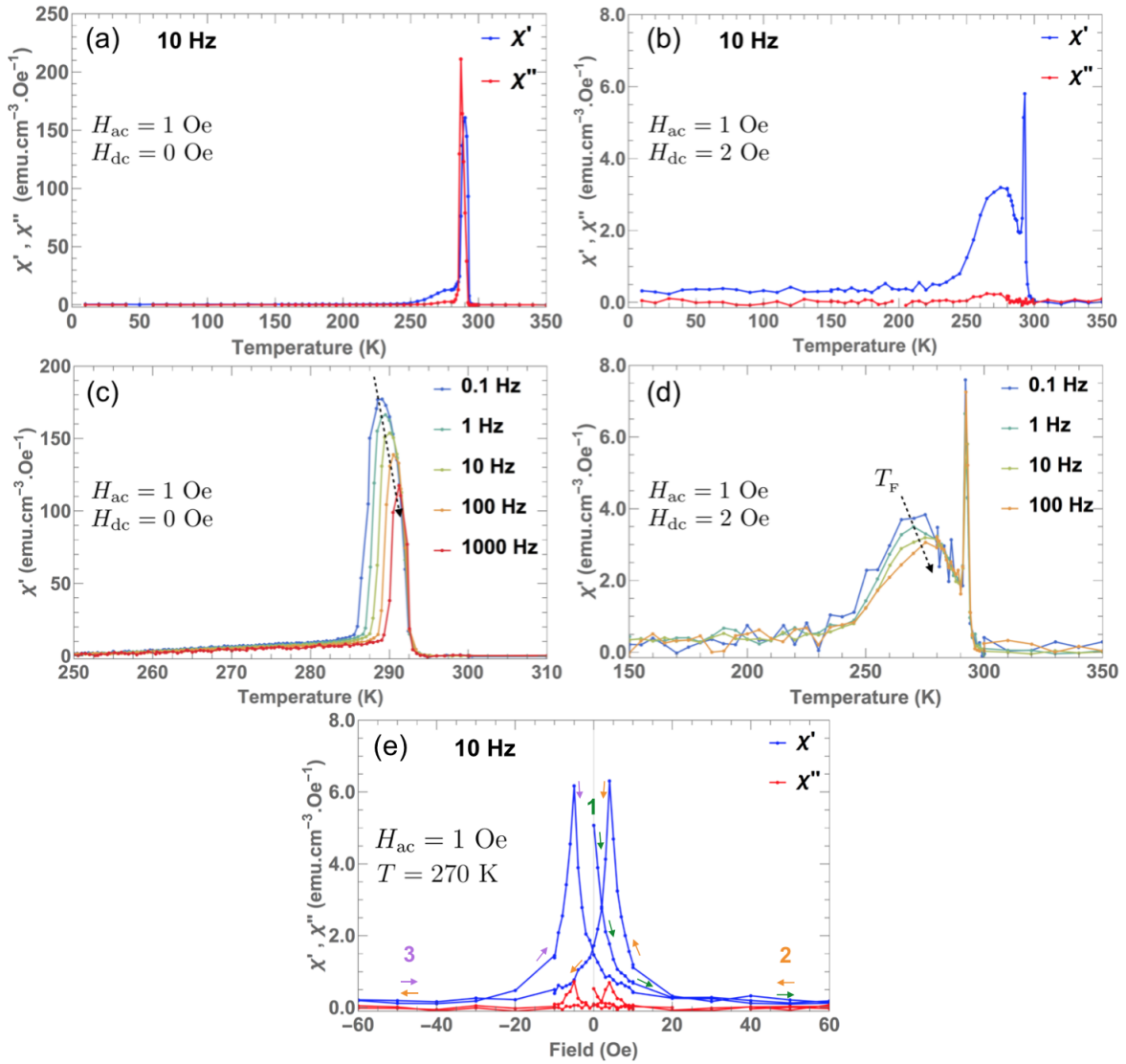


Figure 5-5: ac susceptibility measurements performed using a driving field of 1 Oe with no dc field [(a) and (c)] and with superimposed dc field of 2 Oe [(b) and (d)]. A driving frequency of 10 Hz was used in (a) and (b), for which both real and imaginary parts are shown. The frequency dependence of the real part χ' is shown with (c) zero dc field and (d) with a dc field of 2 Oe, in a temperature range close to the Curie point. The spin-freezing temperature shifting with higher frequency is indicated by a dashed arrow. The dependence of the ac susceptibility on the dc static field is measured (e) at 270 K in three steps: 1) initial step, 2) hysteresis loop for unloading field, and 3) hysteresis loop for loading field.

of the peak of the PM to FM transition substantially decreases, and what was seen as a small broad peak in Fig. 5-5(a) appears as a distinct feature in Fig. 5-5(b). The imaginary susceptibility in Fig. 5-5(b) is severely reduced to be one order of magnitude smaller than the real component. The maximum of the secondary peak of the real susceptibility is slightly shifted to a lower temperature (~ 265 K) in the presence of the static field. This observation is consistent with the fact that the irreversibility temperature decreases with increasing field (see Fig. 5-3). In Figs. 5-5(c) and 5-5(d), it is evidenced that the ac susceptibility is dependent on the frequency of the driving field, which is a sign of a slowing down in the magnetization dynamics. In the data in Fig. 5-5(d), one can notice that the peak at 294 K is independent on frequency, which is expected for a transition to a long-range-ordered phase, such as the PM to FM transition, while the other peak is frequency dependent. The maximum of the secondary peak shifts towards higher temperatures with increasing frequencies, which is a common feature seen in spin glasses [33]. In summary, the results in Fig. 5-5 suggest that when the Mn_5Ge_3 thin film is cooled down from above room temperature, it undergoes a PM to FM transition at 294 K. Further decrease in temperature leads to a slow magnetization dynamics occurring in the immediate vicinity of T_c at low fields. The scaling laws are employed in order to quantify the frequency dependence of the spin-glass transition temperature T_F . Here, the freezing temperature shift (δT_F) per decade of frequency is given by

$$\delta T_F = \frac{\Delta T_F}{T_F \Delta[\log(\omega/2\pi)]}. \quad (5.2)$$

From the results in Fig. 5-5(d), we estimate $\delta T_F \simeq 0.005$. Previous reports state that δT_F usually ranges from 0.0045 to 0.06 for canonical spin glasses (e.g. CuMn),

and $\delta T_F \geq 0.1$ for systems with noninteracting clusters, such as superparamagnets [33, 34, 35, 36, 37]. Consequently, the value of δT_F for our system is of the same order of magnitude as that of a canonical spin glass.

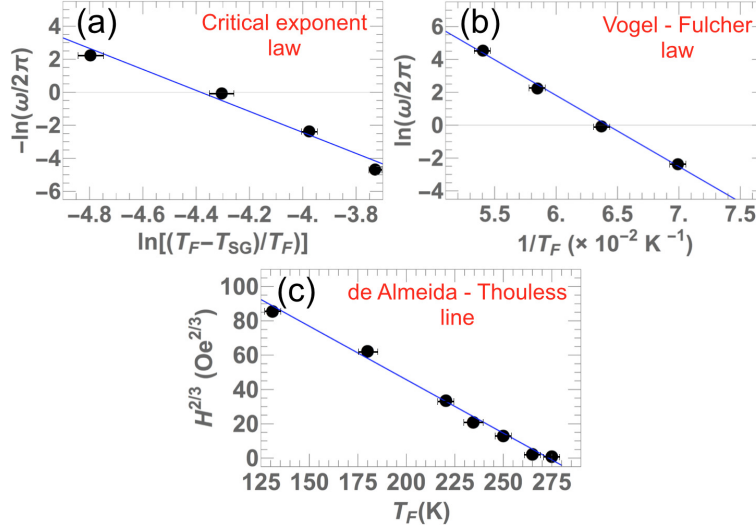


Figure 5-6: (a) Log-log plot of the critical exponent law for the frequency dependence of the freezing temperature, (b) Vogel-Fulcher law, both fitted by using the data in Fig. 5-5(d). (c) $H^{2/3}$ as a function of T_F . The irreversibility temperatures are obtained from the ZFC and FC curves, by calculating the difference between the FC and ZFC magnetizations and determining the onset of non-zero difference.

The hypothesis of a spin-glass-like behavior in our system is further supported by the fit of the frequency dependence of the susceptibility maxima, using the critical exponent law:

$$\tau = \tau_0^{\text{crit}} \left(\frac{T_F - T_{\text{SG}}}{T_F} \right)^{-z\nu}, \quad (5.3)$$

where $1/\tau = \omega/2\pi$ is the driving frequency, τ_0^{crit} is the characteristic relaxation time for a single spin-flip, T_{SG} is the spin-glass transition temperature at zero frequency, and $z\nu$ is the dynamical exponent. Figure 5-6(a) shows a log-log plot corresponding to Eq. (5.3), the best fit is obtained with $z\nu \simeq 6.5$, $1/\tau_0^{\text{crit}} \simeq 1.1 \times 10^{12}$ Hz, and $T_{\text{SG}} = 266.5$ K. The value of $z\nu$ in the present case is included in the typical range

of values found for spin glasses (between 4 and 12) [35, 36, 38], and the value of $1/\tau_0^{\text{crit}}$ is close to the highest values of characteristic frequency reported for spin glasses ($10^8 \leq 1/\tau_0^{\text{crit}} \leq 10^{12}$ Hz) [35, 38, 39]. The Arrhenius law for the frequency dependence of the ac susceptibility maximum $1/\tau = 1/\tau_0 \exp(-E_a/k_B T_F)$, which accounts for the time scale to overcome energy barriers by an activation process, is not adapted to describe the frequency dependence of the freezing temperature in our sample because it results in the unphysical values of $1/\tau_0 \sim 10^{193}$ Hz and the activation energy term $E_a/k_B = 1.2 \times 10^5$ K. E_a and k_B are the activation energy and the Boltzmann constant, respectively. This invalidity of the Arrhenius law is consistent with the fact that the epitaxial Mn₅Ge₃ thin film does not contain any noninteracting magnetic clusters [34]. In order to take into account the fact that the spins in the glassy state are interacting with each other and get an estimation of the activation energy, we use the phenomenological Vogel-Fulcher law:

$$\frac{1}{\tau} = \frac{1}{\tau_0} \exp \left[\frac{-E_a}{k_B (T_F - T_0)} \right], \quad (5.4)$$

where τ_0 has the same physical meaning as τ_0^{crit} , and T_0 is the empirical Vogel-Fulcher temperature, often interpreted as being related to the strength of the exchange interaction in the material [35, 40, 41, 42]. The best fit, shown in Fig. 5-6(b), is obtained with $1/\tau_0 \simeq 1.2 \times 10^{12}$ Hz, which is consistent with the value found by the critical exponent law [Eq.(5.3)] and an activation energy of $E_a/k_B \simeq 433.2$ K, which is a relatively high value compared to other spin-glass systems. The Vogel-Fulcher temperature is determined to be $T_0 \simeq 254.3$ K. The relatively high value of the Vogel-Fulcher temperature suggests that the exchange interaction in the glassy state in the Mn₅Ge₃/Ge(111) heterostructure is stronger than that of the spin glasses reported in

the literature, for which T_0 is usually below 100 K [33, 34, 37]. A relationship between the Vogel-Fulcher and the critical exponent laws was established in [39], and one can find the dynamical exponent using the activation energy:

$$\ln \left(\frac{40k_{\text{B}}T_{\text{F}}}{E_a} \right) \sim \frac{25}{z\nu}. \quad (5.5)$$

This relation gives $z\nu \simeq 7$, which is close to 6.5 obtained directly by the critical exponent law. As a result, both scaling laws are consistent with each other.

The dependence of the onset of irreversibility on the applied dc field is calculated using the onset of nonzero difference between the FC and ZFC magnetizations. The ac susceptibility vanishes at fields as small as a few Oe [step 1) in Fig. 5-5 (e)], thus making it difficult to probe the properties at higher fields. For Ising spin glasses, the mean-field theory predicts the existence of a transition line in the H - T plane, called the de Almeida-Thouless (AT) line [43, 44, 45, 46]. The AT relation is derived from the Sherrington-Kirkpatrick theory for the free energy of a spin glass [47]. The field dependence of the onset of irreversibility [47, 48, 8] can be analytically written as:

$$\frac{H_{\text{AT}}}{\Delta J} \propto \left[1 - \frac{T_{\text{F}}}{T_{\text{F}}(H=0)} \right]^{3/2}, \quad (5.6)$$

where ΔJ is the width of distribution of exchange energy interaction and $T_{\text{F}}(H=0)$ is the freezing temperature at zero field. A reasonable fit with the theoretical AT line is found for this system and gives a zero-field freezing temperature $T_{\text{F}}(H=0) \simeq 275$ K, as can be seen in Fig. 5-6(c). A magnetic phase diagram in the H - T plane for the spin-glass-like state characterized above is suggested in Fig. 5-7. The AT line normally represents the transition from an ergodic phase to a nonergodic phase, with no change in symmetry [44, 45, 46]. Therefore, the AT line separates a spin-glass phase

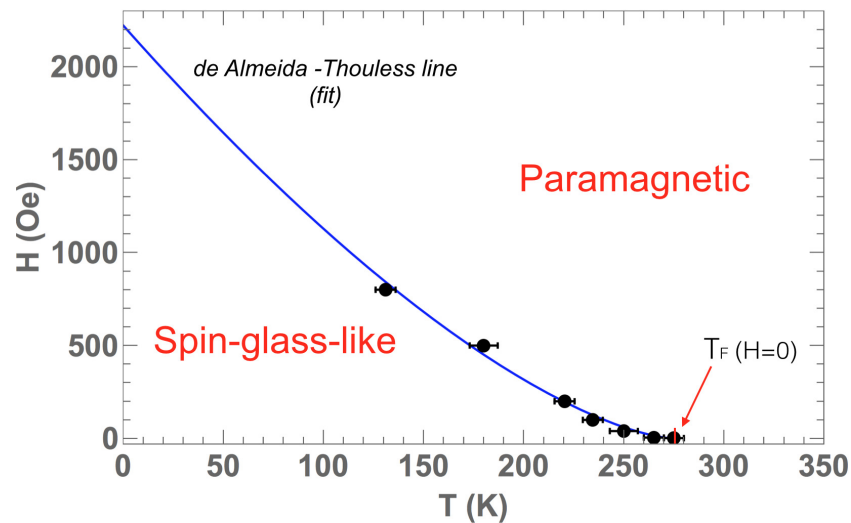


Figure 5-7: The irreversible behavior is characterized by a H - T magnetic phase diagram showing an AT line, which separates the spin-glass-like state from the paramagnetic phase. The AT line is determined experimentally (black dots) using the data from the ZFC and FC measurements and calculated (blue line) using a zero-field freezing temperature of 275 K and a zero-temperature critical field of 2220 Oe in Eq.(5.6).

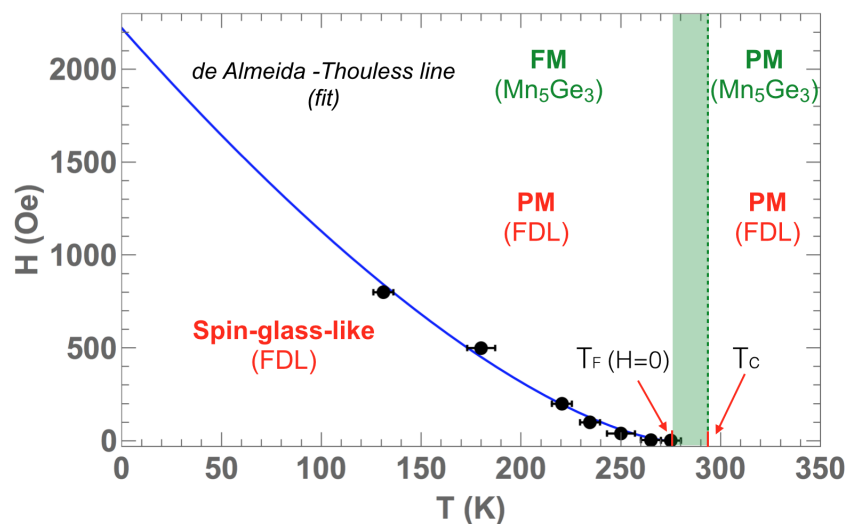


Figure 5-8: The stability domain of the spin-glass-like state shares a common interval of temperature and field with the stability domain of the ferromagnetic state of Mn_5Ge_3 . The slow magnetization dynamics of the sample happens due to the coupling between spin-glass region (FDL) and the ferromagnetic region. In the green region of the diagram, the material behaves as a pure ferromagnet.

(nonergodic) from a paramagnetic phase (ergodic). We find a relatively good match between the theoretical fit of the de Almeida-Thouless line and the results obtained by experiments. One can see that for almost the entire the range of temperature from 0 K to T_C , the FM order of Mn_5Ge_3 overlaps with the stability domain of the spin-glass-like state, provided the magnetic field is low enough. The Curie temperature is barely 20 K above the zero-field spin-glass transition temperature. This means that there is a small range of temperature (between 275 and 294 K), for which the system behaves as a pure ferromagnet, as shown in Fig. 5-8. This fact explains why in the vicinity of the Curie temperature, the magnetization hysteresis curve [see Fig. 5-2(a)] has a high remanence ratio, due to the high intrinsic in-plane anisotropy of the ferromagnetic phase in the thin film, and below a certain temperature, which is $T_F(H = 0) \simeq 275$ K, the hysteresis has a weaker remanence ratio [see Fig. 5-2(b)] due to the influence of a spin-glass-like state. In Fig. 5-5(e), one can see that the coercive field at 270 K is small and comparable to the values close to T_C , despite the entry in the spin-glass phase. The influence of the spin-glass state on the ferromagnetic phase may not occur immediately below the glass transition, due to the thermal energy at 270 K, which weakens the frustrated interactions between the spin glass and the ferromagnet.

The previous results are actually not sufficient to claim that the Mn_5Ge_3 thin film undergoes a true spin-glass phase transition. It can only be claimed that the behavior under the AT line is spin-glass-like. In order to determine whether an actual spin-glass phase transition takes place or not, it is necessary to measure the nonlinear susceptibility of the sample. Unfortunately, the magnitude of the linear susceptibility is already quite small, and because of the fact that the nonlinear contribution is at least one order of magnitude smaller, the non-linear susceptibility measurement is difficult in the present case.

5.3.3 Possible origin of the spin-glass-like behavior

Since the coexistence of the frustration and randomness is required for the spin-glass behavior, observation of the magnetic irreversibility in the single crystalline, i. e., ordered Mn_5Ge_3 is somewhat puzzling. However, as mentioned earlier, Mn_5Ge_3 on $\text{Ge}(111)$ has a “ferromagnetically dead” layer at the $\text{Mn}_5\text{Ge}_3/\text{Ge}$ interface [16]. Therefore it is possible that this “dead layer”, resulting most likely from the intermixing between the ferromagnetic Mn_5Ge_3 and Ge and from the lattice mismatch between the two materials, can possess the disorder needed for the spin-glass-like behavior, especially since there has been a previous report that disordered Mn-Ge compounds could demonstrate the spin-glass behavior [49]. Thus the hypothesis here is that the system is actually made of two magnetic layers, one of which is ferromagnetic and the other is spin glass. The overall glassy behavior of the sample is due to the interaction between the ferromagnetic Mn_5Ge_3 with the thin spin-glass-like region. By using samples grown in the same conditions as samples A and C with different thicknesses, we estimated the thickness of the “ferromagnetically dead” layer to be 1.9 ± 0.2 nm. The presence of the sudden increase in magnetization at 65 K for decreasing temperature in Fig. 5-3 can be seen as the consequence of the exchange coupling at the interface between the spin-glass region and the FM phase. The kink in the FC magnetization happens at a temperature that is relatively low compared to the zero-field spin-glass-like transition temperature. In previous reports, a noticeable feature of many metallic spin-glasses (such as CuMn , AgMn , AuFe , Ni-Mn alloys) was the occurrence of unidirectional anisotropy [50, 51, 52, 53, 54, 55] for $T \ll T_F$ (typically $T < T_F/3$, see Ref.[50]). In our case, the presence of a low temperature unidirectional anisotropy can create an additional easy axis in the FM phase along the applied field during the FC process, thus increasing the magnetization below a certain temperature. A

widely used criterion for evaluating the presence of a unidirectional anisotropy is the presence of an exchange bias field. However, in our case the spin-glass region may be too small to induce a measurable exchange bias field in the FM region. Such a low temperature kink in the FC magnetization has also been observed below the spin-glass transition temperature in ferromagnetic systems that share interfaces with spin-glasses, such as $\gamma\text{-Fe}_2\text{O}_3$, $\text{La}_{2/3}\text{Sr}_{1/3}\text{MnO}_3$ and $\text{La}_{0.7}\text{Ca}_{0.3}\text{MnO}_3$, and the behavior was attributed to the effect of spin-glass interfaces [6, 8, 9, 59]. In Refs.[6, 8, 9], the magnetization kink was also the onset of exchange bias. In addition, temperature-dependent magnetization curves measured at fields as high as 10^4 Oe have no kink at 65 K. The kink in the FC magnetization is visible only below the AT line, which confirms its relationship to the spin-glass-like state.

The irreversible behavior of the thermal magnetization in the $\text{Mn}_5\text{Ge}_3/\text{Ge}(111)$ heterostructure can be explained as follows. Under the ZFC condition, the directions of the spins in the spin-glass region are randomly oriented and thus the spins in the spin-glass region are randomly coupled with the spins of the FM region near the interface. Such random coupling makes the motion of the domain walls unfavorable. As a result, for decreasing temperature the ZFC magnetization becomes small [Fig. 5-3] and the coercive field becomes large [Fig. 5-2(b)]. Under the FC condition, the directions of the spins in the spin-glass region tend to align more with the external field, so the randomness in the magnetic coupling between the FM and the spin-glass regions is diminished. Consequently, the magnetic domains move more easily, allowing the FC magnetization to become large. However, the coercivity remains large because the directions of the spins in the spin-glass region are still random, even under the FC condition.

Since the scaling laws showed that the spin-glass-like region at the $\text{Mn}_5\text{Ge}_3/\text{Ge}$

interface behaves like a canonical spin glass, it is reasonable to assume that this region is made of Mn atoms embedded in a Ge-rich phase, thus making a case comparable to the above-mentioned spin glasses. Considering that the interactions between Mn atoms in the spin-glass region are mediated by conduction electrons, the Ruderman-Kittel-Kasuya-Yoshida (RKKY) model [51, 52, 56, 57] allows to evaluate the freezing temperature as follows $T_F \sim V_0 S^2 d^{-3}$ [56], where V_0 is the RKKY coupling constant, S is the spin of Mn, and d is the average distance between Mn atoms. Consequently, the high spin-glass transition temperature in our system can be interpreted as the fact that the average distance between Mn atoms in the spin-glass region is relatively small. Therefore, this picture suggests that the spin-glass-like behavior is induced by an inhomogeneous composition for the “dead” layer.

According to the previous description of the nature of the spin-glass layer, it would be natural to consider that its properties are dependent on the thin film growth conditions. The magnetic properties of samples B and C (described in Table 5.1) are discussed in the following section. Although the structural characterizations of samples B and C give the same results as those for sample A, the annealing temperature employed for the solid phase epitaxy and the film thickness have an influence on the thermal irreversibility of the magnetization in Mn_5Ge_3 on $\text{Ge}(111)$.

5.4 Influence of the growth conditions on the spin-glass-like behavior

5.4.1 Influence of the solid phase epitaxy temperature

Sample B was fabricated using a higher annealing temperature than that for sample A. The ZFC and FC magnetizations of sample B [Fig. 5-9(a)] are substantially different from the ones shown for sample A in Fig. 5-3. The temperature dependence of the real part of the susceptibility [Fig. 5-9(b)] has distinct features from the case of sample A; the Curie point is lower than that of sample A by four degrees ($T_C \simeq 290$ K).

From the ZFC and FC curves, one can see that the onset of irreversibility, marked by T_{irr} , occurs at a temperature higher than the Curie point. This is a consequence of the higher growth temperature, which broadens the spin-glass transition temperature region, as evidenced by the observation of a frequency dependence of the real part of the susceptibility both below and above T_C in Fig. 5-9(b). Thus, a small portion of the spin-glass region has a transition temperature at around T_{irr} but a large portion of the spin-glass region has its transition at around T_F . As for sample A, the difference between the ZFC and FC magnetizations is due to the interaction between the spin-glass region and the FM region. The weak irreversibility just below T_{irr} in the ZFC and FC curves may be attributed to the sole contribution of the spin-glass region, which has a smaller size compared to the overall size of the sample. The difference between the FC and ZFC magnetizations becomes significant when Mn_5Ge_3 enters the FM phase. From the data in Fig. 5-9(b), we obtain $\delta T_F \simeq 0.005$, which is in agreement with sample A. As for sample A, the low temperature kink in the FC magnetization is visible in sample B, accounting for the same effect discussed above.

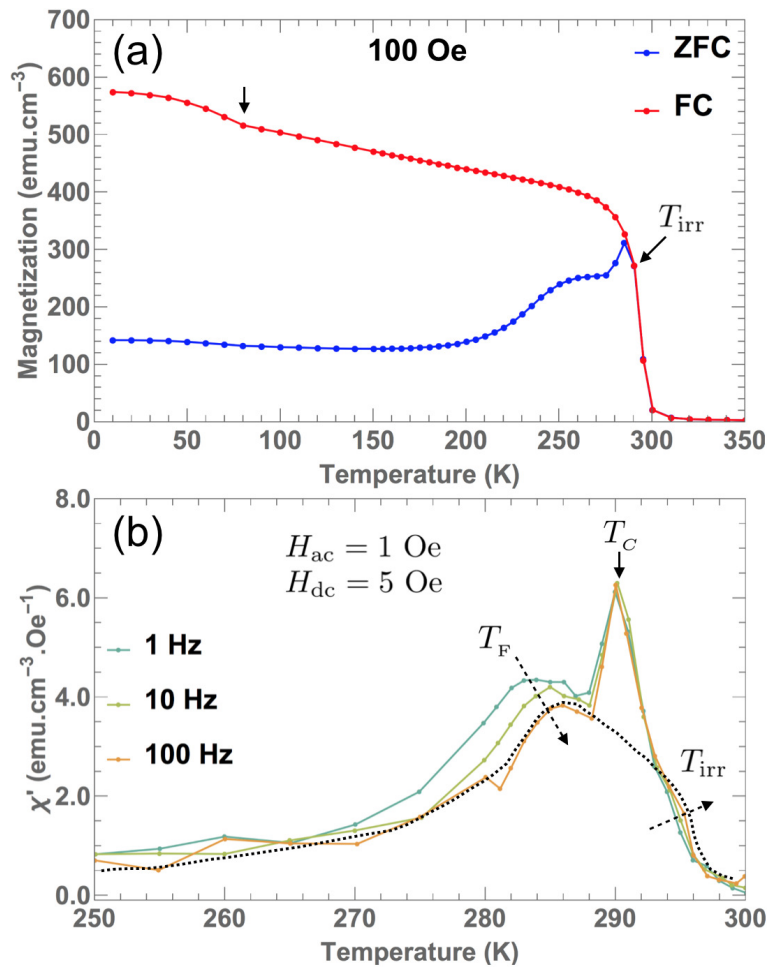


Figure 5-9: (Color online) (a) ZFC and FC curves measured at a dc field of 100 Oe for sample B. (b) Frequency dependence of the in-phase component of the ac susceptibility, using a driving amplitude of 1 Oe and a bias dc field of 5 Oe. The Curie point is about 290 K and the peak corresponding to the irreversible behavior seems to overlap with the frequency-independent peak, as suggested by the eye-guiding dashed curve in (b). The sudden increase in FC magnetization is marked by an arrow at 80 K.

However, the onset of the kink in sample B is at about 80 K, which is higher than that of sample A.

5.4.2 Influence of the thickness

Sample C is grown in the same conditions as sample A but its thickness is larger. Similar to sample B, the spin-glass region in sample C shows the transition from PM to spin glass above the Curie temperature of the FM phase [see Fig. 5-10(a)]. This is confirmed by the relative positions of the two maxima in the real part of the susceptibility [Fig. 5-10(b)], from which we estimate $T_C \simeq 288\text{K}$ and $T_{\text{irr}} = 295\text{K}$. The position of the maximum of χ'' shows that the most visible relaxation process occurs just below T_C , while no maximum of comparable magnitude is present in the vicinity of T_{irr} . So, the main relaxation process occurs in the FM state. This behavior is similar to that of sample B. A sudden increase of FC magnetization is observed at 80 K as well. The main feature of sample C is the larger difference between the FC and ZFC magnetizations at low temperature, compared to the case of sample A. This is due to the fact that the ferromagnetic volume in sample C is larger than that in sample A, but the spin-glass volume around the interface is kept the same in both cases.

Despite demonstrating the quantitative variation in the magnetic properties depending on the growth conditions, samples A, B and C share common traits, which are the presence of the slow magnetization relaxation close to the Curie point, and the low temperature kink in the FC magnetization. The susceptibility measurements for samples B and C imply that the spin-glass region alone is too small to induce a visible maximum in χ'' , however for decreasing temperature, a clear slow magnetization dynamics is obtained when the FM state is reached, thus evidencing the interaction

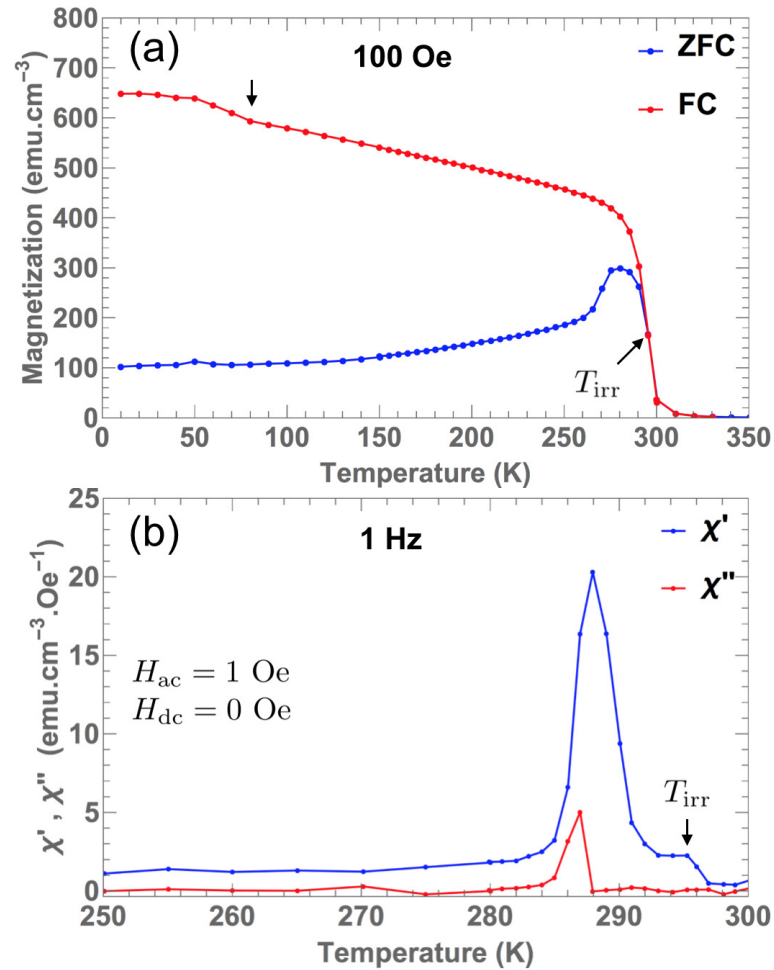


Figure 5-10: (Color online) (a) ZFC and FC curves measured at a dc field of 100 Oe for sample C. (b) Real and imaginary parts of the ac susceptibility measured without bias dc field. The Curie point is about 288 K, which is slightly lower than that of sample B. The irreversibility temperature is higher than the Curie point $T_{\text{irr}} \simeq 295$ K. The sudden increase in FC magnetization is marked by an arrow at 80 K.

between the two regions. In sample A, since the spin-glass transition occurs below the Curie point, the slow dynamics is obtained at the transition point, i.e. T_{irr} and T_{F} are identical for sample A. The origin of the spin-glass-like behavior itself is extrinsic to the ferromagnetic Mn_5Ge_3 thin film. However, the spin-glass-like nature of the interface layer significantly affects the temperature-dependent behavior of the magnetization of the $\text{Mn}_5\text{Ge}_3/\text{Ge}(111)$ heterostructure. It was reported in previous literatures [60, 16, 61] that the remanence ratio decreased with increasing thickness for both in-plane and perpendicular magnetizations. Since the easy axis of the bulk material is along the hexagonal c axis, one would expect larger perpendicular remanences for larger thicknesses of thin films. The interfacial glassy behavior shown in the present work is very likely to explain the great differences between the bulk material and Mn_5Ge_3 films on Ge(111) at higher thicknesses.

5.5 Summary

To summarize this chapter, Mn_5Ge_3 epitaxial thin films on $\text{Ge}(111)$ do not show a simple ferromagnetic ordering contrary to the bulk Mn_5Ge_3 . Films grown at $150\text{ }^\circ\text{C}$ via solid phase epitaxy undergo a transition to a spin-blocked state, for which the transition temperature at zero field is relatively close to the Curie point. The analysis of the ac susceptibility indicates that the spin-blocked state is spin-glass-like. Such transition to the glassy state explains the very different shapes of the magnetization cycles in the vicinity of T_C from the ones at low temperature. This spin-glass-like behavior is attributed to the presence of a “ferromagnetically dead layer” or more directly the spin-glass-like layer at the $\text{Mn}_5\text{Ge}_3/\text{Ge}$ interface that is formed during the solid phase epitaxy process. Thus the Mn_5Ge_3 film is separated into two layers, one of which is ferromagnetic. The spin-glass-like nature attributed to the interface-side layer explains the presence of the thermal irreversibility in the magnetization due to the frustrated interactions with the ferromagnetic Mn_5Ge_3 . The spin-glass-like nature for the “ferromagnetically dead layer” is supported by the scaling laws. The fact that the magnetization irreversibility in Mn_5Ge_3 thin films is affected by the growth temperature and the thickness of the FM region, while the structure of the Mn_5Ge_3 layer remains the same, supports the hypothesis on a variation of magnetic properties due to the $\text{Mn}_5\text{Ge}_3/\text{Ge}$ interface rather than the FM region. At higher growth temperature ($200\text{ }^\circ\text{C}$), the Curie point becomes slightly lower and the irreversibility occurs above T_C . For a larger thickness (33 nm), the irreversibility also occurs above T_C , but the FC and ZFC magnetizations show the larger difference at low temperatures. Despite the FM behavior at high temperature and the glassy state at low temperature, the system is much different from a reentrant spin-glass because of the extrinsic character of the spin-glass state.

Bibliography

- [1] J. S. Kouvel, *J. Phys. Chem. Solids* **21**, 57 (1961). [Cited on page(s) 105.]
- [2] M. Ali, P. Adie, C. H. Marrows, D. Greig, B. J. Hickey, and R. L. Stamps, *Nature Mater.* **6**, 70 (2007). [Cited on page(s) 105.]
- [3] F. T. Yuan, J. K. Lin, Y. D. Yao, and S. -F. Lee, *Appl. Phys. Lett.* **96**, 162502 (2010). [Cited on page(s) 105.]
- [4] R. Iguchi, K. Ando, E. Saitoh, T. Sato, *J. Phys.: Conf. Ser.* **266**, 012089 (2011). [Cited on page(s) 105.]
- [5] J. F. Ding, O. I. Lebedev, S. Turner, Y. F. Tian, W. J. Hu, J. W. Seo, C. Panagopoulos, W. Prellier, G. Van Tendeloo, and T. Wu, *Phys. Rev. B* **87**, 054428 (2013). [Cited on page(s) 105.]
- [6] T. Zhu, B. G. Shen, J. R. Sun, H. W. Zhao, and W. S. Zhan, *Appl. Phys. Lett.* **78**, 3863 (2001). [Cited on page(s) 3, 105, and 122.]
- [7] R. H. Kodama, A. E. Berkowitz, E. J. McNiff, Jr., and S. Foner, *Phys. Rev. Lett.* **77**, 394 (1996). [Cited on page(s) 105.]
- [8] B. Martínez, X. Obradors, Ll. Balcells, A. Rouanet, and C. Monty, *Phys. Rev. Lett.* **80**, 181 (1998). [Cited on page(s) 3, 105, 118, and 122.]
- [9] S. B. Xi, W. J. Lu, H. Y. Wu, P. Tong, and Y. P. Sun, *J. Appl. Phys.* **112**, 123903 (2012). [Cited on page(s) 3, 105, and 122.]
- [10] C. Zeng, S. C. Erwin, L. C. Feldman, A. P. Li, R. Jin, Y. Song, J. R. Thompson and H. H. Weitering, *Appl. Phys. Lett.* **83**, 5002 (2003). [Cited on page(s) 6, 29, and 105.]
- [11] C. Zeng, W. Zhu, S. C. Erwin, Z. Zhang, and H. H. Weitering, *Phys. Rev. B* **70**, 205340 (2004). [Cited on page(s) 6 and 105.]
- [12] L. Sangaletti, D. Ghidoni, S. Pagliara, A. Goldoni, A. Morgante, L. Floreano, A. Cossaro, M. C. Mozzati, and C. B. Azzoni, *Phys. Rev. B* **72**, 035434 (2005). [Cited on page(s) 6 and 105.]
- [13] L. Sangaletti, E. Magnano, F. Bondino, C. Cepek, A. Sepe, and A. Goldoni, *Phys. Rev. B* **75**, 153311 (2007). [Cited on page(s) 6 and 105.]
- [14] S. Olive-Mendez, A. Spiesser, L. A. Michez, V. Le Thanh, A. Glachant, J. Derrien, T. Devillers, A. Barski, and M. Jamet, *Thin Solid Films* **517**, 191 (2008). [Cited on page(s) 105.]

- [15] J. Hirvonen Grytzeli, H. M. Zhang, and L. S. O. Johansson, *Phys. Rev. B* **86**, 125313 (2012). [Cited on page(s) 6 and 105.]
- [16] A. Spiesser, F. Viro, L. A. Michez, R. Hayn, S. Bertaina, L. Favre, M. Petit, and V. Le Thanh, *Phys. Rev. B* **86**, 035211 (2012). [Cited on page(s) 106, 121, and 128.]
- [17] S. Picozzi, A. Continenza, and A. J. Freeman, *Phys. Rev. B* **70**, 235205 (2004). [Cited on page(s) 106.]
- [18] P. De Padova, J. M. Mariot, L. Favre, I. Berbezier, B. Olivieri, P. Perfetti, C. Quaresima, C. Ottaviani, A. Taleb-Ibrahimi, P. Le Fèvre, F. Bertran, O. Heckmann, M. C. Richter, W. Ndiaye, F. D’Orazio, F. Lucari, C. M. Cacho, K. Hricovini, *Surf. Sci.* **605**, 638 (2011). [Cited on page(s) 6 and 107.]
- [19] A. Truong, A. O. Watanabe, T. Sekiguchi, P. A. Mortemousque, T. Sato, K. Ando, and K. M. Itoh, *Phys. Rev. B* **90**, 224415 (2014). [Cited on page(s) 39, 81, and 109.]
- [20] E. Callen, Y. J. Liu, and J. R. Cullen, *Phys. Rev. B* **16**, 263 (1977). [Cited on page(s) 109.]
- [21] S. Chikazumi, *Physics of Magnetism* (Wiley, New York, 1964), p. 247. [Cited on page(s) 109.]
- [22] I. Maartense, and G. Williams, *J. Phys. F: Met. Phys.* **6**, L121 (1976). [Cited on page(s) 109.]
- [23] F. H. Salas, M. Maribal-García, *Phys. Rev. B* **41**, 10859 (1990). [Cited on page(s) 109.]
- [24] A. Truong, A. O. Watanabe, P. A. Mortemousque, K. Ando, T. Sato, T. Taniyama, and K. M. Itoh, *Phys. Rev. B* **91** 214425 (2015). [Cited on page(s) 6, 96, and 111.]
- [25] K. Binder and A. P. Young, *Rev. Mod. Phys.* **58**, 801 (1986). [Cited on page(s) 74 and 112.]
- [26] P. Nordblad, P. Svedlindh, L. Lundgren, and L. Sandlund, *Phys. Rev. B* **33**, 645(R) (1986). [Cited on page(s) 112.]
- [27] M. A. Continentino, A. P. Malozemoff, *Phys. Rev. B* **33**, 3591(R) (1986). [Cited on page(s) 112.]
- [28] R. V. Chamberlin, G. Mozurkewich, and R. Orbach, *Phys. Rev. Lett.* **52**, 867 (1984). [Cited on page(s) 74 and 112.]

- [29] S. D. Tiwari, and K. P. Rajeev, Phys. Rev. B **72**, 104433 (2005). [Cited on page(s) 112 and 113.]
- [30] D. X. Li, S. Nimori, Y. Shiokawa, Y. Haga, E. Yamamoto, and Y. Onuki, Phys. Rev. B **68**, 012413 (2003). [Cited on page(s) 113.]
- [31] D. X. Li, S. Nimori, Y. Shiokawa, Y. Haga, E. Yamamoto, and Y. Onuki, Phys. Rev. B **68**, 172405 (2003). [Cited on page(s) 113.]
- [32] C. N. Guy, J. Phys. F: Met. Phys. **8**, 1309 (1978). [Cited on page(s) 113.]
- [33] Y. T. Wang, H. Y. Bai, M. X. Pan, D. Q. Zhao, and W. H. Wang, Phys. Rev. B **74**, 064422 (2006). [Cited on page(s) 115, 116, and 118.]
- [34] V. K. Anand, D. T. Adroja, and A. D. Hillier, Phys. Rev. B **85**, 014418 (2012). [Cited on page(s) 116, 117, and 118.]
- [35] J. A. Mydosh, *Spin Glass: An Experimental Introduction* (Taylor and Francis, London, 1993). [Cited on page(s) 116 and 117.]
- [36] Z. Fu, Y. Zheng, Y. Xiao, S. Bedanta, A. Senyshyn, G. G. Simeoni, Y. Su, U. Rucker, P. Kogerler, and T. Bruckel. Phys. Rev. B **87**, 214406 (2013). [Cited on page(s) 116 and 117.]
- [37] L. Ma, W. H. Wang, J. B. Lu, J. Q. Li, C. M. Zhen, D. L. Hou, and G. H. Wu, Appl. Phys. Lett. **99**, 182507 (2011). [Cited on page(s) 116 and 118.]
- [38] P. C. Hohenberg and B. I. Halperin, Rev. Mod. Phys. **49**, 435 (1977). [Cited on page(s) 117.]
- [39] J. Souletie and J. L. Tholence, Phys. Rev. B **32**, 516 (1985). [Cited on page(s) 117 and 118.]
- [40] S. Shtrikman, and E. P. Wohlfarth, Phys. Lett. A **85**, 467 (1981). [Cited on page(s) 117.]
- [41] C. A. Cardoso, F. M. Araujo-Moreira, V. P. S. Awana, E. Takayama-Muromachi, O. F. de Lima, H. Yamauchi, Phys. Rev. B **67**, 020407(R) (2003). [Cited on page(s) 117.]
- [42] J. L. Tholence, Solid State Commun. **35**, 113 (1980). [Cited on page(s) 117.]
- [43] H. Aruga Katori, and A. Ito, J. Phys. Soc. Jpn. **63**, 3122 (1994). [Cited on page(s) 118.]
- [44] A. P. Young, and H. G. Katzgraber, Phys. Rev. Lett. **93**, 207203 (2004). [Cited on page(s) 118.]

- [45] H. G. Katzgraber, and A. P. Young, Phys. Rev. B **72**, 184416 (2005). [Cited on page(s) 118.]
- [46] H. G. Katzgraber, D. Larson, and A. P. Young, Phys. Rev. Lett. **102** 177205 (2009). [Cited on page(s) 118.]
- [47] J. R. L. de Almeida, and D. J. Thouless, J. Phys. A: Math. Gen. **11**, 5 (1978). [Cited on page(s) 118.]
- [48] M. Gruyters, Phys. Rev. Lett. **95**, 077204 (2005). [Cited on page(s) 118.]
- [49] J. J. Hauser, J. Magn. Magn. Mater. **15-18**, 1387 (1980). [Cited on page(s) 75 and 121.]
- [50] F. Hippert and H. Alloul, J. Phys. (Paris) **43**, 691 (1982). [Cited on page(s) 67, 73, and 121.]
- [51] J. B. Staunton, B. L. Gyorffy, J. Poulter, and P. Strange, J. Phys.: Condens. Matter **1**, 5157 (1989). [Cited on page(s) 67, 121, and 123.]
- [52] P. M. Levy, C. Morgan-Pond, and A. Fert, J. Appl. Phys. **53**, 2168 (1982). [Cited on page(s) 67, 121, and 123.]
- [53] T. Sato, Phys. Rev. B **41**, 2550 (1989). [Cited on page(s) 67 and 121.]
- [54] Y. Öner and H. Sari, Phys. Rev. B **49**, 5999 (1994). [Cited on page(s) 67 and 121.]
- [55] J. S. Kouvel, W. Abdul-Razzaq, and Kh. Ziq, Phys. Rev. B **35**, 1768 (1987). [Cited on page(s) 67 and 121.]
- [56] S. N. Lyakhimets, IEEE Trans. Magn. **30**, 840 (1994). [Cited on page(s) 123.]
- [57] P. M. Levy and A. Fert, Phys. Rev. B **23**, 4667 (1981). [Cited on page(s) 123.]
- [58] A. Stroppa, M. Peressi, Mater. Sci. Semicond. Process **9**, 841 (2006). [Cited on page(s) 100.]
- [59] P. Dey, T. K. Nath, P. K. Manna, and S. M. Yusuf, J. Appl. Phys. **104**, 103907 (2008). [Cited on page(s) 3 and 122.]
- [60] A. Spiesser, S. F. Olive-Mendez, M. T. Dau, L. A. Michez, A. Watanabe, V. Le Thanh, A. Glachant, J. Derrien, A. Barski, M. Jamet, Thin Solid Films **518**, S113 (2010). [Cited on page(s) 29 and 128.]
- [61] V. Le Thanh, A. Spiesser, M. T. Dau, S. F. Olive-Mendez, L. A. Michez, and M. Petit, Adv. Nat. Sci.: Nanosci. Nanotechnol. **4**, 043002 (2013). [Cited on page(s) 128.]

Chapter 6

Conclusion

The main focus of this thesis was to characterize the magnetic anisotropy and determine the origin of the thermal irreversibility in the magnetization of Mn_5Ge_3 epitaxial thin films on Ge(111). Previous works have theoretically predicted that Mn_5Ge_3 can be a potential candidate for spin injection in the group IV semiconductor Ge. Due to its ability to grow epitaxially on Ge(111) with a relatively sharp interface, and the possibility to increase its Curie temperature by carbon doping, Mn_5Ge_3 on Ge(111) is increasingly becoming attractive. However, some features in the magnetization were not clearly understood, such as the relatively low in-plane remanence ratio at low temperature and the decrease of both in-plane and out-of-plane remanence ratios with increasing thicknesses of the thin films.

Chapter 4 evidenced the presence of an out-of-plane contribution for the magnetic anisotropy, which origin is the $\text{Mn}_5\text{Ge}_3(001)/\text{Ge}(111)$ epitaxial relation. Despite being a candidate for explaining the low in-plane remanence ratio, the out-of-plane anisotropy was shown not to have a sufficient magnitude to affect the in-plane magnetization. Although it has no direct effects on the magnetization cycles at low

temperatures, the out-of-plane magnetocrystalline anisotropy displays an interesting temperature dependence, which does not follow the Callen-Callen law. Despite not following the Callen-Callen law, the magnetocrystalline anisotropy in Mn_5Ge_3 thin films is still related to the magnetization by a power law, which reveals that the magnetic ions still interact with the crystal field but in a different manner than that given by the single-ion anisotropy model. The lower power in the temperature dependence of the magnetocrystalline anisotropy energy may be due to the hybridization between p orbitals from Ge sites and $3d$ orbitals from Mn sites, which decrease the degree of localization of the magnetic moment in the compound. However, such mechanism related to the deviation from the Callen-Callen model remains to be clarified. The single-ion anisotropy model is valid for localized spins, and it is not yet known how much the spins are localized in the Mn_5Ge_3 compound. Internal magnetostriction may also be a candidate to explain such discrepancy.

The existence of a thermal irreversibility in the $\text{Mn}_5\text{Ge}_3/\text{Ge}$ heterostructure was very intriguing and unexpected because no disorder was detected in either layers by structural characterization. The zero-field-cooling and field-cooling magnetization measurements, along with the ac susceptibility characterization determined that a slow magnetization dynamics occurs immediately after the material enters the ferromagnetic state, for decreasing temperature. The scaling laws indicate that the slow magnetization dynamics is similar to that observed in canonical spin glasses. A sudden increase of the field-cooling magnetization at low temperature implies that the origin of the spin-glass behavior is a surface effect arising from the coupling between two magnetic layers of different natures, thus suggesting that the “ferromagnetically dead” layer is a spin-glass. The shape of the ZFC and FC curves, and the position of the spin-glass transition depend on the growth conditions. The analysis of samples

annealed at higher temperature and samples with a higher thickness allowed to prove that the main relaxation process does not occur at the spin-glass transition, but just below the Curie temperature independently on the growth conditions. Thus, such slow magnetization dynamics is the result of the interplay between the ferromagnetic Mn_5Ge_3 and the spin-glass-like layer.

The region at the $\text{Mn}_5\text{Ge}_3/\text{Ge}$ interface is therefore characterized as a disordered magnetic phase, which has nonnegligible influence on the properties of the Mn_5Ge_3 epitaxial thin film, despite having a relatively small size compared to the rest of the film. Understanding the mechanism of the natural formation of such interfacial spin-glass can open new possibilities for spintronics device using the coupling between ferromagnets and spin glasses. The properties of spin currents in the $\text{Mn}_5\text{Ge}_3(001)/\text{Ge}(111)$ heterostructure may be altered within the stability domain of the spin-glass state.